



저작자표시-비영리-변경금지 2.0 대한민국

이용자는 아래의 조건을 따르는 경우에 한하여 자유롭게

- 이 저작물을 복제, 배포, 전송, 전시, 공연 및 방송할 수 있습니다.

다음과 같은 조건을 따라야 합니다:



저작자표시. 귀하는 원저작자를 표시하여야 합니다.



비영리. 귀하는 이 저작물을 영리 목적으로 이용할 수 없습니다.



변경금지. 귀하는 이 저작물을 개작, 변형 또는 가공할 수 없습니다.

- 귀하는, 이 저작물의 재이용이나 배포의 경우, 이 저작물에 적용된 이용허락조건을 명확하게 나타내어야 합니다.
- 저작권자로부터 별도의 허가를 받으면 이러한 조건들은 적용되지 않습니다.

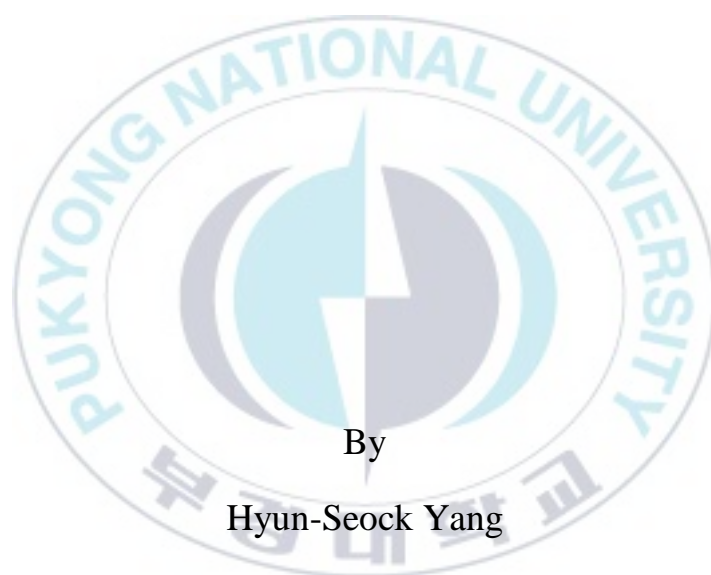
저작권법에 따른 이용자의 권리는 위의 내용에 의하여 영향을 받지 않습니다.

이것은 [이용허락규약\(Legal Code\)](#)을 이해하기 쉽게 요약한 것입니다.

[Disclaimer](#)

Thesis for the Degree of Doctor of Philosophy

Characterization of charge transport in bulk heterojunction organic solar cells



By

Hyun-Seock Yang

Department of Physics

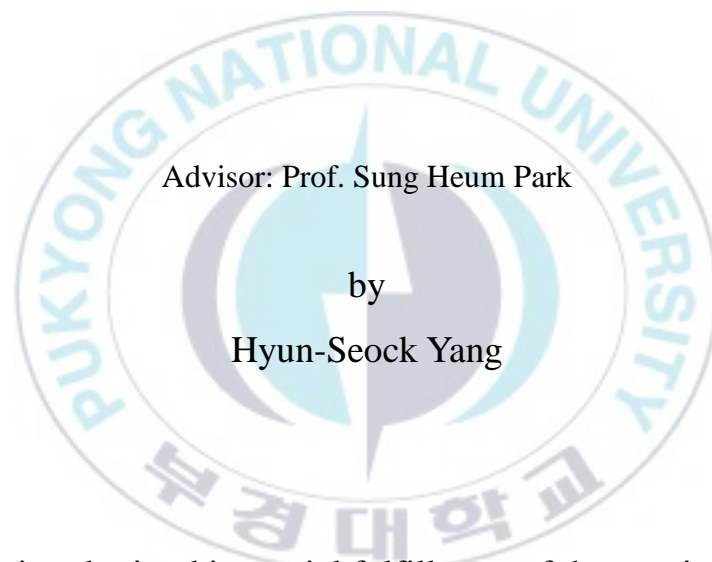
The Graduate School

Pukyong National University

February 2023

Characterization of charge transport in bulk heterojunction organic solar cells

(이종접합 유기 태양전지에서의 전하 수송 분석 연구)



Advisor: Prof. Sung Heum Park

by

Hyun-Seock Yang

A thesis submitted in partial fulfillment of the requirements
for the degree of

Doctor of Philosophy

in Department of Physics, The Graduate School,
Pukyong National University

February 2023

Characterization of charge transport in bulk heterojunction organic solar cells

Dissertation

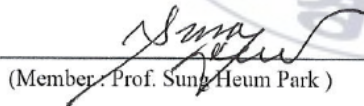
By

Hyun-Seock Yang

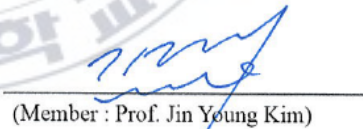
Approved by :



(Chairman : Prof. Bo Ram Lee)



(Member : Prof. Sung Heum Park)



(Member : Prof. Jin Young Kim)



(Member : Prof. Junghwan Kim)



(Member : Prof. Seyoung Kee)

2023.2.17.

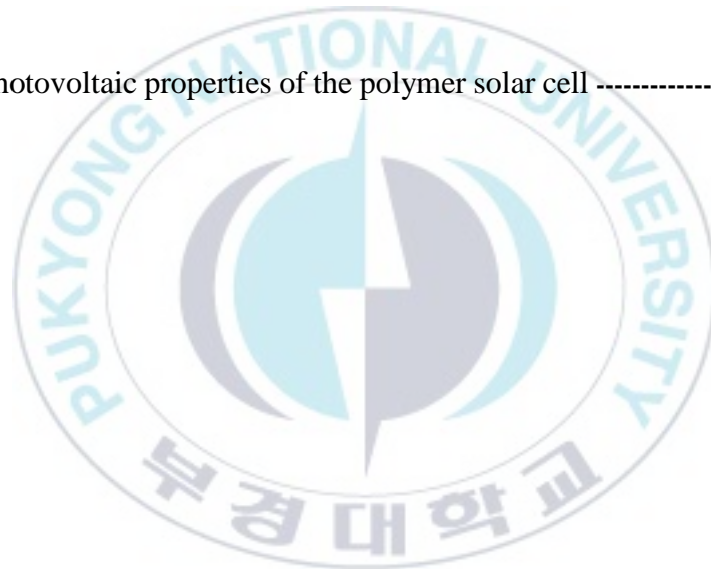
Content

CHAPTER 1 INTRODUCTION	1
1.1 Conjugated Organic materials	1
1.2 Optoelectrical Properties of Conjugated Organic materials	4
1.3 Application of Organic materials to Solar cell	10
CHAPTER 2 THEORY	13
2.1 Charge Transport at Interfaces between Donor and Acceptor	13
2.1.1 Delocalization of Excited Electrons in Organic molecular	13
2.1.2 Hot-State Charge Transport in Bulk heterojunction Organic Film	15
2.2 Voltage loss in Organic Blend System	20
2.2.1 Origin of Voltage Loss in Organic Blend System	20
2.2.2 Strategy for Reducing Voltage Loss	26
2.3 Device Physics for Bulk heterojunction Organic Solar Cell	29
CHAPTER 3 EXPERIMENTAL	32
3.1 Material Preparation	32
3.2 Device Preparation	34
3.3 Analysis	35

CHAPTER 4	STUDY ON CHARGE TRANSPORT BETWEEN DONOR AND ACCEPTOR	37
4.1	Introduction	37
4.2	Result and Discussion	39
4.2.1	Hot-state matching formations at the two organic materials system	39
4.2.2	Quantification of the hot-state matching in organic blend system	42
4.2.3	Correlation between hot-state matching and PICT	50
4.3	Conclusion	56
CHAPTER 5	APPLYING EFFICIENT CHARGE TRANSPORT ON ORGANIC SOLAR CELL	57
5.1	Introduction	57
5.2	Result and Discussion	60
5.2.1	Mismatching Factor from Modified Optical Density	60
5.2.2	Design of Conjugated Organic materials	80
5.3	Conclusion	89
CHAPTER 6	CONCLUSION	90
REFERENCES		92
ACKNOWLEDGEMENT		100

LIST OF TABLES

Table 1. Integrated MF of PBDB-T:ITIC:PC71BM blend system -----	76
Table 2. Photovoltaic parameter with ratio of PBDB-T:ITIC:PC71BM -----	78
Table 3. Optoelectrical properties of polymers -----	83
Table 4. Photovoltaic properties of the polymer solar cell -----	85



LIST OF FIGURES

Figure 1. Schematic diagram of sigma and π orbital-----	2
Figure 2. Schematic diagram for band structure of conjugated organic materials-----	3
Figure 3. Process of Photoinduced Charge Transfer-----	5
Figure 4. Light induced electron spin resonance (LESR) setting and data-----	6
Figure 5. Transient absorption spectra (TAS) setting and data-----	7
Figure 6. Sensitive EQE and EL data for organic based blend system-----	9
Figure 7. Mechanism of AFM and GIWAX measurement-----	12
Figure 8. Charge transfer mechanism in the blend system of organic materials-----	16
Figure 9. Scheme for cases of the molecule distance and resonance distance--	19
Figure 10. Scheme for photon energy loss analysis in solar cells-----	22
Figure 11. Scheme for process of Auger recombination-----	24

Figure 12. Charge transfer mechanism on mismatched and well-matched states-	
-----	28
Figure 13. J-V characteristics of solar cell-----	29
Figure 14. Mechanism of PICT at mismatched state and well-matched state--	40
Figure 15. Energetics of the formation of hot-state matching for PICT-----	41
Figure 16. Scheme for mismatching factor from photon energy spectra and electron energy spectra -----	43
Figure 17. UPS measurement for P1, P2, D18, PCBM, PC71BM and Y6-----	44
Figure 18. Material and optical properties of P1 and PC71BM-----	46
Figure 19. Energy level diagram with OD of the unoccupied molecular orbitals-	
-----	48
Figure 20. Material and optical properties of P1 and PC71BM-----	49
Figure 21. Energy level diagram with population of OD for various organic materials-----	51

Figure 22. MF of the each blend systems (PTB7-Th:PC71BM, PTB7-Th:ITIC and PTB7-Th:IEICO-4F) -----	52
Figure 23. Optical and energetic properties of components for PTB7-Th based two organic materials system-----	54
Figure 24. Optical and energetic properties of components for PBDB-T based two organic materials system-----	54
Figure 25. Electron dynamic in the blend system-----	55
Figure 26. Variation of Voc under irradiation of different monochromatic light for P1:PC71BM-----	61
Figure 27. Saturated Voc under the condition of particular wavelengths-----	63
Figure 28. Light intensity dependent Voc at each state matching formations--	65
Figure 29. Wavelength dependent Voc of binary blend system-----	66
Figure 30. Variation of quasi-Fermi levels under light irradiation-----	68
Figure 31. Photovoltaic properties for applying MODO to organic based solar cell. -----	71

Figure 32. MF of PBDB-T based blend systems-----	71
Figure 33. Device and molecular structure of D18, Y6 and PCBM with role of third component. -----	72
Figure 34. Photovoltaic properties for applying MODO-----	74
Figure 35. Photovoltaic properties with Integrated Mismatching dependent---	75
Figure 36. Complementary absorption spectra with the various ratio of PBDB- T:ITIC:PC71BM blend-----	75
Figure 37. Mismatching factor of PBDB-T:ITIC:PC71BM blend system-----	76
Figure 38. Photovoltaic properties of PBDB-T:ITIC:PC71BM solar cell-----	77
Figure 39. Diverse tendency between photovoltaic parameter and DOS matching-----	78
Figure 40. Charge transfer mechanism on mismatched and well-matched states- -----	79
Figure 41. Molecular structures and energy levels of electron donor and PC71BM and schematic diagram of the PSC device architecture-----	81

Figure 42. UV–visible absorption spectra of polymers in dichlorobenzene solution-----	82
Figure 43. Electrochemical properties of polymers-----	83
Figure 44. Theoretical calculation of the monomers by density functional theory (DFT) at the B3LYP/6–31 G level-----	84
Figure 45. Current density-voltage characteristics of the polymer solar cells under the illumination of AM 1.5, 100 mW/cm ² -----	86
Figure 46. IPCE curves of the corresponding polymer solar cells-----	87
Figure 48. AFM images of films spin coated from PBDT-FPz:PC70BM, PBDT-TFPz:PC70BM and PBDT-DTFPz:PC70BM with DIO-----	88

Abstract

Charge transport between conjugated organic materials called as photoinduced intermolecular charge transfer (PICT) plays an important role in determining the power conversion efficiency (PCE) of bulk heterojunction (BHJ) organic photovoltaics (OPVs) especially open circuit voltage. Since the PICT originates from the both geometric and energetic accessible delocalized state matching, energetic characterization of PICT between conjugated organic materials should be understood. In this study, the energetic characterizations as hot-state matching and HOMO level tuning were studied for efficient PICT between donor and acceptor. Firstly, an effective method to quantify the hot-state matching of OPVs is developed. By calculating the mismatching factor (MF) from the modified optical density overlapping (MODO) in the BHJ, the degree of energy-state matching between the electron donor and acceptor at the BHJ interface is quantified. Furthermore, the correlation between MF and PICT is also studied. Secondly, the correlation between the V_{oc} loss of the OPV device and the energy-state matching at the BHJ interface is investigated via applying MF. OPVs with smaller MFs exhibit higher V_{oc} values. Because the MF indicates the degree of energy-state matching, which is a critical factor for suppressing energy loss, it can be used to estimate the V_{oc} loss in OPVs. Thirdly, HOMO level of organic materials is tuned by controlling numbers of thiophene unit. Thereby indicating that increased numbers of thiophene units in the backbone resulted in high HOMO energy levels, resulting in enhancement of V_{oc} . These result clearly indicates that the energy-state matching between the donor and acceptor is crucial for achieving high V_{oc} in OPVs.

이종접합 유기 태양전지에서의 전하 수송 분석 연구

양 현 석

부 경 대 학 교 대 학 원 물 리 학 과

요 약

공액 유기물질계면에서 일어나는 빛에 의해 유발된 전하이동(Photoinduced charge transfer, PICT)은 이종접합 유기태양전지에서 개로 전압 등의 광-전 효율을 결정짓는 중요한 역할을 하는 요소이다. PICT는 두 종류의 다른 상을 가지는 유기물질간의 비편재화된 상태 결맞음에서 비롯되기 때문에 공액 유기물질 사이의 에너지 특성에 대한 이해가 반드시 필요하다. 본 연구에서는 유기물질 계면상 발생하는 전하이동에 대한 연구를 다각적으로 진행했다. Chapter 1에서는 유기물질 간의 들뜸 에너지 준위 매칭을 효율적으로 정량화하는 방법을 연구했다. 본 연구에서는 두 유기물질의 광밀도 곱침을 이용하여 불균형 상수를 계산함으로써 전자 주개 물질과 받개 물질간의 에너지 준위 균형을 정량화했으며, 이를 바탕으로 불균형 상수와 전하이동간의 상관관계를 규명했다. Chapter 2에서는 유기태양전지의 개로 전압과 불균형 상수간의 상관관계를 연구함으로써, 본 연구에서 새롭게 제시된 불균형 상수 개념을 실제 소자에 적용했다. 그 결과 불균형 상수가 적은 혼합계일수록 낮은 개로 전압손실로 인해 높은 개로 전압을 얻을 수 있었다. Chapter 3에서는 유기물질의 사이오펜의 개수를 조절함으로써 HOMO 준위를 조절하는 연구를 진행했다. 위의 세 가지 연구 결과는 전자 주개와 받개의 에너지 준위 균형이 PICT를 향상시키는데 매우 중요한 역할을 하는 것을 보여준다. 결과적으로 위와 같이 세가지 방법을 통해 유기 물질 계면상 발생하는 전하이동 특성을 분석하고 이를 통해 더욱 효율적인 전하이동을 유도하는데 성공했다.

Chapter 1 Introduction

1.1 Conjugated Organic Materials

Conjugated organic materials are one of the widely used semiconducting materials in recent decades.¹⁻³ Because the conjugated organic materials have various semiconducting properties which can be tunable by molecular, these organic materials have been applied numerous kinds of electronic devices.^{4,5} Organic photovoltaics, organic light emitted diode (OLED) and field effect transistors (FETs) would be example of applying conjugated organic materials. As similar as general organic materials, the conjugated organic materials are also composed with the basis on carbon (C) chains with oxygen (O) and hydrogen (H).⁶ Among the various types of organic materials, the origin of semiconducting or metallic property which is electrical conductive is “conjugation” structure of bonding within the organic materials.^{6,7} The conjugation structure is alternating structure that of two or more double bonding exist with a single bond between them. By establishing this origin of conjugated organic materials Hideki Shirakawa, Alan MacDiarmid and Alan Heeger reports the first example of conductivity values in the metallic regime, for which the 2000 Nobel Prize in Chemistry was awarded.⁸

The carbon atom of organic chains has 6 electrons outside of the nucleus, among them 4 are valence electrons (2s and 2p) which takes part in chemical bonding.^{6,7} From the point view of total energy and the chemical bonds in carbon bonding, there are two formation of hybridization structure for bonding orbitals with tetrahedral symmetry (saturated organic materials) and hexagonal symmetry (conjugated organic

materials).^{6,7} Because the tetrahedral symmetry as sp^2p_z hybridization is available to form a π -bond, planar backbone with sp^2 δ -bonding with the perpendicular p_z formation can be constructed. The s orbital is spherically symmetric while p_x , p_y and p_z are directly along the each axis. Therefore the conjugated organic materials have the three in-plane δ -orbitals which constructs backbone of molecular and one π orbital which is orthogonal to the plane, and the electron of p_z orbital called as π -electron (**Figure 1**).⁹⁻
¹¹ Because the π -electron has attracting force from the nuclei of the neighboring carbon atoms, the π -electrons delocalize along the chain of molecular. And this π -electron being decoupled from the backbone causes the unique electrical properties to conjugated organic materials.^{3,6,12}

The electrons in organic materials are bounded by a nuclei, and the nuclei is forming a chain in organic materials.^{3,6,12} In this circumstance, the electrons would be affected by the neighboring nuclei, and the affection from nuclei changes kinetic energy of electrons.^{1,8,13} The change of kinetic energy originate the electron forbidden energy level called band gap. In organic material system, it is simply considered that the carbon chain is same as linearly combined lattice. Therefore, in order to understand the energy structure of conjugated organic materials, linear combination of molecular orbitals (LCMO) is required.

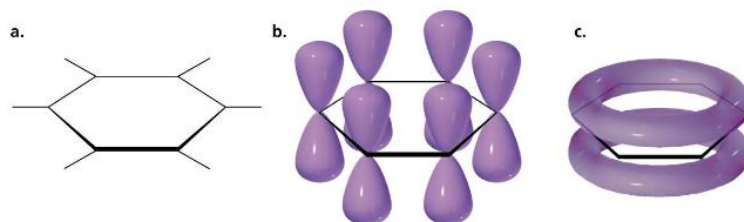


Figure 1. Schematic diagram of sigma and π orbital a) Planar backbone of conjugated benzene, b) Perpendicular p_z orbitals of π electrons, c) Delocalization of π electrons

In organic materials, the energy band consists of both bonding and anti-bonding energy levels.^{8,13} The both the bonding and anti-bonding energy levels associated with sp^2 wave functions of δ bond while the π energy levels which is located between the bonding and anti-bonding energy levels associated with p_z wave function of π bond (Figure 2).¹⁴ The π energy levels which constructed by the linear combination of p_z orbitals of repeated unit have the higher conductivity from the delocalization of π -electrons within the organic materials. In the molecule, the π -electron excitation to anti-bonding of π -levels can generate current without the breaking of molecular structure.^{6,15} Therefore, because the targeting electrons in conjugated polymer for electronic devices would be the electrons in π energy levels, understanding of injected electron into π energy levels by photon excitation or charge injection by external voltage must be required for using of conjugated organic materials.¹⁶

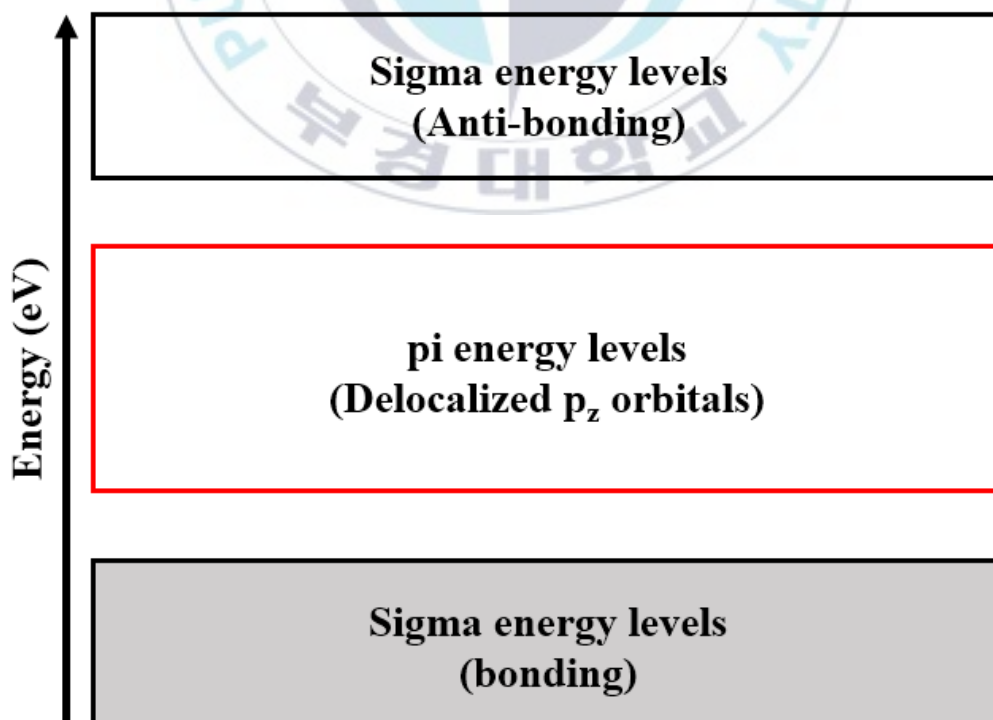


Figure 2. Schematic diagram for band structure of conjugated organic materials

1.2 Optoelectrical Properties of Conjugated Organic Materials and Analysis Method

Although the semiconducting or metallic property of conjugated organic materials is originated by delocalization of π electrons within molecular structures, there are no electrons in anti-bonding energy level (π^*) of π -band at neutral stable state in nature.^{17,18} The π energy levels (valance band) are all occupied states by π electrons at neutral stable state while all π^* energy levels (conduction band) are empty in this condition. It can be a main reason that the general conjugated organic materials does not have free carriers as metals and charge creation in π^* energy levels as doping and photon excitation is required for conjugated organic materials. Among them, this study focuses on the charge generation by photon excitation.^{19,20}

The electrons in fully occupied valance state can be excited π^* energy levels by absorption of photon energy.¹² However, the excited electron are strongly bounded with hole as form as exciton. The exciton is a quasi-particle which is bounded by electrostatic attractive Coulomb force between electron and hole.²¹ In case of organic materials the relatively low dielectric constant of organic materials causes the strong binding energy of exciton with the range from 0.1 to 1 eV which called as “Frenkel exciton”.^{22,23} Even though the electrons are located within π^* energy levels by excitation, electrical neutral state of exciton by geometrically coupled excited electron and hole as formation as exciton is hard to generate free carriers. Therefore, electron accepting materials are required to generate free carriers.^{23,24} The electron acceptor is a role to separate exciton for free carrier generation by using electron affinity difference

of each organic materials, and the excited electron on donor transfers to the lowest energy unoccupied molecular orbital (LUMO) of the acceptor. This electron transfer is called as “photoinduced electron (charge) transfer”.²⁵⁻²⁸ It means that the blend system of two organic materials (one is electron donor, another is electron acceptor) can generate free carriers under the photon irradiation condition.

The blend system for the photoinduced charge transfer (PICT) must generate additional interfaces between donor and acceptor, and this additional interfaces results in several intermediate states before generation of free carriers.^{29,30} The intermediate states can be separated as three parts as exciplex formation, charge transfer formation and radical pair formation.^{10,31,32} The exciplex formation is delocalized state in formation of exciton on donor and acceptor complex. In this state, each electron and hole does not have partial charge because of geometrical coupling.^{3,33} When the coupling is broken by the difference of electron affinity, the electron and hole have partial charge in charge transfer state. Finally, the transferred electrons on acceptor domain and remained hole on donor domain have radical pair formation which can perfectly separate by potential energy.^{3,10,24}

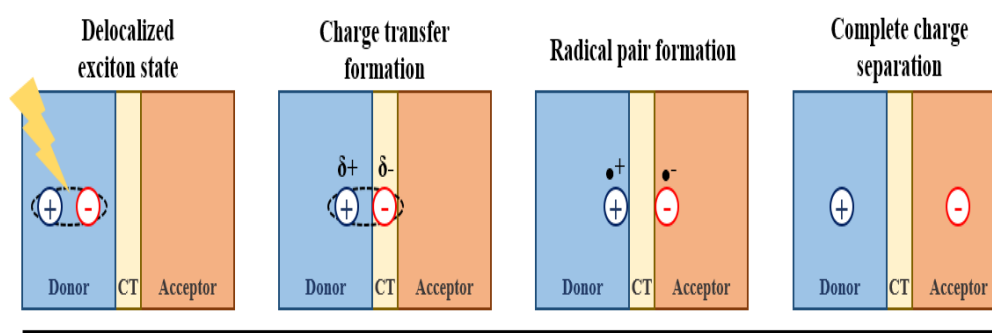


Figure 3. Process of Photoinduced Charge Transfer

The important point of intermediate states is that the excited electron energy continuously relax toward LUMO level by thermal relaxation and the relaxed exciton or electrons in charge transfer state causes either radiative or non-radiative recombination of electron and hole pair.^{14,34} The radiative and non-radiative recombination reduce the final number of collected free carriers at both cathode and anode of device.^{35,36} Therefore, in the blend system of conjugated organic materials, suppression of recombination is required.

The origin of PICT at interfaces between donor and acceptor is a result of the uncertainty principle of the fundamental quantum uncertainty. Therefore, the PICT is the ultrafast charge transfer that requires the delocalized coherent superposition between donor and acceptor materials.^{17,37,38} Each donor and acceptor have their initially delocalized coherent state, and nanostructured organic blend system can be described by Eigen functions of Schrodinger equation from initially delocalized coherent state. Because these quantum phenomena of PICT has the time scale under 100 fs, electron dynamics under the photon irradiation condition have been studied by using several advanced measurement such as light induced electron spin resonance (LESR), transient absorption and sensitive external quantum efficiency.

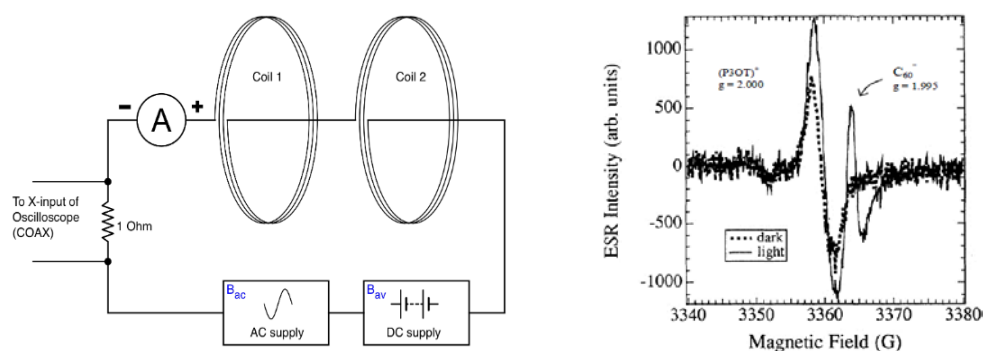


Figure 4. Light induced electron spin resonance (LESR) setting and data²⁶

The LESR is a measurement for detecting both radical formation and complete charge separation in the blend system of donor and acceptor.²⁶ Independent precession signal of the spins on donor and acceptor at irradiation condition which can be observed from LESR means complete charge separation in the blend system.⁸ Moreover, the difference of relaxation time for each independent precession signal provide the information about the carrier relaxation time of separated electrons and hole on acceptor and donor.²⁷ However, because relatively similar g-values of conjugated organic materials are hard to sort the each independent precession, generally LESR is used in case of fullerene based blend system.³⁰

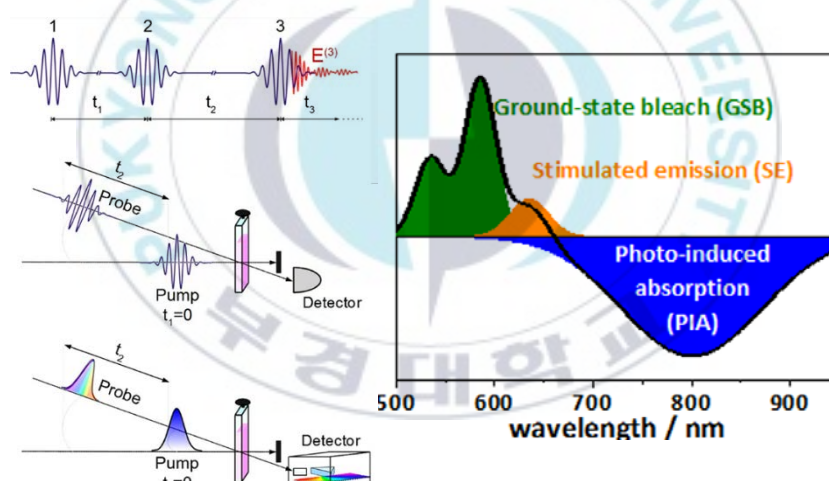


Figure 5. Transient absorption spectra (TAS) setting and data

One of the most widely used analysis method for PICT is transient absorption spectra (TAS) which has fundamental as pump-probe measurement.³⁹ Electrons on valence band edge (HOMO level) excite to hot-state energy level which corresponding the upper energy level of LUMO by pump photon. Before the time scale of thermal relaxation (~ 50 fs) secondary probe photon is irradiate to the excited system.³⁴ The spectra of probe light provides three parts of signals divided with the range of

wavelength as ground state bleach (GSB), stimulated emission (SE) and photo-induced absorption (PIA).^{40,41} The GSB has negative value of “ $\Delta A/A$ ” where A is absorption of organic materials and ΔA are the changed absorption of excited state.

The GSB covers the range of shorter wavelength which is similar with intrinsic absorption range of organic materials. The negative GSB means photo-bleaching of the ground states by strong pump excitation. The degraded GSB around absorption edge means stimulated emission.^{42,43} In order to analysis the PICT, PIA part are usually considered, because the dynamics of the excited electrons on hot-state can be determined by PIA.⁴⁴

Generally, the wavelength around initial part of positive $\Delta A/A$ shows the information of charge transfer state (CT).^{34,45,46} Otherwise, longer wavelength of PIA part shows the information of polaron state of the blend system. The relaxation time of each part also analyzed by time resolved PIA.⁴⁰⁻⁴² However, even though the PIA has information about CT and polaron state of organic materials, quantitative analysis of dynamics of CT and polaron state is hard to understand. The reason is that the information of PIA is mixed complex feature of both CT and polaron states. Therefore, analysis of independent CT of polaron state also required to understand the dynamics of PICT.

The CT state which occurs non-radiative recombination usually locates at the sub-band gap of organic materials, and the CT state called as lowest lying charge transfer state.^{47,48} In this point view, optical transition from the formation of PICT to CT states is one of the important factor for determining the efficiency of PICT. This means that

the dynamics of electrons which are fall into the lowest lying CT states are important to understand efficient PICT. In order to detect this information, analysis of sensitive external quantum efficiency (EQE) measurement with electroluminescence (EL) spectra is used.^{1,13} The sensitive EQE spectrum can be calculated via Fourier-transform photocurrent spectroscopy. The sensitive EQE measurement is a combined results of EL and EQE of the blend system.^{14,49,50} The EL is a process for charge recombination, while EQE is a process for charge generation. From the maximum points of both EL and EQE spectrum, because these process are vice versa, the reduced section of each EL and EQE should be overlapped in the dimension of energy level as shown **Figure 6**. In the sensitive EQE spectrum, CT band covers low energy part which the value of EQE enhances dramatically range. Based on the fitted EL and EQE spectrum, the energy level of CT states for organic materials also can be calculated.^{35,51,52}

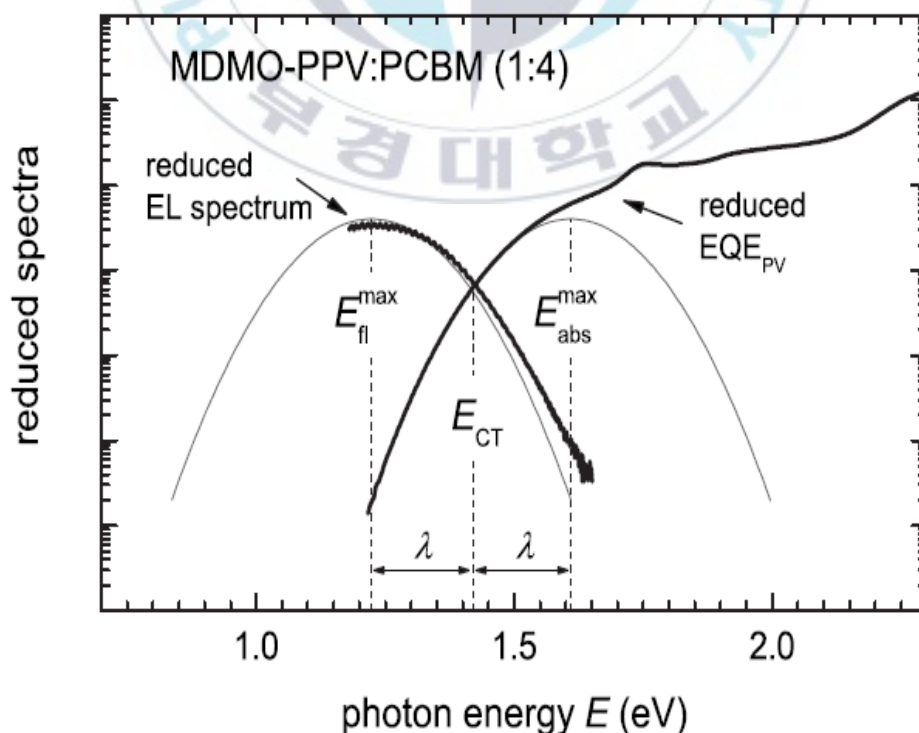


Figure 6. Sensitive EQE and EL data for organic based blend system³⁵

1.3 Application of Organic Materials to Solar cell

The main application of PICT on electric device is the conjugated organic material based bulk heterojunction solar cell.^{1,8,17,43,46} The solar cell is a device which converts solar energy to electrical energy by creating electrons and holes, and bulk heterojunction means the heterojunction between donor and acceptor within the thin bulk film fabricated from mixture of donor and acceptor materials. Because the conjugated organic materials is soluble to organic solvent such as chlorobenzene, solution process as spin coating and ink-jet method are widely used for stacking layers for organic based solar cell.^{4,16,53} Each layers including functional layer and photo active layer have interfaces between the layers, and it becomes the trap site on solar cell. The trap sites reduced the number of collected charge at electrode. Therefore, suppressing the trap sites is effective method to enhance the performance of organic solar cell.

The simplest main mechanism of solar cell can be divided by three parts as absorption, PICT and charge collection at the opposite electrode.^{14,54} The electrons on HOMO levels excites to hot-state energy levels as form as the exciton by absorbing photon energy. Although the quasi-Fermi level differences between cathode and anode constructs built-in potential in active layer, the electrical neutral property of exciton never be influenced by built-in potential.^{2,3,35,55,56} However, in the blend system of donor and acceptor, the relatively strong electron affinity of acceptor causes electron transfer to acceptor domain. If the transferred electrons are sufficiently separated from binding energy of positive radical by remained hole on acceptor domain.^{10,57} The

electrons are collected within electrode by built-in potential. This process is same with diode, but in case of organic based solar cell requires the photon energy for PICT.

Although each layer of organic based solar cell should be developed for enhancement of performance, this research is focusing on the only active layer. The active layer is a role to photon energy absorption and generating free carriers. Because the exciton diffusion length which is the length scale of exciton before carrier recombination is around 10 nm, the phase separated bulk heterojunction would have the several nanoscales.^{46,58-61} These interpenetration network of donor and acceptor have advantage to enhance the probability of exciton separation. Therefore, morphological optimization of active layer is one of the important factor for performance of organic solar cell.^{46,51,62} This morphological property of the blend system usually controlled by post-treatment method, additive materials and tuning of molecular structures. These control have effects on solubility and miscibility, results in phase separation of donor and acceptor.^{4,14,63} These morphological properties can be measured by several kinds of method such as Atomic force microscope (AFM), Transmission electron microscope (TEM) and Grazing-incidence wide-angle X-ray Scattering (GIWAX). The AFM is a general tool to detect the nanostructure of surface. It also shows the partial difference of work function for each point of film.⁶³⁻⁶⁵ The crystallinity of organic thin film can be measured by GIWAX.^{10,60,64} The stacking state organic materials such as pi-pi stacking can be determined by GIWAX. At last, The TEM is a tool for detection about length scale of phase separation and connectivity of network for the blend system.⁶⁶⁻⁶⁹ The one more controllable factor in active layer is about energetic favorable structure of donor and acceptor. The conjugated organic materials have their intrinsic energetic

structure. The energetic structure can be considered as the HOMO, LUMO level, band gap and hot-state energy level. Under the fundamental of LCMO, the energy difference between HOMO and LUMO level are band gap of each materials. Because the LUMO level means electron affinity, LUMO level of acceptor must be deeper than LUMO of donor. Otherwise, in the point view of hole, HOMO of acceptor also must be deeper than HOMO of donor. In the past decades, the charge transfer at interface between donor and acceptor considered as energy-gradient drive molecular hopping. Therefore, empirical rules of V_{oc} which requires extra energy with the range of 0.3 eV for exciton separation have to be fulfilled to fabricate solar cell.⁷⁰ However, advanced technology of photo-physical measurement demonstrated that the energy-gradient driven molecular hopping is a phenomenon of several particular organic materials, and the PICT is determined by the ultra-fast charge transfer in hot-state energy level and the influences from charge transfer state. From this numerous of effort to develop the organic based solar cell, over than 18.5 % of power conversion efficiency (PCE) has been achieved. However, the mechanism or the effect of PICT and CT states still debate, because the development of higher resolution of advanced photo-physical measurement such as TA and sensitive EQE have observed the unique and new property of the blend system of conjugated organic materials.

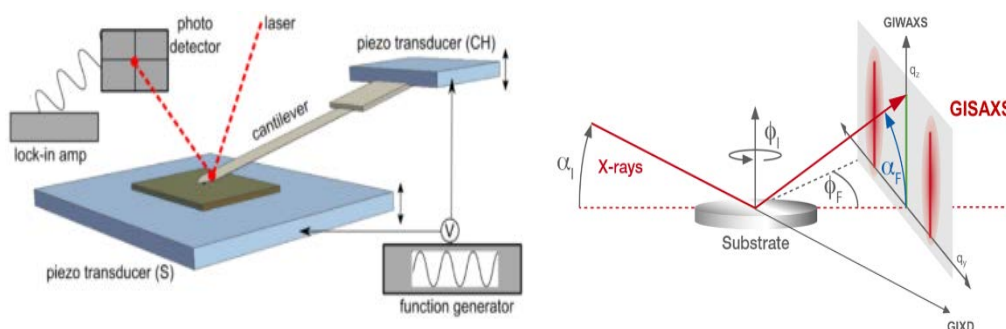


Figure 7. Mechanism of AFM and GIWAX measurement⁶⁰

Chapter 2 Theory

2.1 Charge Transport at Interfaces between Donor and Acceptor

2.1.1 Delocalization of Excited Electrons in Organic molecular

Optoelectronic properties of conjugated organic materials is well explain by LCMO as previously mentioned.^{6,71} In conjugated organic materials, the number of p_z orbital originates the number of electron states which is determined by the number of nodes.^{27,55,72,73} The number of node has same value with the number of states for anti-bonding of π^* orbital. This means that the states where has lower energy level that the state which has the half of whole number of p_z orbital would be valence states, and the highest energy state of valence state for group of node is HOMO level.^{14,17,70} Because the electrons are occupied in these states in neutral condition, there are no energy degradation. However, if the electrons are located on the energy level above HOMO level which is unoccupied energy level, energy release occurs within the energy scale of vibronic energy. In order to excite the electrons on HOMO level to upper level, fortunately the external energy is required with the scale of optical energy (several eV). In the point view of bond length alternation (BLA), the 1D chain of conjugated organic materials has nearly similar energy levels between HOMO and LUMO. It means that even though there is an energy barrier between alternation conditions of conjugation, therefore there are no difference of energy between the alternations. However, in case of aromatic ring such as benzene, the energy of aromatic and quinoidal is relatively difference ($E_{\text{aromatic}} < E_{\text{quinoidal}}$).^{10,74} And the calculated energy of each E_{aromatic} , $E_{\text{quinoidal}}$ usually matched with HOMO and LUMO level of materials. It can be a main reason

that general conjugated organic materials are based on the aromatic ring. Based on BLA, the delocalization property of conjugated organic materials can be tuned by doping of sulfur or nitrogen on aromatic ring.^{72,75} These approach stabilizes the electrons on LUMO level resulting in the enhanced optical property of materials including band gap open.

The delocalization along the chain of conjugated organic materials can be described by Su-Schrieffer-Heeger (SSH) Hamiltonian. The SSH Hamiltonian has three parts as written below.^{6,8,71}

$$H_{SSH} = \sum_{n,\sigma} [-t_0 + \alpha(u_{n+1} - u_n)](c_{n+1,\sigma}^+ c_{n,\sigma} + c_{n,\sigma}^+ c_{n+1,\sigma}) + \sum_n \frac{p_n^2}{2m} + \frac{1}{2} K \sum (u_{n+1} - u_n)^2 \text{-----Equation 1.}$$

Where the c^+ is fermion creation operator and c is fermion annihilation operator, p is the nuclear momenta for site n , u is displacement from equilibrium, m is carbon mass, and K is effective spring constant of the δ -bond. There are three parts on the SSH Hamiltonian. The second and third part are showing nuclei vibrational with considering of their displacement from equilibrium positions. The electronic structure of conjugated organic materials is described in the first part with the tight-binding approximation of the π -band structure. The electron transfer of hopping from i to $i \pm 1$ is described with $-t_0$. Because the transfer energy increase by the attractive interaction between electrons at i site to $i \pm 1$, the magnitude of $-t_0$ is roughly proportional to the ionization potential of the atom. Therefore the overlapping of the wave function for charge transfer by delocalization would be described to $t_0 \approx 2I_p \langle i | i \pm 1 \rangle$. Where I_p is ionization potential. The factor of 2 comes from the existence of the kinetic and potential energy on the electron. In generally the electron energy loss measurement of the band dispersion have showing that the t_0 of the conjugated organic materials is nearly 3 eV, while the

ionization potential is 5 eV. These values mean that the overlapping of the wave function is relatively huge ($\langle |i \pm 1| \rangle \approx 0.3$) and results in the strong tendency toward delocalization of the electrons along the chain of conjugated organic materials.

2.1.2 Hot-State Charge Transport in Bulk heterojunction Organic Film

In the blend system of two conjugated organic materials as bulk heterojunction structure, the charge transfer process have been demonstrated as ultra-fast charge transfer.^{14,58} The ultra-fast charge transfer is resulted in the electron delocalization in the blend system, and it has a time scale under 50 fs.^{14,65} Even the time scale is relatively longer than the charge transport at the metal to metal interface (several hundreds of atto-seconds), the time scale of charge transport at organic materials fulfills the time scale for photoinduced charge generation. Because the fundamental of PICT is based on delocalization of electrons, the PICT also originate by quantum uncertainty. It can be a main reason that the extended excited states of wave function should be considered to the blend system. The uncertainty of position and momentum of excited electron also obeyed by the Heisenberg's uncertainty equation. Therefore, the PICT generates in the condition of the delocalized coherent superposition of the Eigen functions for each donor and acceptor including with blend system, and the charge have to transfer before the collapse of the delocalized coherent superposition.^{27,76-78} However, each conjugated organic materials have different time scale for the collapse of the delocalization state, resulting in the different rate of generated mobile carriers and the influences of CT states.^{55,61,74} Although the hot-state charge transfer is an ultimately high efficient charge transfer at the interface of donor and acceptor, the rate of generated final mobile carriers are different with it, because of trapped or recombined charge carriers. And the

dominant sites of these trap and recombination are CT state especially the lower lying CT states under LUMO of acceptor.^{21,54} Therefore the understanding of the sub-bandgap have been required for dynamics of PICT. Although it is well known that the excess energy or driving energy for electrons does not effect to enhancement of the number of generated mobile carrier by overcoming CT state, the directly generate mobile carrier on hot-state which has less influence from CT state can suppress the recombination rate at interfaces.⁷⁹ Therefore, the relation between the process of PICT and thermal relaxation in particular blend system must be understood. Because the time scale between the frequent events shows the information of probability for each events, the optical process such as PICT or thermal relaxation can be determined by the comparison of time scale for each events.

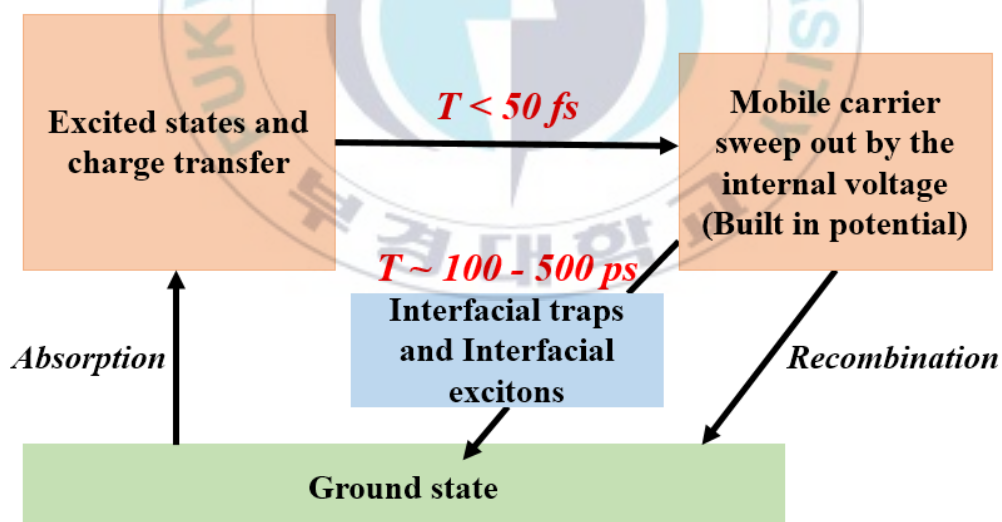


Figure 8. Charge transfer mechanism in the blend system of organic materials

The time scales for the light absorption with the generation of delocalization states is 0-5 fs (under 20 fs), in this time scale the generation of direct CT states also occur at interfaces from attractive force with delocalization, while indirect CT states (after relaxation) are generated in relatively slow time scale from 100 to 200 fs, and the

collapse of CT states occurs after 600 ps. Otherwise the time scale of PICT is nearly 50 fs which is a reason that direct charge transfer at hot-state is called as ultra-fast charge transfer.^{14,41,80} This means that the influence from CT states to PICT continuously exists during whole of PICT process, and trapped electron in CT states is hard to overcome the barrier of CT states. However, fortunately, the relaxation time scale from hot-state to LUMO or CT states relatively longer than the time scale of PICT with the range of 50 fs–10ps.^{52,55,60} Therefore, in order to boost the efficient PICT with suppressed recombination at CT states, the directly transferred PICT process is required. These properties also can be explained by the spin system of excited electrons. Although the life time of singlet state for excited electrons are known as nearly 1.2 ps, the time scales that the only singlet exciton exists is under 80 fs.^{15,46,81} This means that both of the singlet and triplet states are co-existed within the range from 80 fs to 1.2 ps. Therefore, it can be considered such like that the co-existed states of both singlet and triplet exciton indicates the intermediate CT states. Otherwise, the only triplet states are observed after 1.2 ps which means the process of PICT already finish and there are only relaxation process is existed in this time scale.^{2,8,28,43,82} These optoelectronic properties of conjugated organic blend system shows that the directly generated charge carriers on hot-state by PICT is one of the important factor.

Because it is well known that the geometrical distance for PICT covers under 20 nm, the structure of blend system also be a crucial factor for PICT.^{4,14,17,80} The conjugated organic materials aggregate in thin film condition, and the aggregation causes the deformation of absorption and emission band.^{10,54} The reason of deformation is the pi-pi stacking which is orbital overlapping of pi electron in phase separated

molecular. Because the π - π stacking has two interaction between organic molecule as charge transfer interaction (short range) and coulomb interaction (long range), the type of aggregation for organic molecule must be considered.^{83,84} The type of aggregation is determined from the angle (α) between transition moment of molecular and the center of line joining. In case of H-aggregation, the range of α should be “ $54.7 < \alpha < 90$ ”, otherwise J-aggregation is “ $0 < \alpha < 54.7$ ”.^{55,72} Generally H-aggregation has aligned π - π stacking of organic molecule resulting in blue-shift of optical density, and J-aggregation with weak π - π stacking has red-shifted optical density.⁵⁹ The reason of this changes can be understood as the symmetry breaking of orbitals, and this symmetry breaking also causes the CT states at the interface between donor and donor. These changes of optical density affects to the optoelectrical property of photovoltaics. Therefore, control of the aggregation type by treatment or morphology control is required to enhance the performance of photovoltaics. The H and J-aggregation are the aggregation types in one materials.^{59,60,68,85} Although this CT states are the sites which have the high probability of recombination, the nonpolar dielectric system on the only one material system has less influence to the recombination on CT states between same organic materials. However, geometrical location of the combination of donor and acceptor is much different. However the blend system of donor and acceptor is clearly phase separated structure. In this case the location type can be divided as “face on” and “edge on”.⁸⁴ The face on has similar structure with H-aggregation which has high π - π stacking while edge on has J-aggregation structure which has relatively low π - π stacking. Because the PICT is originated by delocalized coherent superposition, the resonance between the wave function of donor and acceptor is necessary. This means that the resonance distance between donor and acceptor would be a key factor of the

distance between donor and acceptor molecule.⁴⁶ If the molecule distance (D) is longer than resonance distance (R) as “ $D > R$ ”, the PICT is suppressed because of absent charge accepting state. Otherwise if “ $D < R$ ”, electrons in donor would relax toward the energy level which fulfill the delocalized coherent superposition. Therefore the best condition for PICT is “ $D = R$ ” condition as shown in **Figure 9**. This theory well explain the importance of the resonance of the hot-state. The theory also well matched with some experimental results that the rate of PICT is different with the energy level of hot-state, and the difference is depend on the type of organic materials. Moreover, it is also discovered that the density of state at particular hot-state also give effect for the rate of PICT. Therefore, both of the energy level of well resonance and density of states would be require to get efficient PICT.

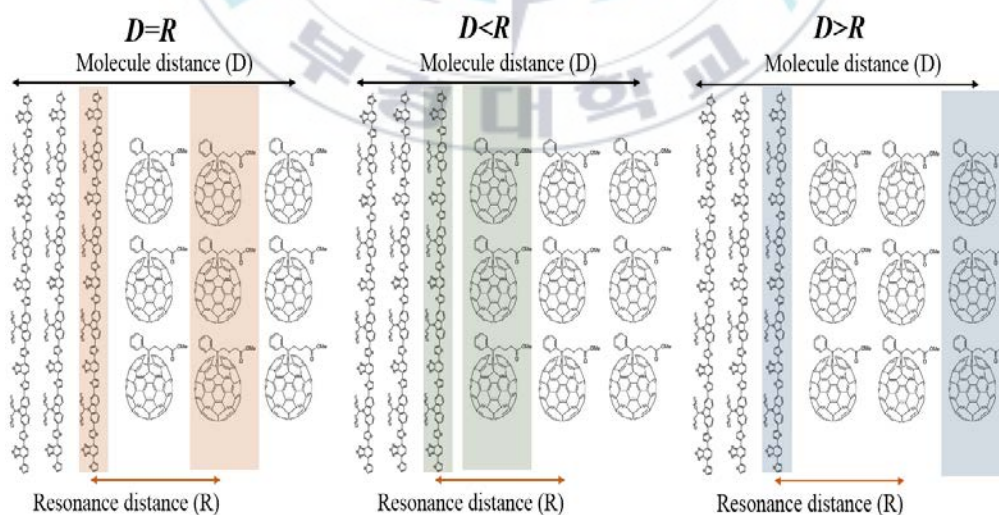


Figure 9. Scheme for cases of the molecule distance and resonance distance

2.2 Voltage loss in Organic Blend System

2.2.1 Origin of Voltage Loss in Organic Blend System

The bulk heterojunction structure of organic blend system has the interpenetrating donor and acceptor network in the film, and the interpenetrating network shows the nearly unity quantum efficiency. That is because both of the exciton and charge carriers diffuse randomly, after then they are eventually recombine. However, if the built-in potential are constructed in the blend system, the dynamics of exciton and charge carriers are different.⁸⁶⁻⁹⁰ The origin of built-in potential is the difference of work function between cathode and anode. The difference of work functions causes the symmetry breaking through the device resulting in construction of built-in potential. In this built-in potential, the draft of charge carriers overcome the diffusion of charge carriers resulting in the collection of carriers at both electrode.^{4,60,75,91} While the dynamics of exciton still be under the diffusion, because the charge of exciton is zero (the exciton exists without the separation in geometrical spaces). Therefore, the symmetry breaking via built-in potential must be required for charge collection in the organic blend system. Historically, although the origin of V_{oc} is said to be the energy gap between the both quasi-Fermi levels of donor and acceptor materials, numerous researcher regards the trend of practical V_{oc} values would proportional to the maximum of V_{oc} which can be calculated from $HOMO_{donor}$ - $LUMO_{acceptor}$. This empirical result are explained as below.⁷⁰

$$V_{oc} = \frac{1}{e} \left[|E_{Donor}^{HOMO}| - [E_{Acceptor}^{LUMO}] \right] - 0.3 \text{ -----Equation 2.}$$

The 0.3 is an empirical factor from experimental results. However, sometimes the relative HOMO-LUMO energy gap corresponding to V_{oc} is not always the case under practical conditions especially non-fullerene acceptor (NFA), since sometimes the energy transfer mechanism became more significant than the HOMO-LUMO value.

The recent research trend of the bulk heterojunction organic structure focuses on the V_{oc} .^{59,91,92} Since the PCE of organic solar cells (OSCs) still lag behind comparing with inorganic of perovskite based solar cell because of relatively low V_{oc} . The reason of the relatively loss V_{oc} relates with the high loss of photon energy resulting in low V_{oc} .^{18,86,93} In general, the photon energy loss in solar cell can be explained by the equation as below.

$$\Delta E_{loss} = E_g - qV_{oc} \text{-----Equation 3.}$$

Where q is elementary charge and E_g is the optical band gap of the absorber. Because the V_{oc} is determined by the difference of quasi-Fermi level between both electrodes, the subtraction from energy gap which is the excited electron energy level to the converted energy from V_{oc} would be the photon energy loss. From this equation, reducing photon energy loss can be a direct pathway to enhance V_{oc} resulting in enhancement of PCE. The rate of photon energy losses are different with the materials types as crystalline semiconductor, hybrid semiconductor and organic semiconductor. For example, the rate of photon energy loss for gallium arsenide, crystalline silicon and perovskite are 0.32, 0.38 and 0.4-0.5 eV respectively.^{18,94-96} Comparing with these materials, conjugated organic materials shows much larger energy loss with the scale of 0.6-0.11 eV, and these scales is also much higher than the Shockley-Queisser (SQ)

theory (0.25-0.3 eV).⁵⁰ The reason of relatively high energy loss of organic solar cell is high recombination rate of both radiative and non-radiative. The dominant origin of the radiative recombination is due to absorption edge broadening effect by uncoordinated structure of organic materials, while the non-radiative recombination is due to the additional interface between donor and acceptor which do not exist in inorganic or perovskite bases solar cell.⁹⁷⁻¹⁰⁰ The photon energy loss can be divided as three parts (E_1 , E_2 and E_3) as shown in Figure 10. The E_1 is the energy loss about the Shockley–Queisser (SQ) theory which originates the higher energy absorption above the band gap, and the scale of E_1 is known as 0.3 eV. Because the phenomena of E_1 is common including inorganic and perovskite materials, it seems that there are no extra potential to reducing E_1 . The radiative recombination under band gap results on the energy loss as E_2 .^{98,101,102} In case of inorganic or perovskite solar cell, the E_2 is negligible, but the E_2 of OSCs is not. However, although the fullerene based solar cell shows much higher E_2 with the range around 0.7 eV, recent developed non-fullerene acceptor based OSCs also has the negligible E_2 (0.07 V).⁵⁰ It can be a reason that the non-radiative recombination is the dominant factor for relatively higher energy loss in OSCs.

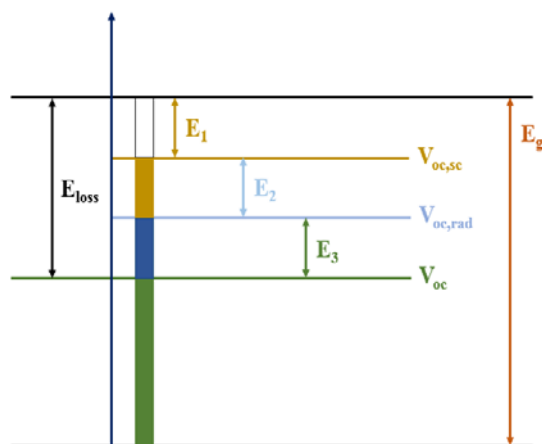


Figure 10. Scheme for photon energy loss analysis in solar cells

The non-radiative recombination is the process which do not radiate the light during recombination, while radiative recombination radiates photon when the electron and hole recombine.^{68,103} There are three types of non-radiative recombination in organic based solar cell as Auger recombination, trap site recombination and bimolecular recombination.^{104,105} The Auger recombination involves three particle system, and the three particles are two electrons and a hole. By the excitation of electron, electron hole pair is generated.^{32,106} The excited electron would recombine with hole, and the recombination radiates energy to out of the electron hole pair system. If there is third particle which is another electron (second electron) nearby the site of recombination, the radiative energy from recombination transfer to the second electron as foster energy transfer which only transfer the energy by energy level overlapping. If the second electron locates on the HOMO level, the second electron excites to LUMO. It is a process which is called as photon recycling. Because the transferred energy is recycled by Auger effect, the photon recycling phenomena is not non-radiative recombination.¹⁰⁷ However, because the quantum yield of photon recycling exponentially degrade with the number of cycle, it can cause the degradation of final quantum yield of OSCs. Otherwise, if the second electron already excites from the light irradiation, the transferred energy just enhance the kinetic energy of second electron to above the LUMO level. The kinetic energy will reduce to LUMO of molecule by the thermal relaxation process. In this process, the photon energy loss occurs as showing like **Figure 11.**

The second type of non-radiative recombination on organic solar cell is trap site recombination.^{4,17,63,80} Although there are no states in the electron forbidden energy

level as band gap of organic materials, defects or trap site can be located in the forbidden energy levels, resulting in trap assisted recombination.^{81,108-111} These trap site are unintentionally introduced on OSC. The trap site recombination is known as the Shockley-Read-Hall (SRH or RHS) recombination.¹¹²⁻¹¹⁴ The excited electron of generated hole by light absorption is trapped on the trap site. Because these trap sites are generally the discrete energy states, the trapped charges involve the restricted charge transport. The restricted charge transport means the increase of probability for recombination. In this case, if the hole also move in the trap site, the trapped electron and hole recombine without the radiation of photon, because the relatively lower energy gap between trapped electron and hole. Even though there are many method to eliminate trap site such as several treatment or morphology control, it is still hard to perfectly eliminate the trap site. Moreover, randomly oriented structure of organic materials also be a dominant reason that there are much more trap site in OSC

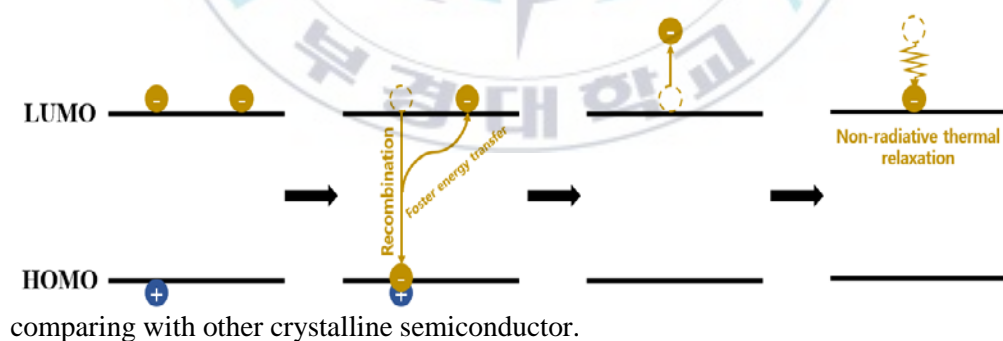


Figure 11. Scheme for process of Auger recombination

The last type of non-radiative recombination on OSC is bimolecular recombination, this recombination is a unique property of the blend system of organic materials, because this the site of the bimolecular recombination is the interface between donor and acceptor.^{14,70} The excited electron on exciton formation has a singlet spin system.

After the exciton separation the changed spin momentum of electron results in the change of spin system to triplet state.^{10,83,84} Because the electron transfers to acceptor and the hole remains in donor, bimolecular condition is constructed at the interfaces. If the separated electrons are still located in donor domain, this recombination would be radiative recombination which is usually observed in direct band gap.^{1,115-117} Because the different phase of electron and hole in the blend system results in the indirect band structure, the bimolecular recombination becomes non-radiative recombination.

These three types of non-radiative recombination are easily observed in numerous type of semiconductor including organic materials.¹¹⁸⁻¹²⁰ However, the effects of these recombination is much different with the types of semiconductor. Unfortunately the organic based solar cell undergo the huge harmful influences from the phenomena of non-radiative recombination comparing with inorganic semiconductor.^{50,121,122} The non-radiative recombination in OSC means the loss of both energy and the number of collected electron. Although this loss causes the degradation of all parameter for solar cell such as J_{sc} , V_{oc} and FF, the most critical parameter which is damaged should be V_{oc} , and the reason can be understand from origin of V_{oc} . As already mentioned, the V_{oc} originates from the difference of Fermi energy level terminal of devices.³³ In general cases, both of the Fermi energy levels well matches with the work function of cathode and anode. However, in solar cell devices, there are quite different Fermi levels because of the influence by irradiation condition.¹²³ Therefore it is required to consider the quasi-Fermi levels which is under the equilibrium state of irradiation.^{124,125} Under the equilibrium state, the continuous creation and excitation of excitons and separated electrons are balanced with the annihilation and relaxation. The creation and excitation

are considered as photo-generation, while the annihilation and relaxation are considered as recombination.^{126,127} Therefore, the V_{oc} is demonstrated from the balance between the photo-generation and recombination. The separated electrons locates on the acceptor domain, and holes locates on the donor domain. This steady state results in the difference of the Fermi energy level for both donor and acceptor. In this situation, the Fermi level has dependency from several factors as the light intensity, the number of generated electrons and hole and so on. The Fermi level which considered the several factors called as quasi-Fermi level in OSCs.

2.2.2 Strategy for Reducing Voltage Loss

Based on the theory of voltage loss in OSCs, it is clear that the reducing of voltage loss by suppressing non-radiative recombination must be required to enhance the power conversion efficiency in OSCs. Generally the strategy for suppressing Auger recombination and bimolecular recombination is the boosting efficient PICT which is directly transferred charge carriers on hot-state. Otherwise, the trap site recombination can be suppressed by elimination of essential trap site by morphology control. Therefore, both energetic approach for suppression of Auger recombination and bimolecular recombination and geometrical approach for elimination of trap site would be accompanied within the blend system of organic materials.

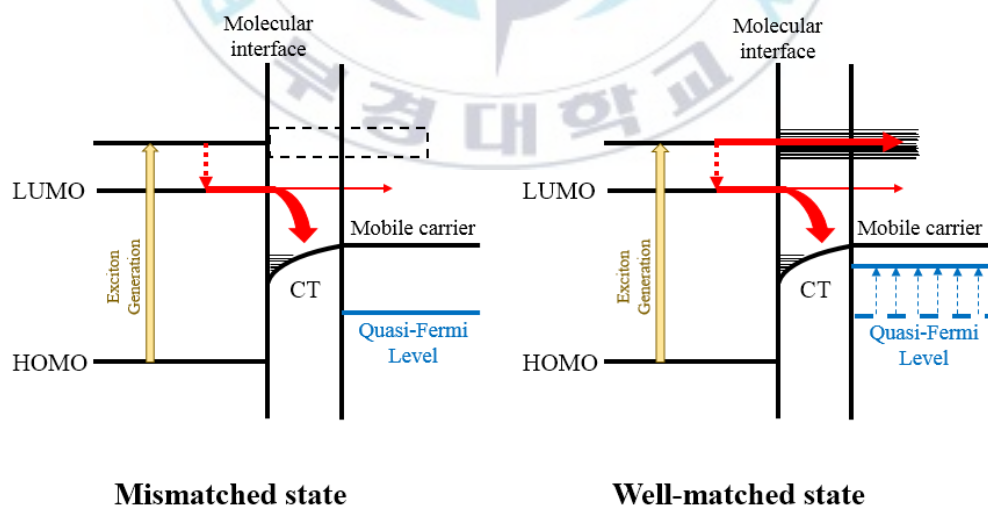
In case of the energetic approach for reducing non-radiative recombination, fundamental strategy is generally focused on reducing the influence of CT states. Because these CT states are dominant site of the Auger recombination and bimolecular recombination, substantial voltage loss originates from the CT states. However, the

targeting of electron states are different between Auger recombination and bimolecular recombination.^{55,128} In case of Auger recombination, because the second electron which are located on HOMO level can undergo photo recycling process, the only excited second electron which radiate energy as thermal relaxation process is considered.^{50,85} Therefore, the targeting electrons for reducing Auger recombination would be an excited electrons on hot-states before thermal relaxation. In this process, the hot-state charge transfer can suppress the voltage loss.¹⁵ This means that the efficient PICT on hot-state can be one of the strategy for enhancement voltage loss. These efficient PICT reduce the probability of trapping in CT states, because the charge transfer process occur on the hot-state which has the higher kinetic energy of electron.^{3,129,130} Otherwise, in case of bimolecular recombination, the bimolecular formation of electrons and holes pair which are located at sub-band gap is only considered. Because even though there is an attractive force between electron and hole pair, the charge carriers which are on upper energy level than sub-band gap have enough kinetic energy to overcome the binding of electron and hole pair.¹³¹⁻¹³³ However, it is well known that the electrons which are on the bounded CT states is weekly dependent on the external bias or excess energy for electrons. Therefore, the strategies as energy favorable material property or morphology control must be required.

One of the most effective strategy of energetic approach for reducing Auger and bimolecular recombination is enhancing the amount of hot-state matching between donor and acceptor. The key point of this strategy is enhancing the rate of hot-state charge transfer before relaxation, resulting in the suppression of the charge transfer on CT states under LUMO level, and it requires the enough hot state matching for

delocalization of electrons on hot-state. This means that if the density of states for excited electron of donor considered as the charge generation states, the corresponded density of states (DOS) for acceptor must be required for delocalization overall the blend system. The corresponded density includes both of the intensity and energy of DOS.^{70,134}

Otherwise, the effective strategy of geometrical approach would be a post treatment for the film of blend system. Because the general conjugated organic materials easily diffuse from the non-polar solvent such as chlorobenzene, solution process for the film fabrication such as spin coating and inkjet method is applied.^{4,16,53,135,136} Since the diffused state of organic materials in solution has randomly blended state, the post treatment can control the quality of film such as percolation network, morphology and stacking type.



Mismatched state **Well-matched state**
Figure 12. Charge transfer mechanism on mismatched and well-matched states

2.3 Device Physics for Bulk heterojunction Organic Solar Cell

The final purpose of solar cell is converting the photon energy to electric energy. Therefore the efficient for light to electrical power conversion would be the most important factor of performance for solar cell.^{14,55,137} The most widely used method to determine the power conversion efficiency (PCE) is the current density-voltage (J - V) characteristics.^{3,35,138} The J - V characteristics is a measurement for photo diode property under irradiation condition. In this analysis, current densities at each external voltage are measured. Because the organic solar cell is diode, saturated current would be observed around “0” external bias. While the current density increase unlimitedly at the driving voltage as shown in blue line in dark condition. In case of irradiation condition, current density shows negative value as red line because of self-generated charge carriers in solar cell. In J - V characteristics, PCE can be simply calculated by using the short circuit current density (J_{sc}), open circuit voltage (V_{oc}) and fill factor (FF) by using the PCE equation below.^{46,55,70,87,119,139}

$$PCE = \frac{P_{out}}{P_{in}} = \frac{V_{oc} \times J_{sc} \times FF}{P_{in}} \text{-----Equation 4.}$$

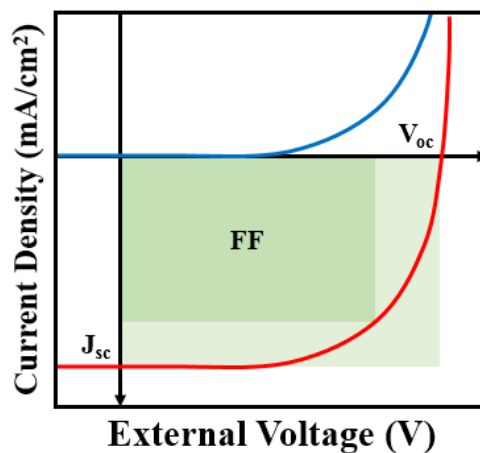


Figure 13. J - V characteristics of solar cell

The general Shockley equation which is modified for solar cells are shown as follow.

$$J(V) = J_0 \left[\exp\left(\frac{q(V - JR_S)}{n_i k_B T}\right) - 1 \right] + \left[\frac{(V - JR_S)}{R_{Sh}} \right] - J_{ph} \text{-----Equation 5.}$$

Where, J_0 is the reverse saturation current density, V is the applied bias, k_B is Boltzmann constant, n_i is the effective light ideality factor, R_S is series resistance, R_{SH} is shunt resistance, T is temperature and J_{ph} is self-generated current density from light. The first term of Shockley equation shows the Shockley equation for ideal diode, and the second term is for effect of resistance. Because the Shockley equation is for current density from external bias, the third term of J_{ph} should be negative.

In J - V characteristics, J_{sc} means the current density of device at “0” external bias. This means that the J_{sc} is the maximized current density which generated by the solar cell. This J_{sc} can be explained by Shockley equation as “ $J_{SC} = -J_{ph} = -edGP_c(I, V)$ ”. Where G is the rate of generated free charge carriers per unit volume, d is the distance between each electrode, and $P_c(I, V)$ is the probability of charge collection. The short circuit is a condition for actual performing state of solar cell. Therefore, the J_{sc} shows the rate of charge generation, and the J_{sc} usually depends on the photon absorption. As shown in J_{sc} explanation of Shockley equation J_{sc} has linear dependency on the light intensity. However, in actual devices, the current density which is generated by photon do not show the linear dependency because of charge collection part as like “ $J_{ph} = \alpha P_{in}^\alpha$ ”. When α is “1”, the most of the generated charges collects on electrode without the recombination. While α under “1” as the general devices means that the generated charge carriers loss from the difference of the carrier mobility for electrons and holes, bimolecular recombination and the variations in the distribution of density of states.

The V_{oc} indicates the voltage when the external bias make current density “0”. In the irradiation conditions the active layer of solar cell has built-in potential, the built-in potential is constructed from the quasi-Fermi energy level difference between cathode and anode. If the external bias which is reverse direction with built-in potential, the built-in potential offsets by the external bias. Therefore the V_{oc} is same with the built-in potential including quasi-Fermi energy level condition. From the general Shockley equation for photovoltaics, V_{oc} can be represented as “ $V_{OC} = \frac{n_i k_B T}{q} \ln \left(\frac{J_{ph}}{J_0} + 1 \right)$ ”. The equation shows that V_{oc} has the inversely proportional relation with J_0 while directly proportional relation with J_{ph} and n_i . Because the closed relation between V_{oc} and J_{sc} , the light intensity dependent V_{oc} is used for the analysis of the recombination mechanism within devices. According to the Shockley equation, the slope of the V_{oc} versus $\ln(I)$ plot is corresponding to $\frac{n_i k_B T}{q}$. Hence, the ideality factor (n_i) of 1 indicates that the bimolecular (Langevin) recombination is dominant, while the n_i of 2 indicates the SRH (trap-assisted) recombination is dominant at open circuit condition. In general, the n_i ranges from 1 to 2, suggesting that recombination at open circuit is a combination of SRH and bimolecular process. Fill factor (FF) is calculated from the ratio between the maximum power of the solar cell and the product value of J_{sc} and V_{oc} . In the ideal solar cell, the maximum power would be the product of J_{sc} and V_{oc} . However, when the carrier extraction is not a unity, the maximum power should be lower than it. Because the carrier extraction depends on carrier mobility, resistance and recombination, FF shows these all informations as final formation. It is a main reason that the quality of solar cell are generally decided by the FF . The FF can be calculated by the equation as

$$“FF = \frac{V_{max} \times I_{max}}{V_{OC} \times I_{SC}}”.$$

CHAPTER 3 EXPERIMENTAL

3.1 Material Preparation

<P1 and P2 Synthesis>

To the ice cold solution of **5** (1.20 g, 1.76 mmol) in anhydrous toluene (40 mL) was added 2-octyldodecan-1-amine (0.57 g, 1.90 mmol) drop by drop via syringe under an argon atmosphere. The solution was stirred for 1 h and then slowly heated to reflux for 10 h. Toluene was completely removed and the residue was dissolved in dry methylene chloride (50 mL) and cooling. To the stirred solution, 5.0 mL of thionyl chloride was added in one portion and then heated. After 30 min, the solution was completely removed by rotary evaporation. The pasty mass was dissolved in methylene chloride (50 mL) and washed with brine. The organic layer was dried over anhydrous Na₂SO₄. The solvent was concentrated and then the residue was purified by column chromatography (silica gel, hexane:ethyl acetate, 90/10, v/v) to afford pure product ttPPD as a yellow solid. A solution of BDTT (0.27 g, 0.30 mmol) and ttPPD (0.29 g, 0.30 mmol) were dissolved in chlorobenzene (20 mL). The solution was purged well with argon for 45 min and then Pd₂(dba)₃ (7 mg) and P(o-tol)₃ (15 mg) were added in one portion. The entire mixture was stirred and refluxed for 16 h under argon atmosphere. Subsequently, the reaction mixture was cooled to RT and then added drop by drop into a vigorously stirred methanol (200 mL). The precipitates were recovered by filtration, and the crude polymer was extracted with methanol and acetone for 24 h each in a Soxhlet apparatus to afford pure polymer P(BDTTttPPD) as a dark brown solid. Yield (0.39 g, 94%).

<Polimerization>

Polymerization of poly[2,6-(4,8-bis(2-ethylhexyloxy)benzo [1,2- b:4,5-b']dithiophene) -alt-1,4-(7,8-bis((2-ethylhexyl)oxy)- 2-fluorophenazine)] (PBDT-FPz). The 1,4-dibromo-7,8-bis((2-ethylhexyl)oxy)- 2-fluorophenazine (3) (0.238 g, 0.492 mmol) was added to chlorobenzene (20 ml), then 2,6-bis(trimethyltin)- 4,8-bis(2-ethylhexyloxy)benzo[1,2-b:4,5-b']dithiophene (0.3 g, 0.388 mmol) and Pd catalyst that tris(o-tolyl)phosphine (0.080 g, 0.0246 mmol) and Pd₂(dba)₃ (0.0226 g, 0.0246 mmol) put into flask. This solution was stirred 48 h at 100 °C condition. After cooled to room temperature, this solution was put into stirred methyl alcohol at 0 °C one by one. The polymer was filtered and washed with methanol. The collected polymer was soxhlet-extracted with methanol, acetone, chloroform and chlorobenze. Then, chloroform and chlorobenzene solutions were put into stirred methanol to reprecipitation. The purified polymer was collected by filtration to give 240 mg.

<Others>

Reagents and solvents were purchased from Sigma-Aldrich. PCE10 (PTB7-Th), PCE11 (PffBT4T-2OD), PBDB-T, PBDB-T-2Cl, PCDTBT, Si-PCPDTBT, series of IEICO were purchased from one-Material. F-N2200, PC71BM, PCBM, C₆₀, Y6 were purchased from nanocleanTec.

3.2 Device Preparation

ITO-coated glass substrates were sequentially cleaned in an ultrasonic bath with deionized water, acetone, ethanol and isopropanol for 10 minutes and then dried in the oven at 100 °C for overnight. The surface of the substrates were then treated with UV/Ozone treatment for 1800 s, thereafter poly(3,4-ethylenedioxythiophene)-poly(styrene sulfonate) (PEDOT:PSS, Paytron PH) was spin-coated onto the substrate at the 4500 rpm for 50 s and annealed at 140 °C for 10 min. A polymer blend of electron donor (P1, P2, PTB7-Th and PBDB-T) and electron acceptor (PC71BM, ITIC and IEICO-4F) at various ratios was dissolved in chlorobenzene (CB): 1,8-Diiodooctane (DIO) (97:3 vol%) and thereafter spin-coated on top of the PEDOT/PSS layer. Specifically, the D18:Y6:PCBM blend was dissolved in chloroform (CF): 1-chloronaphthalene (CN) (99:1 vol%). After coating the active layer, it was washed by 0.2 ml methanol via spin-coating at 3000 rpm for 30 s. Lastly, 100 nm of Al electrode was deposited by thermal evaporation in vacuum of approximately 3×10^{-6} Torr.

3.3 Analysis

<Optoelectrical analysis>

The UV-Vis absorption spectra of conjugated polymer and small molecule materials was measured by a T70+ UV/vis spectrometer. The saturated V_{oc} and light intensity- dependent V_{oc} were measured under monochromatic light by using Xenon lamp (Dongwoo optron). The irradiated current density–voltage (J – V) curves were tested using Keithley 2400 under air mass 1.5 global (AM 1.5G) irradiation (100 mW cm^{-2}). The light intensity was calibrated using the NREL-Si solar cell.

In order to calculate the MF, the two assumptions are applied to our study. 1) The information of the full-range density of state (DOS) of unoccupied molecular orbital replaces to the optical density of organic materials; although electrical DOS is not exactly the same as optical DOS, the optical density in quantum theory results from a mixing of suitable excited state wave functions with the ground state wave function. 2) Every electrons at ground states locates at the highest occupied molecular orbital (HOMO) level of organic materials. Based on the two assumption the MF can be simply calculate. The energy of excited electrons can be express by summation of HOMO level and photon energy ($h\nu$) as shown equation (1). If the number of optical state at i energy level are N_i , the optical density at i energy level should be express as form as equation (4). Then we defined MF at i energy level from subtracting from optical density of donor to optical density acceptor as shown as equation (5). The integrated MF are calculated from LUMO of donor to vacuum energy level as equation (6).

$$E_{excited\ electron} = E_{HOMO} + h\nu \quad (1)$$

$$N_i E_{excited\ electron} = N_i (E_{HOMO} + h\nu_i) \quad (2)$$

$$N_i E_i = \frac{D(E_i)}{dE_i} E_i = N_i (E_{HOMO} + h\nu_i) \quad (3)$$

$$D(\epsilon) i = \int_i N_i dE_i \quad (4)$$

$$MF_i \equiv D_{Donor}(\epsilon)_i - D_{Acceptor}(\epsilon)_i \quad (5)$$

$$Integrated\ MF = \int_{LUMO\ of\ donor}^0 |D_{Donor}(\epsilon)_i - D_{Acceptor}(\epsilon)_i| dE \quad (6)$$

<Transient absorption spectrometer>

Steady-state absorption and photoluminescence (PL) spectra were obtained using a Hitachi UH5300 UV–vis absorption spectrometer and Ocean Optics QEPro spectral analyzer, respectively. Atomic force microscopy (AFM) images were obtained using a tapping-mode AFM spectrometer (XE-100, Park Systems Corp). Femtosecond transient absorption (TA) and transient absorption anisotropy (TAA) spectra were recorded using a home-made TA measurement system, comprising a 1-kHz repetition rate femtosecond Ti:sapphire regenerative amplifier system (Hurricane, Spectra Physics), an infrared optical parametric amplifier (OPA-800CF, Spectra Physics), and multichannel spectrometers (Ocean FX, QEPro, and NIRQUEST; Ocean Optics). More details regarding this system have been provided elsewhere.² For the TAA decay ($r(t)$) measurements, the white-light continuum probe pulse was horizontally polarized using a sheet polarizer. The pump pulse was subsequently changed to yield parallel or perpendicular polarization using a liquid crystal polarization rotator (LCR1-633, Thorlabs) with respect to the polarization of the probe pulse. Finally, TAA decay was evaluated using the equation, $r(t) = (\Delta A_{HH}(t) - \Delta A_{HV}(t)) / (\Delta A_{HH}(t) + 2\Delta A_{HV}(t))$, where the variable represents the TA amplitude.

CHAPTER 4

STUDY ON CHARGE TRANSPORT BETWEEN DONOR AND ACCEPTOR

4.1 Introduction

In a two organic materials system such as organic photovoltaics (OPVs), photon absorption of the conjugated organic materials generates Frenkel excitons which are strongly bounded at room temperature.^{61,140} In order to generate mobile carriers by dissociation of Frenkel excitons, the photo-induced inter-molecular charge transfer (PICT) requires, by its nature, the ionization potential of excited states of donor, electron affinity of the acceptor and the Coulomb energy of separated radicals including polarization effects.^{8,28,89} Fundamentally, PICT is an ultrafast charge transfer which results in the delocalized coherent superposition of Eigen functions between donor and acceptor materials.^{14,17} In order to accomplish the efficient PICT, many researchers have studied the carrier dynamic at interface between two or more organic materials system. Richard H. Friend et al. demonstrated that the efficient organic photo-conversion occurs through hot-state charge delocalization.²⁴ They also demonstrate that both geometrical and energetic accessible delocalized state matching around the lowest unoccupied molecular orbital (LUMO) level are key factors to generate mobile carriers. Furthermore, Alan J. Heeger et al determined that there are two kinds of process for PICT, 1) the directly generated mobile carriers by ultra-fast charge transfer and 2) two steps process which includes intermediate charge transferred state by Coulomb energy of positive and negative carriers.³ Consequently, delocalized “hot-state matching” is crucial for directly generated mobile carriers. However, most of studies have been

focused on only near LUMO levels of both donor and acceptor, hence the electron dynamics coexists with complicated relaxation dynamics at the higher level than LUMO level of donor. In this fundamental, what happens at the higher energy levels than LUMO for PICT could be a crucial question, but it is still hard to understand at the two organic material system.

In this study, we focused not only on the vicinity of the LUMO level but also the full range of unoccupied molecular orbitals to achieve the efficient PICT. We assume that the directly generated mobile carriers which is one of the charge transfer process occurs efficiently at the well matched state. In order to demonstrate the correlation between hot-state matching and efficient PICT, the three assumptions are applied to our study. 1) V_{oc} manifests an equilibrium states including both carrier dynamics and relaxation dynamics; the timescale of V_{oc} measurement is order of magnitude slower than both carrier transfer and relaxation timescale (i.e. the continuous irradiation of photons, not one electron dynamics, maintains the filled states as the equilibrium states). 2) The information of the full-range DOS of unoccupied molecular orbital replaces to the optical density of organic materials; although electrical DOS is not exactly the same as optical DOS, the optical density in quantum theory results from a mixing of suitable excited state wave functions with the ground state wave function. 3) Every electrons at ground states locates at the highest occupied molecular orbital (HOMO) level of organic materials. From these assumptions, the definition of hot-state matching is established as the overlapped areas of the optical density for the each organic materials. And absolute energy level of excited electrons is represented by the sum of HOMO level and energy of photons which have particular wavelength.

4.2 Result and Discussion

4.2.1 Hot-state matching formations at the two organic materials system

For the PICT at the two organic materials system, electrons should be on the delocalized states of Eigen functions between donor and acceptor materials. This fundamental theory indicates that the poor states of the acceptor domains restricts the delocalization to only donor sites, hence the existence of states on the acceptor at corresponding energy levels is essential for the delocalized electrons transfer under the fundamental of the uncertainty principle. Here, we assume that the delocalization under the equilibrium states may rely on the hot-state matching formation between the donor and the acceptor.

Hot-state matching between the donor and acceptor in the BHJ is one of the important factors to increase the rate of efficient PICT. Because generated electrons should move from the electron donor to the electron acceptor at the interface via PICT, well-matched energy state at the interface leads to efficient electron transfer. In this case, the amount of overlapping of the energy states between the donor and acceptor significantly affects the PICT efficiency of the BHJ. **Figures 14(a) and (b)** illustrate two possible PICT processes in BHJ systems with mismatched and well-matched states of the donor and acceptor at their interfaces. In both cases, electrons in the donor are directly excited to the hot-state level from the HOMO level via the absorption of photon energy (vertical yellow arrows) and then delocalized on the hot states. If there are no states with the same energy level as the hot state in the acceptor (**Figure 1(a)**), the excited electron spontaneously relaxes toward the thermally stable LUMO level of the

donor and is subsequently transferred to the LUMO level of the acceptor via CT states. In this case, owing to the existence of substantial CT states at levels lower than the LUMO level of the acceptor, large numbers of electrons are trapped at the lowest-lying CT states during the transfer process. Because the probability of non-radiative recombination increases at the lowest-lying CT states, the trapped electrons are rarely transferred to the mobile carrier state.

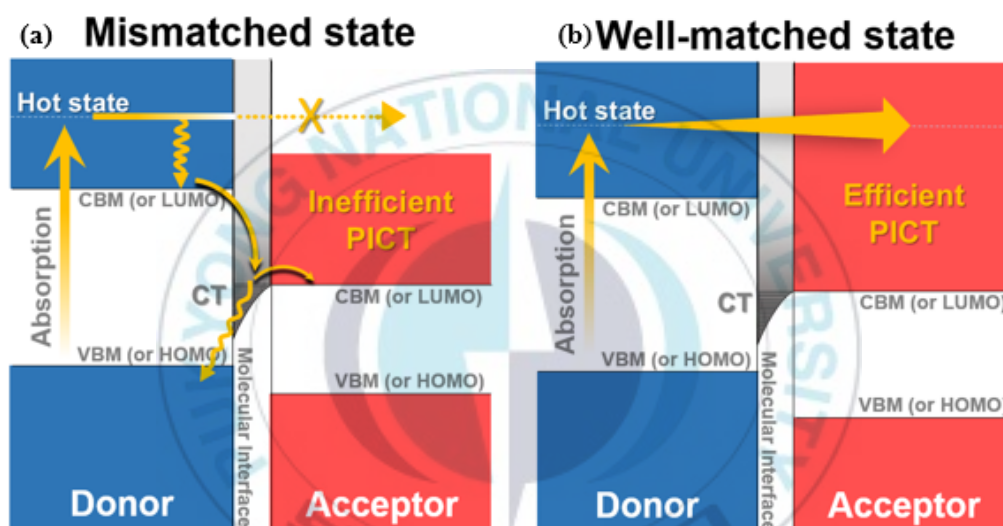


Figure 14. Mechanism of PICT at mismatched state and well-matched state.

By contrast, the excited electrons at the hot state can be transferred to the energy state in the acceptor directly before the relaxation if there are states with the same energy level as the hot state in the acceptor, as shown in **Figure 1(b)**. In this case, a significantly larger number of mobile carriers are generated via the efficient PICT process without trapping at the CT states. Considering this aspect, ensuring energy-state matching at the BHJ interface is a critical factor for affecting the PICT efficiency. Developing effective methods for identifying the degree of state matching in the BHJ is crucial. Although the importance of hot-state matching has been verified by numerous studies, no method for the quantification and visualization of state matching

has been reported. Thus, we developed a simple and effective method to quantify and visualize the hot-state matching for ensuring efficient PICT.

Figure 15 illustrates an energetic scheme of the formation of the hot-state matching for PICT. The yellow arrows represent the electron transfer, and yellow dash lines means the delocalization area of electrons. **Figure 15** presents three possible hot-state matching formations under the equilibrium states. Area I is the only acceptor rich states; although the DOS population of hot-state to accept the delocalized electrons is sufficient, the low absorption by the poor donor states generates less excited electrons at the corresponded energy level. Otherwise, at the only donor rich states marked as Area III; although excitations occur sufficiently at donor states, the delocalization for the directly generated mobile carriers is restricted within donor sites represented as the dash line because of poor acceptor states. Since the excited electrons locate on the restricted delocalized states, the electrons in Area III should be relaxed toward the thermally stable state as LUMO level of donor, and the electrons have to transfer near LUMO level which has the strong influences on charge transfer state (CT). Given that the CT states are the intermediate states which are bound states by electrical attraction force of electrons and holes which causes the non-radiative recombination.

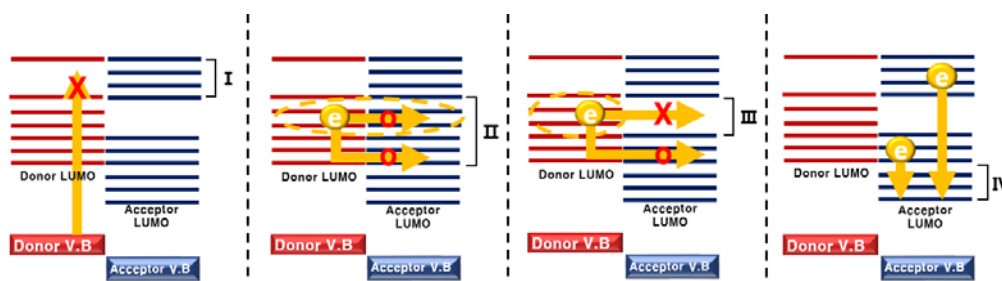


Figure 15. Energetics of the formation of hot-state matching for PICT.

From our expectation, the best condition for the directly generated mobile carriers is Area II which has the both rich states at the donor and acceptor; the number of excited electrons are sufficient, and the delocalized states is matching well along all over the donor and acceptor sites. By the directly generated mobile carrier transfer, the number of degenerated mobile carriers which are on the each donor and acceptor determines the quasi-Fermi energy levels. Moreover, this directly generated mobile carriers have less influence from CT states comparing with Area III, hence long-range dissociation occurs at higher level from the higher kinetic energy of carriers. Consequently, the well matched hot-state formation as Area II results to the efficient PICT for the directly generated mobile carriers.

4.2.2 Quantification of the hot-state matching in organic blend system

In order to apply the hot-state matching on the blend system, quantification of the hot-state matching involving not only LUMO level but also broad range of electron energy level must be calculated for balanced density of states between donor and acceptor, and the balance of state density could be simply calculated from ODO between donor and acceptor. **Figure 16** shows a novel and reasonable methods to quantify and visualize the hot-state matching for broad range of electron energy level by using ODO and mismatching factor (M.F).

Figure 16 shows the developed method to quantify and visualize hot-state matching. According to the optical density overlapping (ODO) and energy-level matching at the interface of the donor and acceptor, we calculate the MF to quantify the degree of energy-state matching. **Figure 16** shows ① the pristine ODO between the donor and

acceptor; the OD spectra of the donor and acceptor were easily obtained by measuring the ultraviolet–visible absorption. The red and blue lines indicate the ODs of the acceptor and donor, respectively. The yellow area is an area of the ODO between the donor and acceptor. In this case, we can easily obtain information regarding the intensity of the OD and the energy bandgap between the valence-band maximum (or HOMO) and conduction-band minimum (or LUMO).

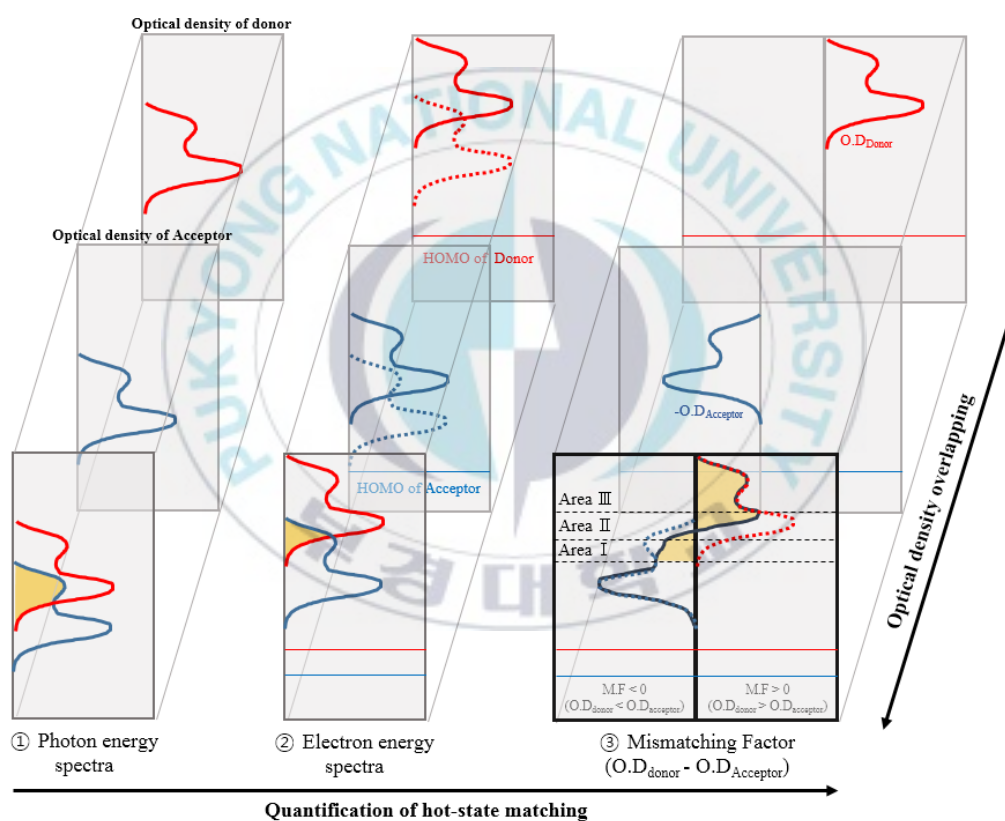


Figure 16. Scheme for mismatching factor from photon energy spectra and electron energy spectra.

However, because the ODO does not include information of the corresponding electron energy level, it is difficult to understand hot-state matching using only ODO information. Therefore, we need additional information regarding the corresponding

energy level of the valence-band maximum (or HOMO) to calculate the energy state of ODO for investigating the charge transfer from the donor to the acceptor. Therefore, in this study, we suggest the MODO calculated via the summation of the OD and HOMO level of each material. For the reliability of HOMO values, HOMO values of each materials are calculated by using UPS measurement as shown **Figure 17**. Because the targeting of calculation of MODO are thin film, UPS measurement are proper to show exact HOMO level of thin film.

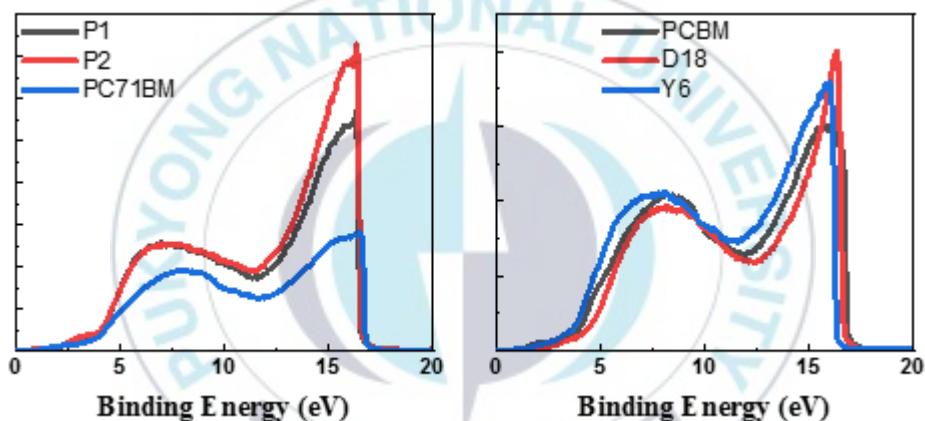


Figure 17. UPS measurement for P1, P2, D18, PCBM, PC71BM and Y6

The sum of the absorbed photon energy and HOMO level for each material is depicted in ② MODO of **Figure 16**. The yellow area in ① indicates the pristine ODO between the donor and acceptor, whereas the yellow area in ② indicates their MODO. As expected, the overlapping areas of ① ODO and ② MODO differ significantly. Although the shape of each modified optical density (MOD) is identical to that of the OD, the degree of overlapping differs significantly between the ODO and MODO, which originates from the difference between their HOMO levels. Because the MODO

implies energy-level matching between the donor and acceptor, the area of the MOD₀ indicates the degree of hot-state matching.

To visualize and quantify the hot-state matching effectively, we define the MF. The MF is calculated by subtracting the MOD for the acceptor from the MOD for the donor ($MF \equiv MOD_{Donor} - MOD_{Acceptor}$) at each electron energy level, as shown in ③ of **Figure 16**. A positive MF value indicates that $MOD_{Donor} > MOD_{Acceptor}$ at the corresponding energy level, whereas a negative MF value indicates that $MOD_{Donor} < MOD_{Acceptor}$ at the corresponding energy level. An MF value of zero indicates that $MOD_{Donor} = MOD_{Acceptor}$, suggesting well-matched energy levels of hot-state matching. Because the electron should be transferred from the donor state to the acceptor state, we calculated the MF values in only the range of the MOD of the donor, which is depicted in ③ of **Figure 16**. The area of the MF is divided into three parts: areas I, II, and III. Area I is the MOD_{Acceptor}-rich area (negative MF), and area III is the MOD_{Donor}-rich area (positive MF). Area II corresponds to the balanced state matching area with a small MF value, and the MF value changes significantly in this area as shown yellow box in ③ of **Figure 16**. The area II is selected by consideration of two conditions. The first condition is the including the point of ' $MF=0$ '. Based on definition of MF, zero point of MF means the energy level which have same optical density of donor and acceptor. However, the energy level which has any optical density of donor and acceptor also has "zero" value of MF as zero point at area III or electron forbidden zone of donor as shown **Figure 16**. Therefore, the additional condition as ' $dMF/dE \gg 0$ ' should be required to select area II. Both areas I and III imply mismatched states, and efficient PICT is difficult to achieve in these areas. However, electrons in the donor can be transferred efficiently to

existing energy states in the acceptor via efficient PICT in area II. Therefore, using the MF value, we can easily estimate the degree of energy-state matching at the interface between the donor and acceptor.

In order to calculate the MODO and MF, the donor materials are selected as P(BDTT-ttDPPDt) (P1) and P(BDTT-BTBDPPD) (P2), equivalent LUMO levels with the different shape of optical density of the unoccupied molecular orbitals, to demonstrate the hot-state matching of the blend system with PC71BM. The molecular structures are shown as **Figure 18(a)**. Both donor materials are based on 4,8-bis(5-(2-ethylhexyl)thiophen-2-yl)benzo[1,2-b:4,5-b'] dithiophene (BDTT) and pyrrolo-[3,4-c]pyrrole-1,3-dione (DPPD) with adjustments of the thiophene numbers and frequency, these adjustments lead to a OD distinction of donor materials. The energy levels of P1, P2 show a nearly equivalent optical bandgap (P1=2.04 eV, P2=2.08 eV), and LUMO levels of two donor materials are -3.37 eV and -3.36 eV respectively.

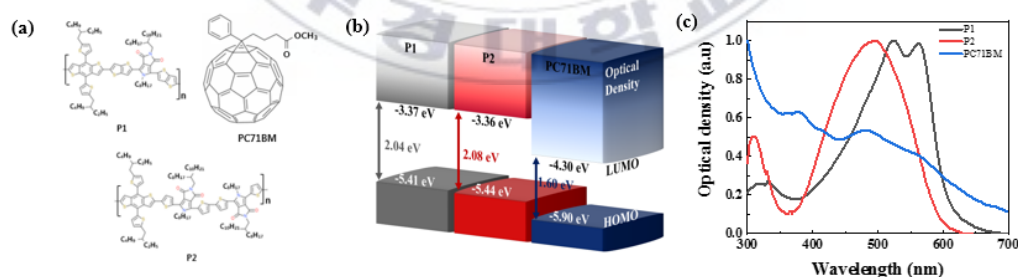


Figure 18. Material and optical properties of P1 and PC71BM. (a) Molecular structures of P1, P2 and PC71BM. (b) Energy-level diagram with optical density of P1, P2 and PC71BM. (c) Absorption spectra of P1, P2 and PC71BM

The distinction of optical density are shown in absorption spectra (**Figure 18(c)**). The most populated absorption peak of P1 has the red shift comparing with P2, and P1 spectra has the more narrow absorption peak. In order to match the optical density

between the donor and acceptor, the sum of optical density and energy of HOMO level is represented as the energy spectra. Since a relativity of the configuration at absolute energy levels is adjusted by HOMO levels of each donor and acceptor materials, both absorption spectra and energy spectra should have a distinction. At the absorption spectra, a main peak of P1 which is in the region from 400 to 600 nm overlaps the 480 nm peaks of PC71BM, but the 480 nm peak is out of the main peak of P1 at the energy spectra. As shown in the absorption spectra and energy spectra, the normalized DOS intensity of the 480 nm peak of PC71BM is nearly 0.5, and the 375 nm peak is nearly 0.6. Because the DOS values are different at the absolute energy levels, the DOS matching which are calculated from overlapped area should have a dependency by material configurations.

The configuration of energy level diagram and the optical density distribution is represented at **Figure 19**. As shown in **Figure 19**, optical density is divided with three parts by the normalized intensity; Dark blue areas, light blue areas and light blue lines show the normalized optical density as 0.6~1, 0.3~0.6 and 0.1~0.3 respectively. And the red lines indicate the energy level which has the most populated optical density. At **Figure 19**, the hot-state matching formations also be shown as the energy levels, and the area which are overlapped with both dark blue should be Area II (well-matched states). The Area II of P1: PC71BM blend covers from -2.8 to -3.2 eV, and P2: PC71BM blend covers from -2.5 to -3.14 eV. The result shows that the Area III of P2: PC71BM (0.64 eV) blend is wider than the P1: PC71BM (0.4 eV). From our research concept, the energy level diagram with hot-state matching imply that P2: PC71BM blend is much more suitable condition to generate the directly generated mobile carriers.

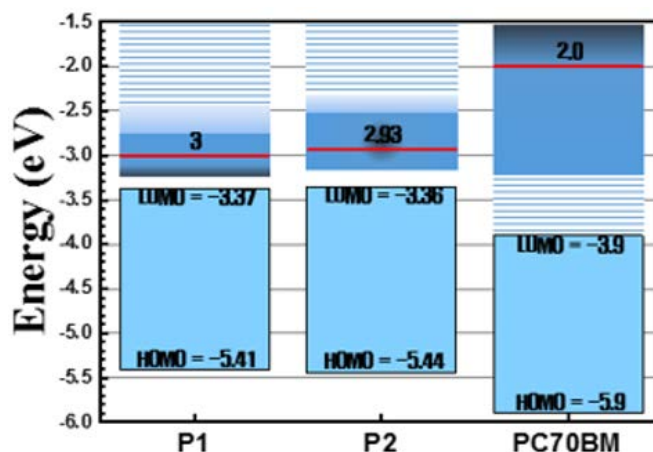


Figure 19. Energy level diagram with OD of the unoccupied molecular orbitals. Bright blue squares are band gaps / Dark blue area, light blue area, light blue line shows normalized optical density 0.6~1, 0.3~0.6 and 0.1~0.3 respectively.

The converted ODs of P1 and PC71BM on the incident-photon energy scale are shown in **Figure 20(a)**. P1 exhibits the highest OD at 2.4 eV (black line), and PC71BM exhibits the peak of OD at 2.5 eV (blue line). The OD of P1 is overlapped in the range of 2.0–4.0 eV with the OD of PC71BM, and the highest overlapped photon energy is nearly 2.5 eV (marked by a star symbol). Vertical arrows in **Figure 20(a)** indicate the corresponding OD intensities of both materials when a photon having energy of 2.5 eV irradiates the materials. The OD values are 0.8 and 0.5 for P1 and PC71BM, respectively.

Figure 20(b) shows the MODs of P1 and PC71BM calculated via the summation of the HOMO level and bandgap for each material. The HOMO levels of P1 and PC71BM are -5.41 and -5.90 eV, respectively. When the materials absorb incident photons with an energy of 2.5 eV, electrons in P1 can be excited to hot states with an energy of -2.91 eV from its HOMO levels of -5.41 eV, whereas electrons in PC71BM

are excited to an energy state of -3.4 eV from its HOMO of -5.9 eV. The yellow area in **Figure 20(b)** indicates the area of MODO between P1 and PC71BM, which differs significantly from the ODO of **Figure 20(a)**. The MOD of P1 is higher than that of PC71BM in the range between -2.75 and -3.4 eV, whereas the MOD of PC71BM is higher above -2.75 eV and below -3.4 eV; the MODs are identical at -2.75 eV (marked by a triangle symbol).

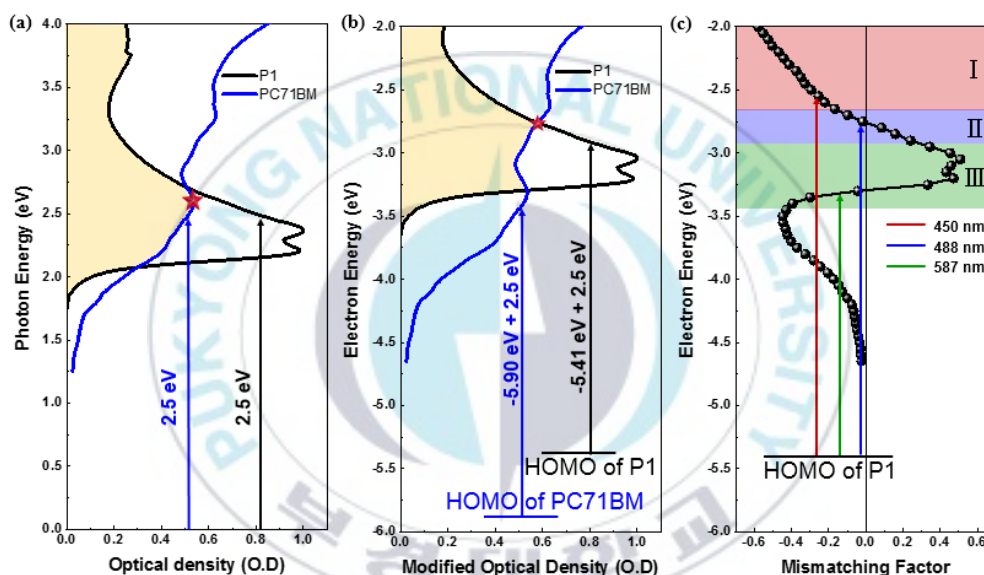


Figure 20. Material and optical properties of P1 and PC71BM. (a) OD of P1 and PC71BM. (b) MOD of P1 and PC71BM. (c) Mismatching factor at each electron energy level for P1:PC71BM.

To visualize the quantity of the MODO, we calculated the MF for the BHJ of P1:PC71BM. **Figure 20(c)** shows the calculated MF for P1:PC71BM (black line) at each energy level. The MF is simply calculated by subtracting the MOD for the PC71BM acceptor from the MOD for P1. The MF is zero at -2.75 eV for P1:PC71BM. As explained previously, the MF of zero indicates that the two MODs are equal and that the energy states at their interface are ideally matched. According to the degree of

the MODO, we defined three matching formations, i.e., areas I, II, and III (red = area I, blue = area II, and green = area III), in the P1:PC71BM blend system. In area I, considerably more states exist in the PC71BM acceptor than in P1. Although the electrons in the P1 donor can be directly transferred to the state in PC71BM before lattice relaxation via the matched state in PC71BM in this case, the relatively low MOD of the P1 donor results in insufficient excitation of P1 and consequently limits the number of generated charge carriers. By contrast, the smaller number of states in PC71BM compared with P1 restricts the charge delocalization of electrons in P1 in area III, causing inefficient PICT. Well-matched energy levels of P1:PC71BM with a small MF value between -0.2 and $+0.2$ are obtained in area II, where the intensities of the two MODs are similar.

4.2.3 Correlation between Hot-state matching and PICT

Here, two donor materials and three acceptor materials are selected to calculate the MODO and MF. The candidates of donors are PTB7-Th and series of PBDB-T, and IEICO-4F, PC71BM and ITIC for acceptors. Numerous researchers are focused on the sum of optical density to improve the photocurrent (J_{sc}) via broad range of complementary absorption even near infrared ray (IR). Here we suggest the novel method by using the subtractions of intensity of hot-state at corresponded energy level with the consideration of both HOMO levels. As already shown at P1 and P2, the population of OD at corresponding energy level for each materials can be represented as the energy level diagram shown in **Figure 21**. The NFA materials have a similar property on the OD shape as that the highest populated OD peaks are located near HOMO level within the energy differential from 0.2 to 0.4 eV, and the widths of Area

II are nearly 0.3 ~ 0.6 eV. Otherwise in cases of PCBM series, the highest populated OD peak (-2 eV) is located at far away from HOMO level (-3.7 ~ -3.9 eV), and the width of Area II covers wide range of donors. Because of this distribution of OD, the Area II of NFA acceptors such as series of ITIC and IEICO-4F are narrower than the series of fullerene. And the main peaks of acceptors are located at deeper levels than HOMO of donors (under -3.6 eV).

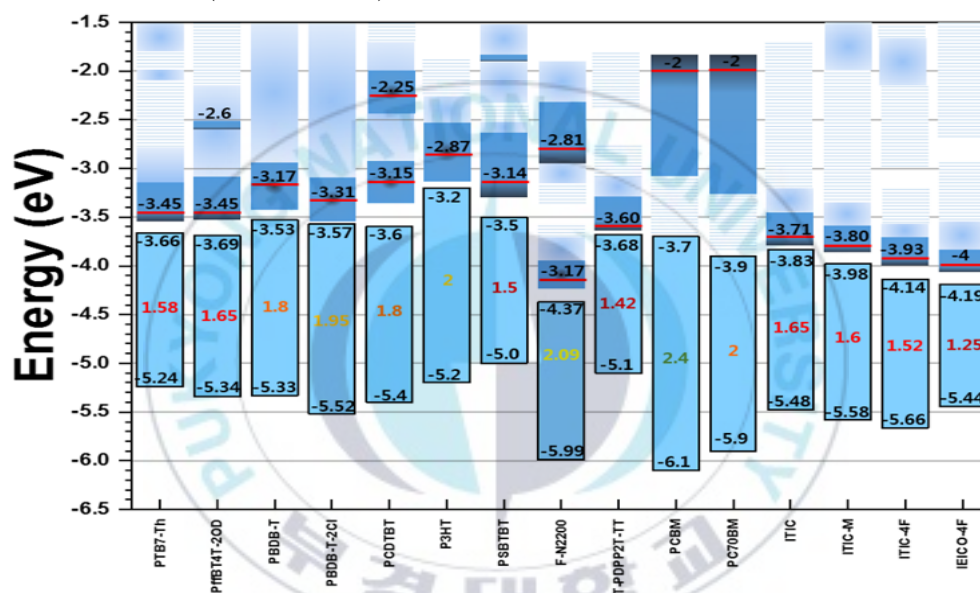


Figure 21. Energy level diagram with population of OD for various organic materials Bright blue squares are band gaps / Dark blue area, light blue area, light blue line shows normalized optical density 0.6~1, 0.3~0.6 and 0.1~0.3 respectively.

From these population of OD properties, the candidates of the organic materials can be divided; the series of fullerene which covers over all OD of donors, the series of ITIC which is overlapped with the only main peaks of donor materials and IEICO-4F which has less overlapped area because of the deepest energy levels of a main peak (-4 eV). By using the selected materials, the MF of the each blend systems (PTB7-Th:PC71BM, PTB7-Th:ITIC and PTB7-Th:IEICO-4F) are calculated (see **Figure 22**).

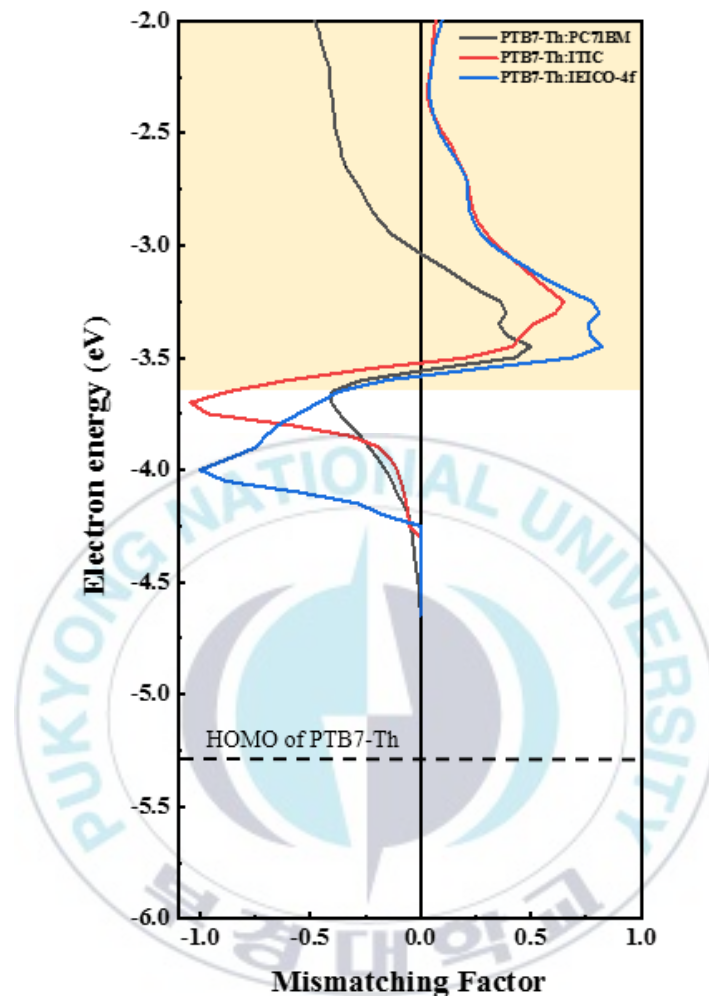


Figure 22. MF of the each blend systems (PTB7-Th:PC71BM, PTB7-Th:ITIC and PTB7-Th:IEICO-4F)

The shapes of each MF show symmetry forms with HOMO level of PTB7-Th (-3.66 eV) as an axis of symmetry. From the definition of MF, symmetry breaking means that MOD of the donor and acceptor are overlapped at the perspective of energy level, hence the intensity MOD is controlled from the weight ratio of donor and acceptor as the normalization form. Since the highest populated MODO peaks of NFA are located near band edge in case of NFA, the symmetry breaking reduce the MF at the section

from -3.66 to -3.0 eV comparing with the peak under HOMO level (from -4.25 to -3.66 eV). Among the blend systems, MF of PTB7-Th:IEICO-4F blends are further from the '0' line, and the highest symmetry is observed between -3.45 eV and -4.0 eV. The highest MF at -3.45 eV has the value of 0.82 which is reduced compared with MF peak at -4.0 eV by MODO.

The results based on the absorption spectra and the energy spectra of the each materials which are presented at **Figure 23** and **Figure 24** imply that the OD of each PTB7-Th and IEICO-4F are separated (i.e. mismatched hot-state formation). And because of high symmetry, MODO which is calculated by inverse of integrated MF should be low. From our expectation, this MF have disadvantage for the directly generated mobile carriers. Comparing with PTB7-Th:IEICO-4F blends, PTB7-Th:ITIC blend shows more reduced MF at -3.25 eV (nearly 0.65) by the symmetry breaking. This MF shape implies that MOD of each materials are well-overlapped (i.e. high MODO) as shown from energy level. This formation may have advantage to the directly generated mobile carriers. Otherwise, as shown in **Figure 22**, the MF of PTB7-Th:PC71BM blend is quite different comparing with NFA. PTB7-Th:PC71BM data shows much low MF (under 0.5) near the HOMO level (-3.66 eV) of donor and distant MF from '0' line in the section from -3.0 eV to -2.0 eV, hence the highest populated MOD peak of PC71BM is far away from band edge. Because of the negative MF sections from -3.0 eV to -2.0 eV the absolute integration should be applied when MF is calculated. The absolute integration section is represented as the yellow box of **Figure 22**.

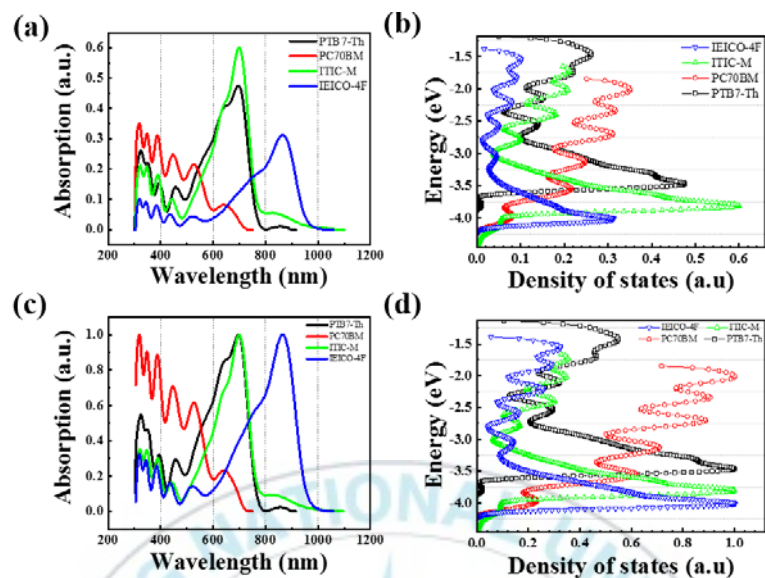


Figure 23. Optical and energetic properties of components for PTB7-Th based two organic materials system. (a) Absorption spectra without normalization. (b) Energy spectra without normalization. (c) Absorption spectra with normalization. (d) Energy spectra with normalization.

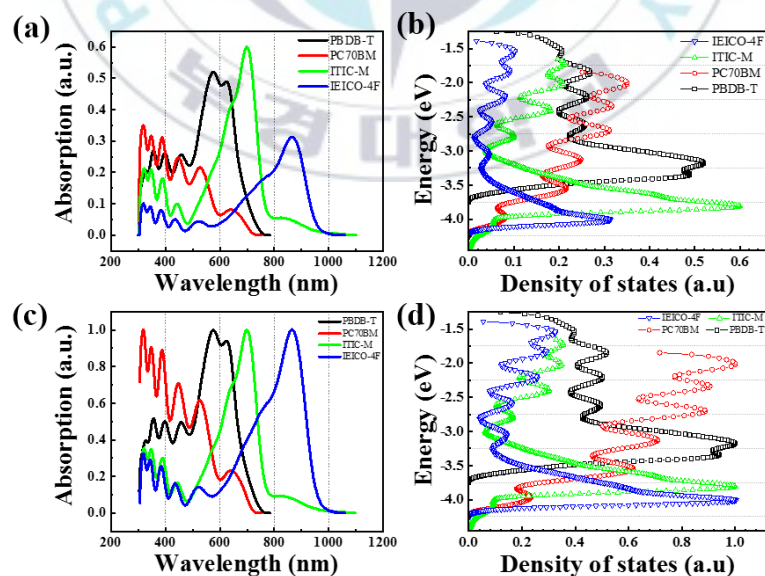


Figure 24. Optical and energetic properties of components for PBDB-T based two organic materials system. (a) Absorption spectra without normalization. (b) Energy spectra without normalization. (c) Absorption spectra with normalization. (d) Energy spectra with normalization.

In order to demonstrate the correlation between MF and PICT, we measured the transient absorption spectra (TAS) of P1:PC71BM blend film as shown in **Figure 25**. As mentioned in **Section 1.2**, because PIA around band edge indicates the information about the CT states where the non-radiative recombination usually occur, the TAS is suitable to show the correlation between MF and PICT. Wavelength of irradiated photon are selected as 400, 550 and 600 nm which are the exciting energy for electrons to area I, area II and area III, respectively. Because the intensity of ΔOD means the amount of generated CT states with the influence of CT states for PICT, the difference of ΔOD for each excitation is one of the most important result to demonstrate the correlation between MF and PICT. As shown in **Figure 25(a)**, the CT states are observed in the range from 600 nm to 650 nm. The results show that the generation of CT states are relatively significant at the mismatched states where the MF are high as 400, 600 nm comparing with well- matched states as 550 nm. The generation of CT states of 550 nm shows around half of the case for 400 and 600 nm. The results means that there are less generation of CT states to the electrons excited on area II.

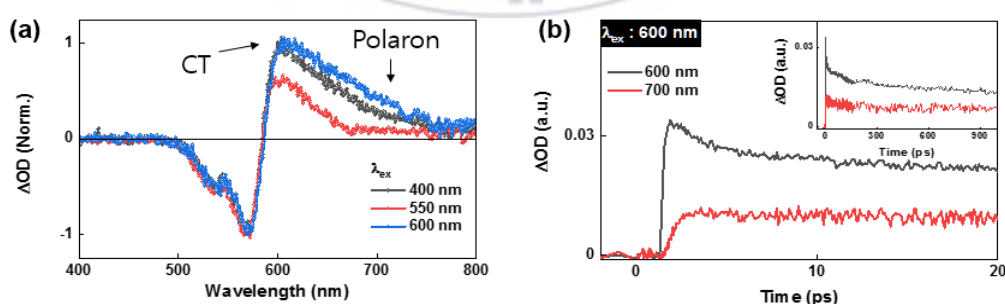


Figure 25. Electron dynamic in the blend system. (a) Transient absorption spectra of excited electron in each area. (b) Life time of polaron state and co-existed state.

The saturated ΔOD on the long wavelength around over 750 nm is PIA of polaron, because the life time of the saturated ΔOD is more than 10 ps as shown in **Figure 25(b)**.

Otherwise, the co-existed state of CT states and polaron is the continuously decrease part of ΔOD . In mismatched cases, the co-existed state covers relatively larger range from 650 to 750 nm. However, the co-existed state of 550 nm excitation just cover around 650 nm. The result means that the area II is much better condition to generate polaron with less influence of CT states. In consequently, we can observed that the electron excitation on well-matched states enhance the rate of efficient PICT by using TAS.

4.3 Conclusion

We developed an effective method to quantify the degree of hot-state matching between the donor and acceptor in the blend system. By calculating the MF of BHJ thin film from the MODO between the donor and acceptor, we quantify the degree of energy-state mismatching between the electron donor and acceptor at their interface. A smaller MF value indicates a higher degree of energy-level matching, whereas a larger MF value indicates a lower degree of state overlapping at the BHJ interface. In order to demonstrate the effect of hot-state matching via calculation of MF, we measured TAS for targeting electrons which excited on corresponded hot-state energy levels. From the TAS result, we can observe the relation between MF and the generation rate of CT states in the blend system. The energy level with low MF which is well-matched energy level has the relatively low generation rate of CT states, while the energy level with the higher MF has huge CT states. The result means that the hot-state matching between donor and acceptor is strongly related with the PICT in the organic blend system.

CHAPTER 5

APPLYING EFFICIENT CHARGE TRANSPORT ON ORGANIC SOLAR CELL

5.1 Introduction

The open-circuit voltage (V_{oc}) in organic photovoltaics (OPVs) based on bulk heterojunction (BHJ) of electron-donating conjugated polymers and electron-accepting materials is one of the important parameters for determining the power-conversion efficiency (PCE).^{32,98,141} Historically, although the V_{oc} is originated on the energy gap between the both quasi-Fermi levels of donor and acceptor materials, numerous researcher regards the trend of practical V_{oc} values would proportional to the maximum of V_{oc} which can be calculated from $HOMO_{donor}-LUMO_{acceptor}$.^{142,143} This empirical result is the simple and intuitional approach. However, sometimes the relative HOMO-LUMO energy gap corresponding to V_{oc} is not always the case under practical conditions, since sometimes the energy transfer mechanism became more significant than the HOMO-LUMO value. Although researchers have attempted to increase V_{oc} through various reasonable approaches, including the use of electron donors with deeper highest occupied molecular orbital (HOMO) levels and electron acceptors with shallower lowest unoccupied molecular orbital (LUMO) level and inserting a functional layer between the active layer and electrodes, OPVs exhibit relatively low V_{oc} values, as compared with inorganic semiconductors and perovskite-based photovoltaics.^{47,104,144,145}

The relatively low V_{oc} in OPVs is mainly ascribed to the high voltage loss resulting from the significant photon energy loss at the lowest-lying charge transfer (CT) states located at levels deeper than the LUMO of the electron acceptor.^{68,104,105} Because substantial electrons and holes separated at the interface undergo non-radiative recombination at the lowest-lying CT states, inefficient photoinduced charge transfer (PICT) occurs unexpectedly in the vicinity of the LUMO level of electron acceptor, resulting in loss of V_{oc} .^{32,50,98} It was previously reported by Heeger group that efficient PICT for directly generated mobile carriers without trapping in CT states could be achieved via a hot-state charge transfer process between the electron donors and acceptors. Friend group reported that efficient PICT occurs through hot-state charge delocalization between the donor and acceptor. They also demonstrated that both geometric and energetic accessible delocalized state matching are key factors for suppressing V_{oc} loss. According to these observations, it is expected that hot-state matching between the electron donor and acceptor is a critical factor for achieving efficient PICT and that ensuring well-matched hot states between the electron donor and acceptor is essential for achieving a high V_{oc} . These facts have motivated research toward gaining an understanding of the hot-state matching between the electron donor and acceptor. Although simulations and experimental studies have been performed to investigate the hot-state matching between the electron donor and acceptor for efficient PICT. Systematic studies on the correlation between the hot-state matching and V_{oc} loss in actual devices have not been conducted. Moreover, because useful methods to quantify the hot-state matching involving not only the LUMO level but also a broad range of electron energy levels between the electron donor and acceptor materials have

not been developed, applying hot-state matching to increase the V_{oc} in actual devices remains a challenge.

Thus, in this study, we investigated correlation between the V_{oc} loss and hot-state matching in OPVs and developed an effective method to quantify the degree of hot-state matching by calculated MF between the donor and acceptor. It was found that a larger MF causes a larger V_{oc} loss for binary and ternary OPVs. By using this novel approach, we demonstrate that the well-matched optical DOS of donor and acceptor configuration exhibits higher V_{oc} (0.03 ~ 0.13 V) than the mismatched states. Donor materials are selected as P(BD TT-ttDPPDtt) (P1) and P(BD TT-BTBDPPD) (P2), equivalent LUMO level with the different DOS of the full-range, to show the hot-state matching dependent V_{oc} . And by using various organic materials such as PTB7-Th, series of PBDB-T, IEICO-4F, series of PCBM and ITIC, the tendency of the correlation also observed. Interestingly we found that the fullerene based acceptors and the non-fullerene acceptor (NFA) blends exhibit a different tendency for hot-state matching under 1 sun spectrum (100mW/cm²). However, under low light intensity (10mW/cm²), V_{oc} dependency by hot-state matching for NFA blends also be observed clearly. Finally, we apply the hot-state matching to ternary solar cells which exhibit the highest V_{oc} with well-matched states. By changing the donor/acceptor ratio, we are able to control the integrated MF of the three organic systems which occur the higher V_{oc} . The improvement of V_{oc} is nearly 3~9% which has dependency with the type of organic materials. Finally, we achieved a high-efficiency ternary OPV device with a PCE of 16.15% by controlling the MF between the donor and acceptor.

5.2 Result and Discussion

5.2.1 Mismatching Factor from Modified Optical Density

< Correlation between MF and V_{oc} >

Based on quantification of hot-state matching, correlation between MF and V_{oc} on actual device is investigated, the correlation was studied at both the comprehensive ODO dependent V_{oc} by using the integrated M.F and the each state matching formation dependent V_{oc} .

In order to obtain the quantitative results of the correlation between hot-state matching and V_{oc} , we also apply the 'MF' which is defined at previous section. **Figure 26(a)** shows the MF of both P1:PC71BM and P2:PC71BM blend systems as energy levels. A black horizontal line represents that the MF is '0' which have the perfectly same optical intensity of donor and acceptor. In order to visualize the hot-state matching formation, three kinds of formations are represented by colored zones. The red, blue and green boxes indicate the Area I, II and III respectively, and the empty box is the electron forbidden zone of the donor. Therefore, although the MF approach to the '0' point near the energy level -4.5 eV, this area is meaningless for our research concept. From the MF, we can select the candidate of the wavelength. As shown in **Figure 26(a)**, we irradiate 450, 488, 500, and 587 nm light to P1:PC71BM blends. The irradiated photons should excite the electrons on the donor domains, and these excited electrons are located at the particular energy levels. Each black quadrangle at **Figure 26(a)** indicates the absolute energy levels where excited electrons are located by absorption of the 450, 488, and 587 nm light respectively. The 488 nm photons excite the electrons

to the most well matched level states (-2.75 eV and -2.93 eV respectively) where the Hot-state matching formation is Area II. Otherwise, in case of 450 nm irradiation, the excited electrons of donor domains are excited to -2.66 eV which is Area I as shown in **Figure 26(a)**. The last formations of Area III is 587 nm as -3.3 eV.

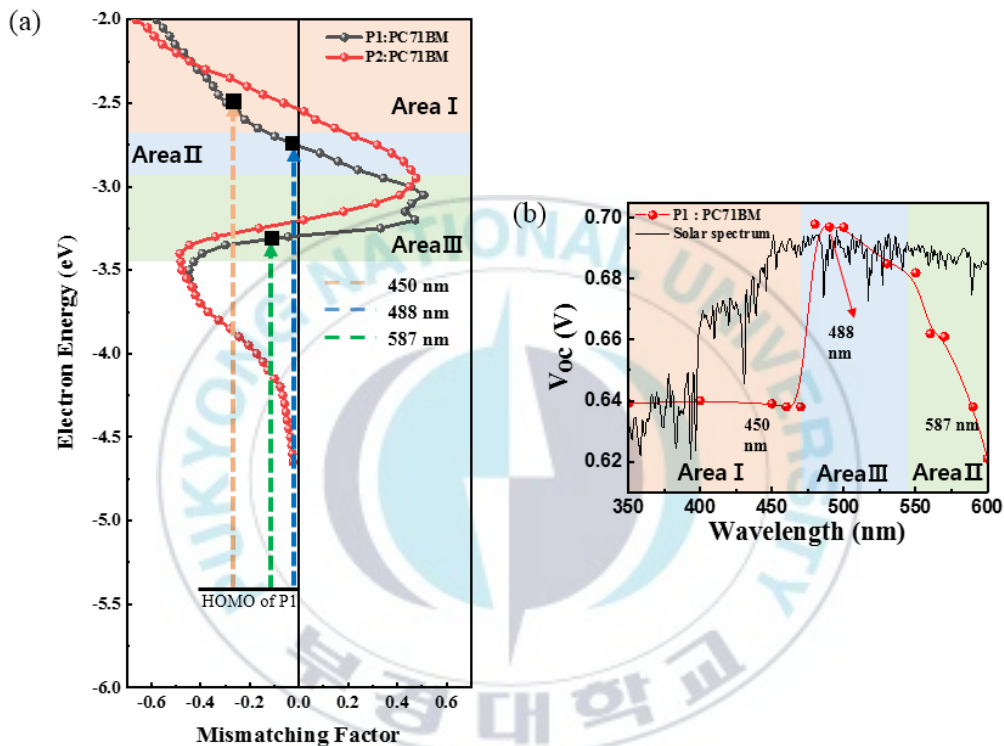


Figure 26. Variation of V_{oc} under irradiation of different monochromatic light for **P1:PC71BM**. (a) Mismatching factors for P1:PC71BM and P2:PC71BM blend system. (b) Wavelength dependent V_{oc} for P1:PC71BM.

Because areas I, II, and III have different degrees of MODO between P1 and PC71BM, the use of monochromatic light with different wavelengths (different photon energies) can selectively excite electrons to each state of the areas. Therefore, by measuring the V_{oc} variation for incident monochromatic light with different energy levels, the correlation between the MODO and V_{oc} in the OPV device can be

investigated. **Figure 26(b)** shows the variation in V_{oc} for the OPV device under irradiation with different monochromatic light. The OPV device structure is shown in the inset of **Figure 26(b)**.

Interestingly, the device exhibits noticeable differences in the V_{oc} value for irradiation with monochromatic light under different energy levels. When monochromatic light with wavelengths of <480 nm is applied to the device, the electrons are selectively excited to area I by absorbing the incident energy. Under irradiation with wavelengths of 400, 450, 460, and 470 nm, the device exhibits a nearly constant V_{oc} of ~ 0.64 V. However, the V_{oc} suddenly increases from 0.64 to 0.72 V when monochromatic light with a wavelength of 480 nm is applied to the device. The enhanced V_{oc} is maintained under irradiation with wavelengths of 490, 500, 520, and 530 nm, and the V_{oc} decreases again when the wavelength of the incident light exceeds 550 nm. Because irradiation with wavelengths of 480–530 nm can excite electrons to area II and irradiation with wavelengths of >550 nm can excite electrons to area III, it is concluded that excitation of electrons to area II increases the V_{oc} of the device.

The result is well matched with our expectation that the hot-state matching of Area II have advantage to directly generated mobile electrons because of the well-matched hot-state, and V_{oc} of the highest value is 0.7 V at 488 nm. And in case of P1:PC71BM blend, the gap of V_{oc} between well-matched states and poor-matched states is nearly 0.06 V. Moreover, from **Figure 26(b)**, the two organic materials system seems to have a capacity for generate mobile carriers at each energy levels, and this capacity of carrier generation is determined by both the state matching and the light intensity. In order to demonstrate the capacity to generate mobile carriers at each energy levels, we measured

the saturated V_{oc} under the separated light with various light intensity. **Figure 27** shows the saturated V_{oc} at a particular wavelength with light intensity. Electrons at HOMO levels are excited by the absorption of the light energy which have particular wavelengths (355/488/633 nm), then excited electrons are located in the Area I, Area II and LUMO level (Area III) respectively.

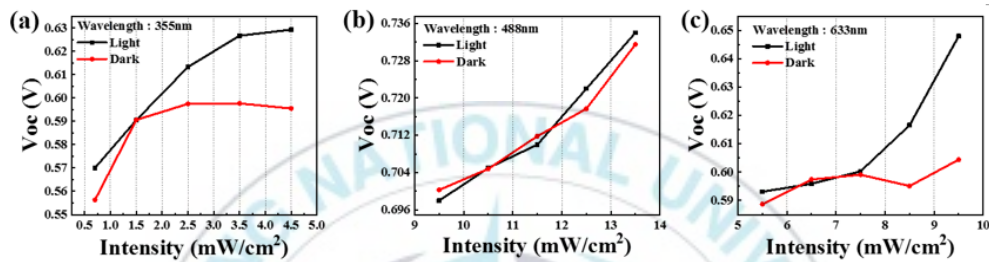


Figure 27. Saturated V_{oc} under the condition of particular wavelengths. (a) 355 nm. (b) 488 nm. (c) 633 nm.

As we expected, the saturated V_{oc} also has dependence on the MF. At the Area II where the MF is -0.016, the highest non-saturated V_{oc} (0.736 eV) is observed as the light intensity is increased to $13.5 mW/cm^2$. This results indicates that the capacity to generate mobile carriers is higher than AM 1.5 G condition (i.e. this blend system can generate more mobile carriers under the higher light intensity than AM 1.5 G). The interesting results are observed at both Area I and Area III. The saturated V_{oc} (nearly 0.60 V) are observed at both the Area I and Area III which have low MF as -0.166 and -0.043 respectively. These results demonstrate that, at the poor matched states, the extra photons are out of roles to generate free charge carrier, which means that the capacity of carrier generation are rely on MF. But when we irradiate the particular wavelength under light conditions which is white light with weak intensity, the differences between Area I and III are observed. Both V_{oc} values are shown as black lines comparing with

dark condition (red line), the value of saturated V_{oc} are different. The saturated V_{oc} of Area I boost to 0.63 V, whereas the non-saturated V_{oc} is observed at Area II and Area III. We assume that in case of Area III the ratio of non-radiative recombination is reduced by enhanced number of carriers, hence the white light may covers the influences of CT states. Consequently, we demonstrated that the well-matched state has the higher ΔV_{oc} (0.03~0.13 V) than mismatched states, hence correlation between MF and these results demonstrate that V_{oc} is involved in the directly generated mobile carriers in two organic systems. Moreover, we observed that low MF also has more capacity for the directly generated mobile carriers from the saturated V_{oc} . Thus, the MF for the full range of unoccupied molecular orbitals is associated with the directly generated mobile carriers, and one of the most crucial aspect of designing two organic materials system should be the MF to achieve the efficient directly generated mobile carriers under equilibrium states.

This tendency is also observed in the variation of V_{oc} with an increase in the intensity of monochromatic light, as shown in **Figure 28**. We selected three monochromatic lights of 450, 488, and 587 nm, corresponding to the energy for exciting electrons to areas I, II, and III, respectively, and monitored the evolution of V_{oc} with an increase in the light intensity. As shown in **Figure 28**, V_{oc} of 450 and 587 nm increased slightly with the increase in the light intensity and becomes saturated approximately 0.6 V. However, V_{oc} under irradiation with monochromatic light of 488 nm differ significantly. The V_{oc} of 488 nm continuously increase with the increase of light intensity from 0.6 to 14.5 mA/cm², and there are no saturated V_{oc} under irradiation condition. Moreover, even the irradiated light intensity is equal, a considerably higher

V_{oc} is obtained under light irradiation of 488 nm. Because irradiation with monochromatic light of 488 nm excites electrons to area II with a well-matched energy state, these results clearly indicate that the energy-level matching at the interface between the electron donor and acceptor is the critical factor for achieving a high V_{oc} .

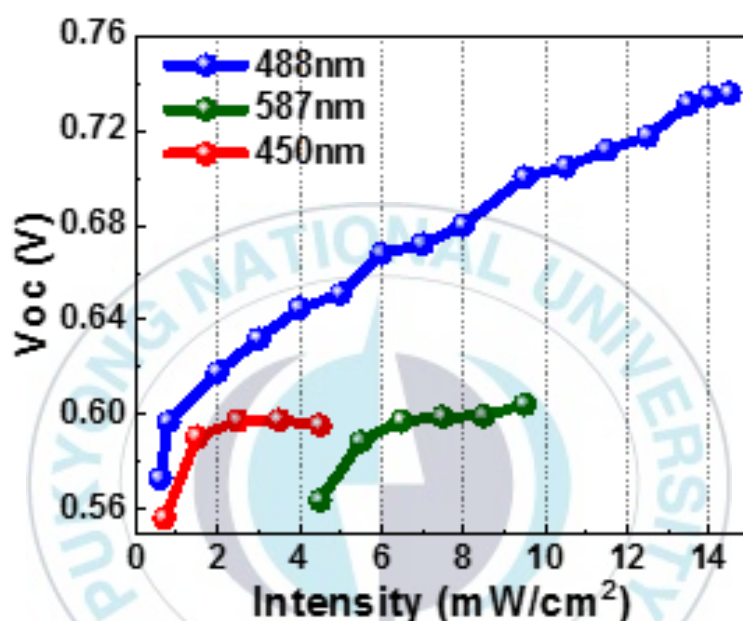


Figure 28. Light intensity dependent V_{oc} at each state matching formations.

In order to confirm our hypothesis that the number of directly generated mobile carriers are influenced by MF, we measured the wavelength dependent V_{oc} under AM 1.5 G. **Figure 29(a)** and **29(b)** shows the light intensity and wavelength dependent V_{oc} . At the PTB7-Th:PC71BM blend, the highest V_{oc} also be observed on Area II, hence mobile carriers by ultra-fast charge transfer are directly generated under the well-matched hot-state matching formation. And the lowest V_{oc} is observed at Area I, and the gap of V_{oc} between well matched and mismatched cases is nearly 0.9 V. The wavelength dependent V_{oc} of PTB7-Th:PC71BM also show the less correlation with light intensity, which indicates that V_{oc} is influenced by MF even light intensity.

However, the strong correlation with both MF and light intensity at PTB7-Th:ITIC blend are observed at the as **Figure 29(a)**, hence the location of DOS matching formation is reversed comparing with PTB7-Th:PC71BM blend. Here, we assume that the difference of the optical density shape between PC71BM and NFA is a key factor. And it is hard to distinguish, a major factor that determine the V_{oc} . In order to demonstrate a major factor to determine V_{oc} in NFA, energy level dependent V_{oc} under the low intensity of light are measured as **Figure 29(c)** and **29(d)**. The low intensity of light is irradiated by using optical filter (10 % of AM 1.5 G). Each green and yellow area implies MOD of PTB7-Th and PC71BM respectively, and red square point is V_{oc} at particular energy levels.

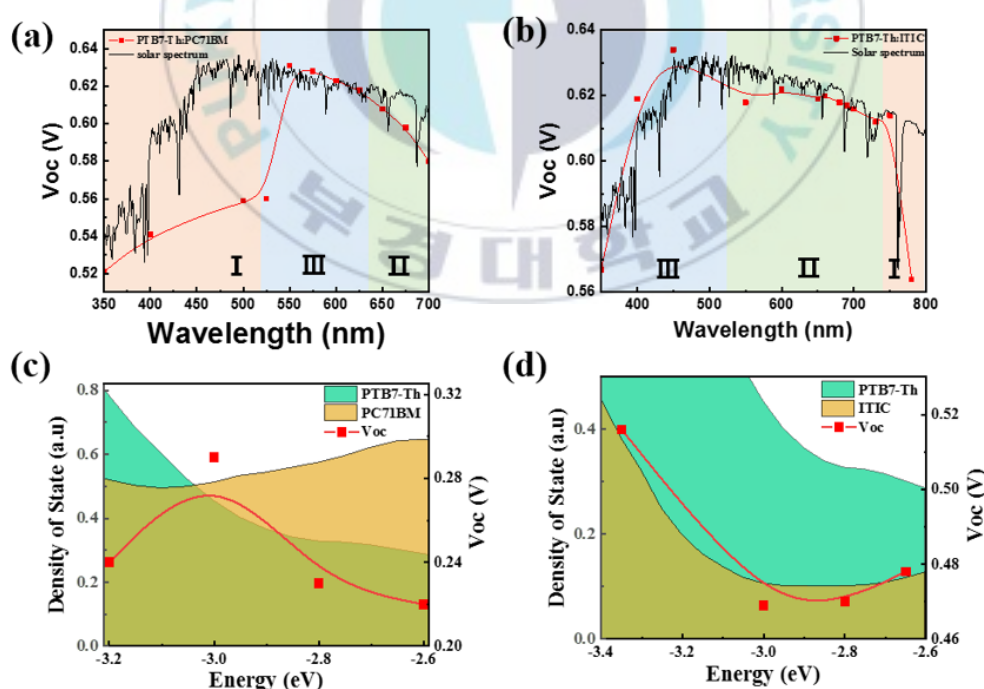


Figure 29. Wavelength dependent V_{oc} of binary blend system. (a) PTB7-Th:PC71BM. (b) PTB7-Th:ITIC. (c) Correlation between MOD and V_{oc} for PTB7-Th:PC71BM (d) Correlation between MOD and V_{oc} for PTB7-Th:ITIC

As shown in **Figure 29(c)** and **29(d)**, V_{oc} has only correlate with overlapping line but not each MOD of donor and acceptor. The important point is that the light intensity to excite the electrons on both -3.4 (600 nm) and -2.6 eV (450 nm) is nearly equal but MF is different. The gap of V_{oc} is nearly 0.04 V at these energy levels. This result demonstrate that the major factor to determine V_{oc} should be MF as we expected. Otherwise, the value of V_{oc} for ITIC blend (0.46 ~ 0.52 V) is higher than PC71BM blend (0.20 ~ 0.29 V). We assume that these variable V_{oc} as material types may be related with other factors as carrier mobility or morphology. Furthermore, we also investigate the scale of V_{oc} variation from MF. From our previous results, the variation of V_{oc} is measured as the scale as 0.03 ~ 0.1 V. If MF and PICT have meaningful relation, the variation of both V_{oc} and quasi-Fermi levels also should be related as similar scale, because quasi-Fermi levels are determined by PICT. Therefore, the variation of quasi-Fermi levels under the various light intensity should be similar with the variation of V_{oc} by MF.

Figure 30(a) and **30(b)** shows the light intensity dependent variation of quasi-Fermi levels. The light intensities are selected as dark, low, middle and high, which are 0 %, 30 %, 60 % and 100 % intensity of AM 1.5 G. And ΔE indicates the variation of quasi-Fermi level by irradiation. And quasi-Fermi levels of both two acceptor materials are measured by using bilayer devices. The variation of quasi-Fermi levels are observed at the range 0.03 ~ 0.13 V, and this range is equal to our previous results. The differences between PC71BM and ITIC are the value of ΔE and time to reach stable states. We assume that both differences may be concerning with carrier mobility of each materials. The results also be observed at KPFM data as **Figure 30(d)**. These

results are crucial evidence to demonstrate that the origin of V_{oc} variation by DOS matching are related with PICT. Consequently, our results demonstrate that MF is a major factor to determine V_{oc} , and correlation between MF and V_{oc} is regardless of material type. However, the variation in range for V_{oc} can be different for each material type due to other factors as carrier mobility. Moreover we found that the maximized improvement of V_{oc} by MF are nearly 0.1 V, this means that the improvement of V_{oc} as 3~9 % can be achieved from MF.

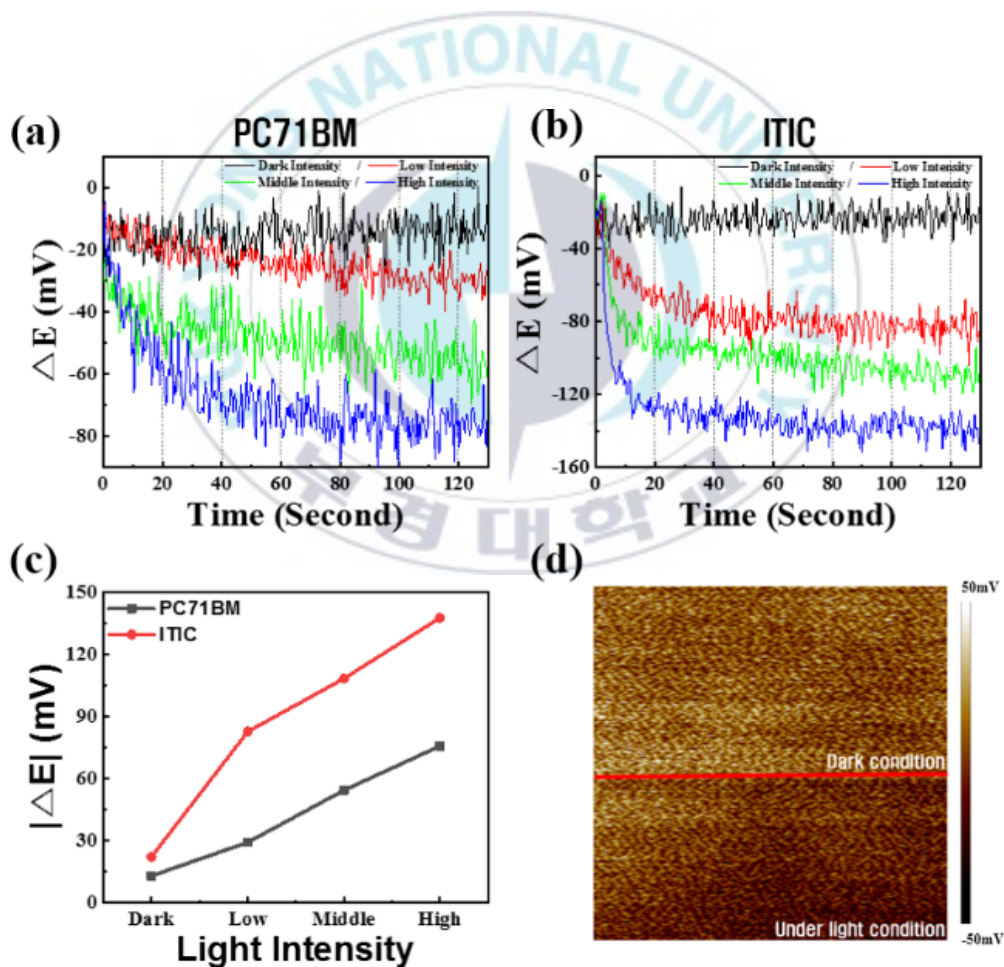


Figure 30. Variation of quasi-Fermi levels under light irradiation. (a) PC71BM. (b) ITIC. (c) light intensity dependent variation of quasi-Fermi levels at stable state. (d) KPFM.

<Estimation of V_{oc} loss in binary and ternary OPVs using integration of MF>

Because the V_{oc} of OPVs is highly sensitive to the MF value indicating the degree of energy-level matching between the electron donor and acceptor at each energy state, the MF can be calculated to estimate the V_{oc} loss at the interface during PICT. A smaller MF value indicates a higher degree of energy-level matching, along with a higher V_{oc} and smaller V_{oc} loss, whereas a larger MF value corresponds to a larger V_{oc} loss, as described before. However, because a donor material in an actual OPV device is excited by irradiation of AM 1.5 solar light with a wide spectral range, the electrons in the donor can be excited to areas I, II, and III simultaneously by absorbing solar light with a wide spectral range and then be transferred to the acceptor via PICT. Therefore, the MF indicating the degree of energy matching at a specific energy state is insufficient for estimating the energy loss in an actual device under the irradiation condition of AM 1.5 solar light.

Integrating each MF value for each energy state over the entire range of the MOD for the donor would be more useful in the case of an actual OPV device irradiated by solar light. As integration of the MF over the entire range of the MOD for the donor indicates the degree of MOD under solar light irradiation, it is more meaningful than each MF at a specific energy state. **Fig. 31(a)** shows the correlation between V_{oc} and the integrated MF for P1:PC71BM and P2:PC71BM. The molecular structure and energy level of P2 are shown in the inset of **Fig. 31(a)**. Because P1 and P2 have similar properties, with similar optical bandgaps (P1 = 2.04 eV, P2 = 2.08 eV) and HOMO levels (P1 = -5.41 eV, P2 = -5.44 eV) but different MOD shapes and MF values, a comparative analysis of these materials provides information for investigating the

validity of the integration of the MF. The integrated MF values are 0.452 for P1:PC71BM and 0.440 for P2:PC71BM. As expected, P1:PC71BM exhibits a higher V_{oc} than P2:PC71BM. This result is reproduced for the devices of PTB7-Th:PC71BM, PTB7-Th:ITIC, and PTB7-Th:IEICO-4F, which are widely used as active materials for OPVs. **Fig. 31(b)** shows the V_{oc} variations for the integrated MF values of these materials. All the device structures and fabrication processes are identical, except for the active materials. The integrated MF values of PTB7-Th:PC71BM, PTB7-Th:ITIC, and PTB7-Th:IEICO-4F are 0.36, 0.39, and 0.45, respectively, and the resulting V_{oc} values are 0.81, 0.78, and 0.71 V, respectively. These results indicate that integrating the MF value across the entire MOD range of the donor is a reasonable approach for estimating the V_{oc} loss in OPVs.

As we expected, the results of V_{oc} has a strong dependency with MF. And the MF of each blend systems for PTB7-Th:PC71BM, PTB7-Th:ITIC and PTB7-Th:IEICO-4F are 0.36, 0.39, and 0.45, while V_{oc} are 0.79, 0.81 and 0.71 V respectively. Since the symmetry breaking is within the axis of HOMO level, the highest V_{oc} is observed at PTB7-Th:ITIC blend. On the other hand, the lowest V_{oc} is observed for PTB7-Th:IEICO-4F blend which has the highest MF with 0.45. The gap of V_{oc} is observed as 0.1 eV by the difference of MF. Although the MF of PTB7-Th:PC71BM at the section from -3.0 to -2.0 eV may seem to have disadvantage for hot-state matching, the excluded energy level (over than -2.0 eV) because of the glass absorption determines the higher MF value compared to the case of PTB7-Th:IEICO-4F blend. Consequently, **Figure 31(a)** and **31(b)** clearly demonstrated the correlation between MF and V_{oc} as we expected. Moreover, PBDB-T based two organic material systems was also be

investigated in **Figure 32(a)** and **32(b)**. As shown in these results, MF dependent V_{oc} is observed from various blend systems regardless of material types. And we assume that the correlation between MF and V_{oc} is due to the number of directly generated mobile carriers.

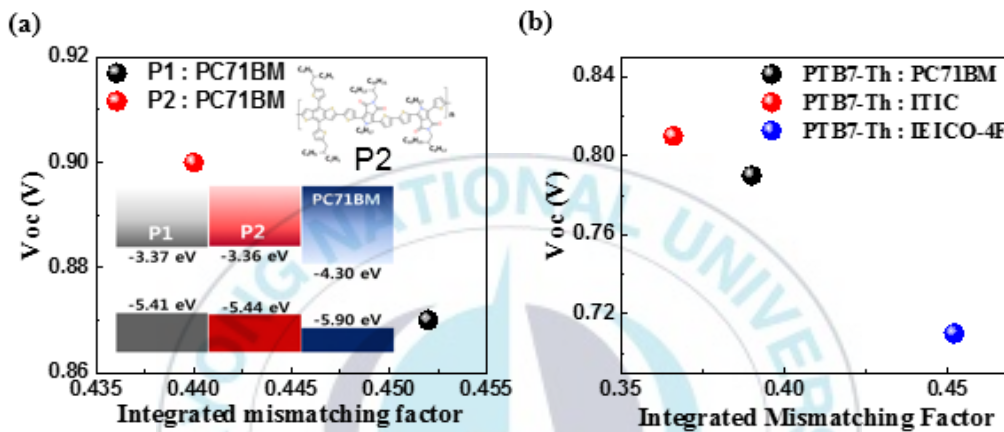


Figure 31. Photovoltaic properties for applying MODO to organic based solar cell. (a) Integrated mismatching factor dependent V_{oc} of P1:PC71BM and P2:PC71BM. **(b)** Integrated mismatching factor dependent V_{oc} of PTB7-Th based photovoltaics.

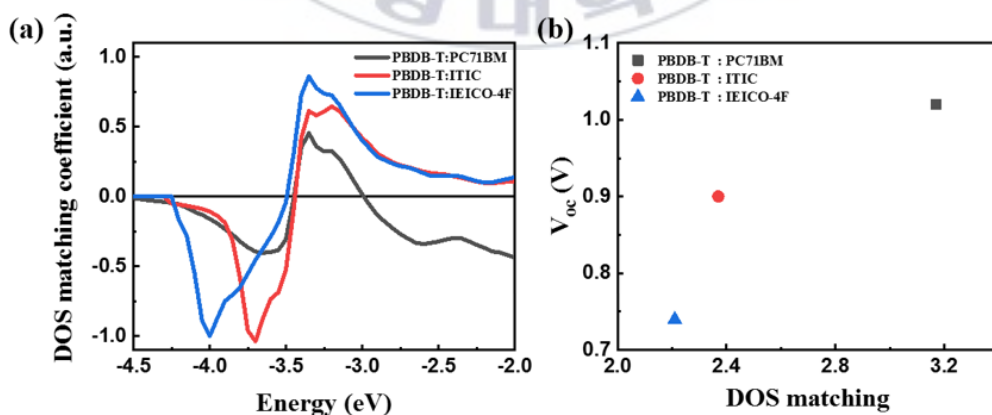


Figure 32. MF of PBDB-T based blend systems. (a) Mismatching factors at the absolute energy levels. **(b)** V_{oc} dependency with MF.

To confirm this concept of integrating the MF for an actual device, we fabricated a ternary OPV device with three active materials. As the absorbance of the active materials could be changed by altering the ratio of the mixture in the ternary system, we could intentionally control the MF value by controlling the mixture ratio of the three materials. In case of one donor with two acceptor should be shown as below.

$$MF_{DAA} \equiv D_{Donor}(\varepsilon)_i - D_{Acceptor1}(\varepsilon)_i - D_{Acceptor2}(\varepsilon)_i \text{-----Equation 6.}$$

$$MF_{DDA} \equiv D_{Donor1}(\varepsilon)_i + D_{Donor2}(\varepsilon)_i - D_{Acceptor}(\varepsilon)_i \text{-----Equation 7.}$$

Where the MF_{DDA} is mismatching factor of double donors system, while MF_{DAA} is double acceptors system.

For the ternary OPV device, D18 was selected as the donor material, and Y6 and PCBM were selected as acceptors. **Figure 33** shows the device structure, along with the molecular structures of D18, Y6, and PCBM, and the device is ITO/PEDOT:PSS/D18:Y6:PCBM /Al.

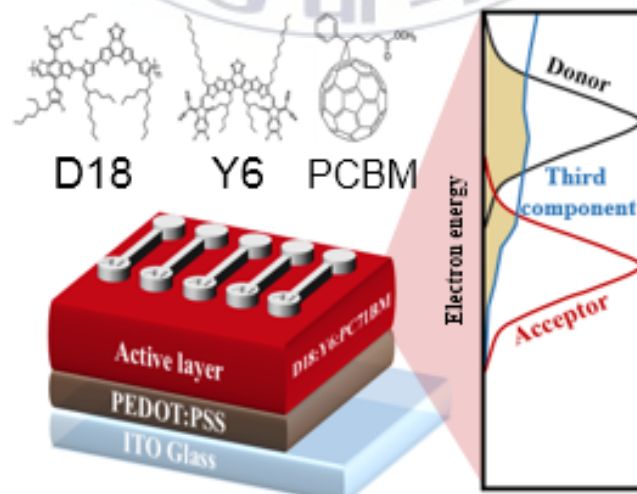


Figure 33. Device and molecular structure of D18, Y6 and PCBM with role of third component.

The inset of **Figure 33** shows the concept of third component on ternary OPVs. The third component is selected as PCBM. Intention for adding PCBM are that the optical density of third component covers optical density of separated donor and acceptor. Since low absorption coefficient of PCBM than PC71BM can concentrate absorption to donor materials, PCBM is suitable for control of MODO for D18:Y6 blend system.

Although the MOD of D18 is considerably separated from that of Y6, the MOD of PCBM covers the ranges of those of D18 and Y6 (see **Figure 34(a)**). Therefore, controlling the amount of PCBM was expected to enable control over the MF for the ternary system. **Figure 34(b)** shows the MF at each electron energy level of D18:Y6:PCBM. The mass ratio of D18:Y6:PCBM was 1:1.6:x (where x represents the amount of PCBM and was set as 0, 0.2, 0.4, and 0.6). The yellow box indicates the absorption area of the D18 donor, which was the integrated section for the integrated MF. As shown in **Figure 34(b)**, the MF of the ternary system was changed by altering the amount of PCBM. The arrows around 2.5 eV indicate the MF variation caused by adding PCBM. The ternary system with $x = 0.4$ exhibited an MF value of zero at 2.5 eV, indicating a high degree of MODO between the D18 donor and Y6 and PCBM acceptors at 2.5 eV. The integrated MFs of the ternary system with PCBM component ratios of $x = 0.6, 0.4, 0.2,$ and 0 were calculated as 0.232, 0.252, 0.275, and 0.299, respectively.

Figure 35(a) presents the variation in V_{oc} for different values of the integrated MF. As expected, larger values of the integrated MF corresponded to lower V_{oc} values. The highest V_{oc} was observed at $x = 0.6$, corresponding to the smallest integrated MF of

0.232. **Figure 35(b)** shows the current–voltage (J - V) curves of ternary devices with different mixture ratios. The OPV devices exhibited high performance with regard to the short-circuit current density (J_{sc}), V_{oc} , and fill factor (FF). J_{sc} and V_{oc} were altered by changing the mixture ratio of the ternary system. The highest PCE of 16.15% was achieved for the device with a D18:Y6:PCBM ratio of 1:1:0.2, whereas the highest V_{oc} was observed for the device with a D18:Y6:PCBM ratio of 1:1:0.6. Because the PCE was determined by the J_{sc} , FF , and V_{oc} , the optimal mixing ratio for maximizing the V_{oc} differed slightly from that for maximizing the PCE, which can be overcome by optimizing the nanoscale morphology of the active layer.

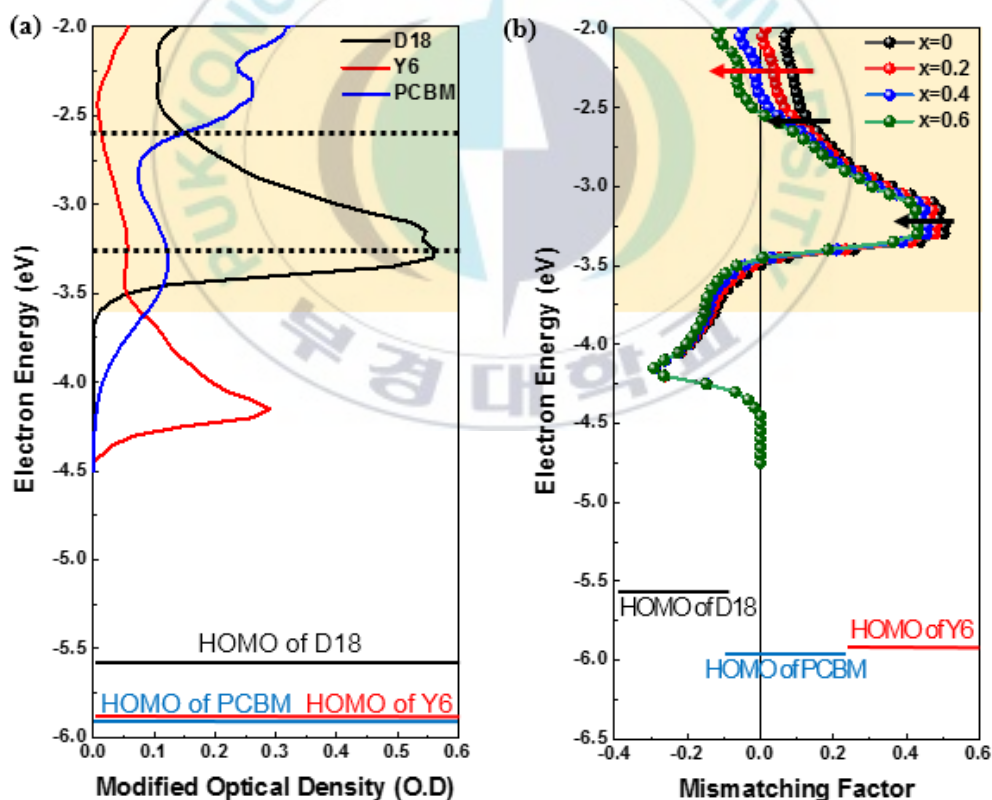


Figure 34. Photovoltaic properties for applying MODO to organic based solar cell. (a) MODO of D18, Y6 and PCBM. **(b)** Mismatching factor at each energy level of D18:Y6:PCBM blend system.

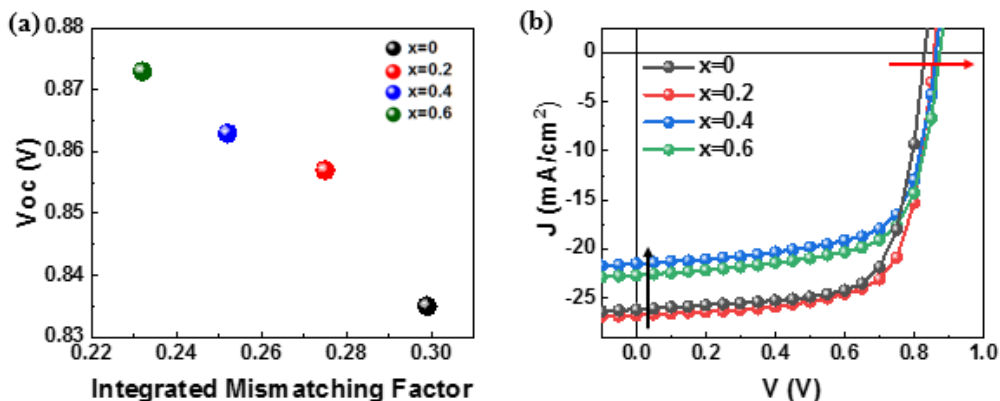


Figure 35. Photovoltaic properties with Integrated Mismatching dependent (a) Integrated mismatching factor dependent V_{oc} with the ratio of third component. (b) J - V characteristics for optimized for the ratio of third component.

To verify the correlation between V_{oc} and MF, we also fabricated ternary OPVs using PBDB-T, ITIC, and PC71BM materials and conducted the same experiments. Since electron transfer layer (ETL) have a pinning effect which reduced the effect of the variable V_{oc} , the ETL is excluded in this structure. In order to apply MF, we measured the complementary absorption with the various ratio as shown **Figure 36**. We measured the complementary absorption and MF of the various ratio.

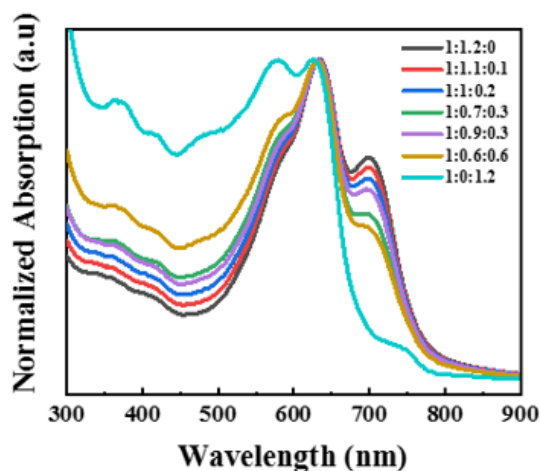


Figure 36. Complementary absorption spectra with the various ratio of PBDB-T:ITIC:PC71BM blend

The MF is calculated without the normalization of MOD intensity. Because in order to confirm the ratio dependent V_{oc} , the MOD intensity of each organic materials is crucial factors. **Figure 37** shows the MF as energy levels. The integration section for MF is also selected from LUMO level of PBDB-T which is a yellow area, and the integrated MF of each blend ratio is calculated in **Table 1**.

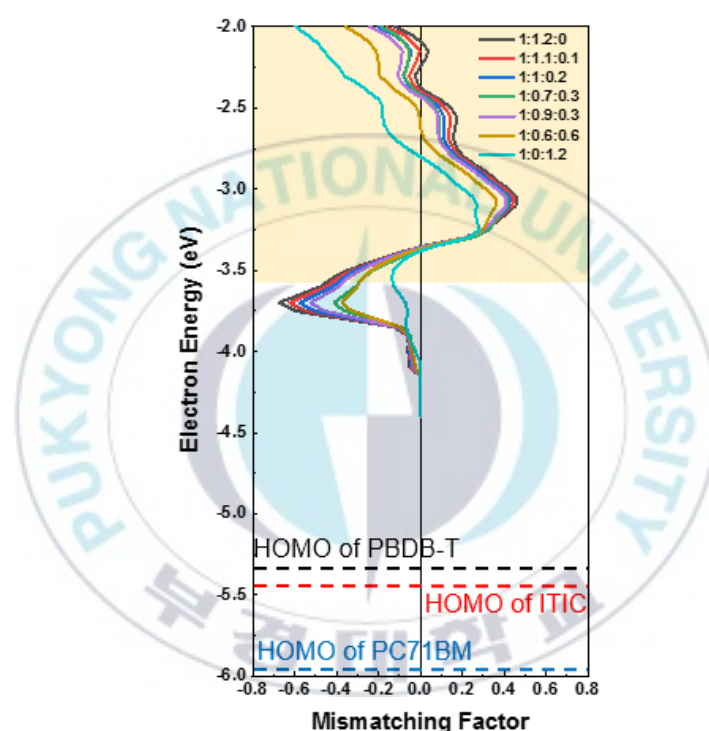


Figure 37. Mismatching factor of PBDB-T:ITIC:PC71BM blend system.

Table 1. Integrated MF of PBDB-T:ITIC:PC71BM blend system.

PBDB-T : ITIC : PC71BM	Integration of MF
1 : 1.2 : 0	0.29215
1 : 1.1 : 0.1	0.28039
1 : 1 : 0.2	0.27611
1 : 0.7 : 0.3	0.25741
1 : 0.9 : 0.3	0.27262
1 : 0.6 : 0.6	0.27055
1 : 0 : 1.2	0.34929

As shown in **Table 1**, the highest integrated MF is calculated at 1:0.7:0.3, but both two organic materials system as 1:1.2:0 and 1:0:1.2 have low integrated MF. Therefore, if the V_{oc} relies on the value of integrated MF, PBDB-T:ITIC:PC71BM blend system may have the ratio dependent variable V_{oc} and the highest V_{oc} would be observed at the ratio 1:0.7:0.3. Although the standard of ratio for donor and acceptor is 1:1.2, the ratio of 1:0.7:0.3 is also included. Because, from our calculation, 1:0.7:0.3 has the lowest MF.

As we expected at **Figure 37** and **Table 1**, two organic materials system shows the low V_{oc} with the higher integrated MF as 0.29 and 0.34. Otherwise, the lowest MF is observed at 1:0.7:0.3 with the value as 0.892. **Figure 38(a)** and **Table 2** show the integrated MF dependent V_{oc} of each blend ratio. The tendency of variable V_{oc} and integrated MF is observed as a linear shape, and the variation of V_{oc} is measured as nearly 0.08 V in ternary blend system. As we expected in **Table 1**, the binary blend system of PBDB-T:PC71BM and PBDB-T ITIC which have higher MF show lower MF comparing with ternary system. Otherwise, the highest V_{oc} is observed in case of 1:0.7:0.3 with the value of 0.89 V.

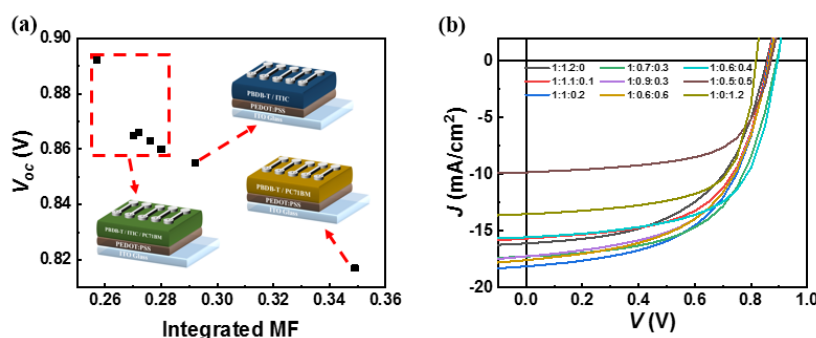


Figure 38. Photovoltaic properties of PBDB-T:ITIC:PC71BM solar cell (a) Integrated mismatching factor dependent V_{oc} of PBDB-T: ITIC: PC71BM based OPVs. (b) J - V characteristics for each material ratio.

Table 2. Photovoltaic parameter with ratio of the PBDB-T:ITIC:PC71BM

Ratio (PBDB-T : ITIC : PC71BM)	Jsc (mA/cm ²)	Voc (V)	FF	PCE (%)
1 : 1.2 : 0	16.08	0.855	0.54	7.46
1 : 1.1 : 0.1	15.65	0.860	0.59	8.07
1 : 1 : 0.2	18.11	0.863	0.56	8.76
1 : 0.7 : 0.3	17.24	0.892	0.58	9.04
1 : 0.9 : 0.3	17.21	0.866	0.56	8.43
1 : 0.6 : 0.6	17.57	0.865	0.55	8.42
1 : 0 : 1.2	13.50	0.817	0.66	7.31

These results also indicate that MF is a crucial factor to determine V_{oc} on ternary OPVs. Moreover, the variation of V_{oc} is measured as nearly 0.08 V in ternary blend system. This result indicates that the improvement of V_{oc} is nearly 3~9 % by hot-state matching (MODO). And the scale of V_{oc} improvement also similar with our previous result. Consequently, we demonstrated that DOS matching is the novel and efficient ratio adjustment of ternary blend system. We also investigate the tendency of V_{oc} with other parameters (see **Figure 39**), however the only V_{oc} shows the tendency with MF.

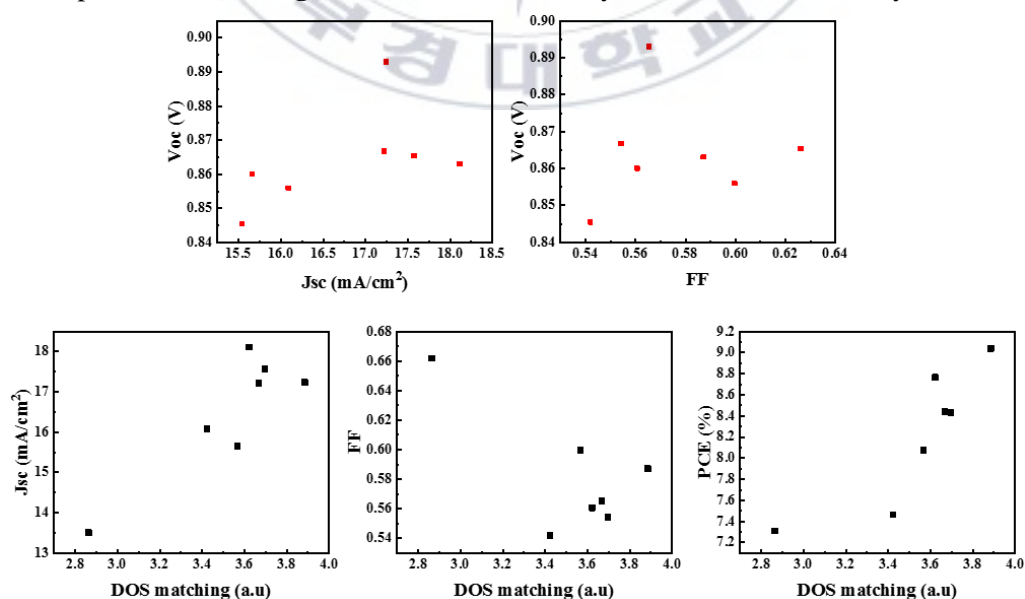


Figure 39. Diverse tendency between photovoltaic parameter and DOS matching

Based on our results, we illustrate the mechanism of PICT as shown in **Figure 40**. First, the electrons on donor are excited to particular energy levels which rely on the energy of irradiated photon. In the equilibrium states, if the hot-state matching are low (mismatched state), the electrons should be relaxed toward the thermally stable state. Then, because of the relaxation, electrons are bound at the CT states. Since the probability of non-radiative recombination is increased at CT states, the number of mobile carriers are reduced. Therefore, this mismatched states process results in the low V_{oc} by deeper quasi-Fermi level. Otherwise, at the well-matched states, the electrons transfer to acceptor domains occurs as the process of directly generated mobile carriers. Therefore, the number of much more mobile carriers enhanced V_{oc} by quasi-Fermi level shift toward LUMO level of acceptor. Our results are consistent with the importance of full range MODO and charge transfer. These results demonstrate that MF is crucial factor to determine the PICT. Therefore, we suggest that applying MF for configuration of organic materials can be a new and advanced strategy for efficient charge transfer and improvement of V_{oc} .

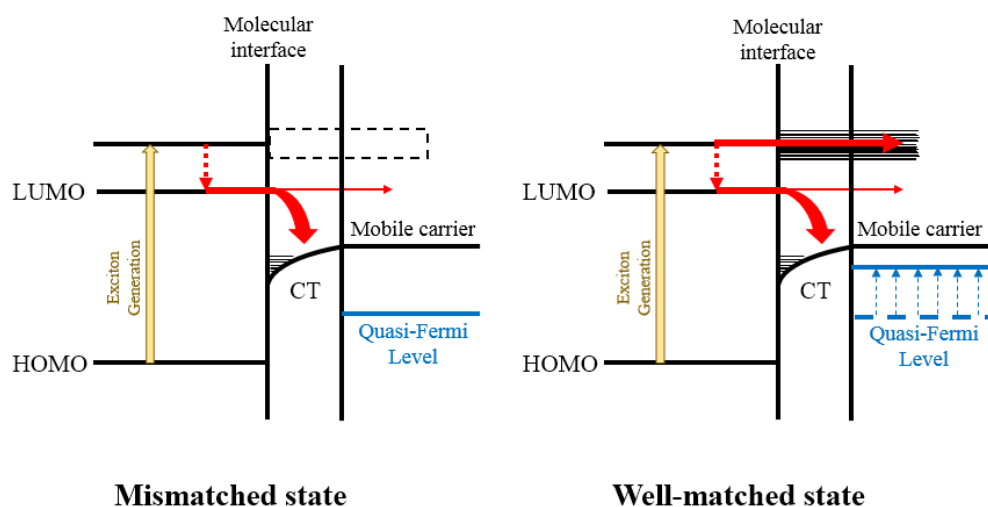


Figure 40. Charge transfer mechanism on mismatched and well-matched states

5.2.2 Design of Conjugated Organic materials

The performances of solar cell devices have improved in recent years with the syntheses of novel materials that feature a donor-acceptor (D-A) structure. In this context, the phenazine moiety is an attractive electron-withdrawing moiety due to its coplanar structure by resulting from the fusing of multiple aromatic rings. As a result, phenazine can take part in π - π interactions and exhibit close packing properties. It has also been found that polymers containing phenazine units show expanded absorption areas in their UV-vis spectra, which give enhanced short circuit current densities (J_{sc}) values. Indeed, polymers containing phenazine as the acceptor unit have been reported to exhibit low band gap and lead to efficient OSCs. In addition, the introduction of fluorine atoms into the conjugated backbone leads to a relatively deep highest occupied molecular orbital (HOMO) energy level, thereby increasing the open circuit voltages (V_{oc}) of OSCs. Thiophene moieties have also been incorporated into polymer building blocks of various conjugation lengths, wherein increased numbers of thiophene result in a decreased electrochemical bandgap between the HOMO and LUMO energy levels.

The strategy for design of conjugated organic materials in this research is the synthesis of push-pull conjugated polymers containing mono-fluorinated phenazine as the electron deficient unit and benzo[1,2-b:4,5-b']dithiophene as the electron donor. The introduction of thiophene units into the conjugated packing is expected to lower the HOMO energy levels of the synthesized polymers due to the increased conjugation length. To control the HOMO energy level and bandgap, conjugated polymers containing mono-fluorophenazine, thiophene, and benzodithiophene synthesized (i.e., of the PBDT-FPz, PBDT-TFPz, and PBDT-DTFPz). These push-pull type polymers

are synthesized via a Stille coupling reaction of 6-bis(trimethyltin) 4,8-bis (2-ethylhexyloxy)benzo[1,2-b:4,5-b']dithiophene as the electron donor, 2-fluorophenazine as the electron acceptor, and thiophene unit of various lengths as the bridge. The optical, electrochemical, and photovoltaic properties of the synthesized polymers are also investigated.

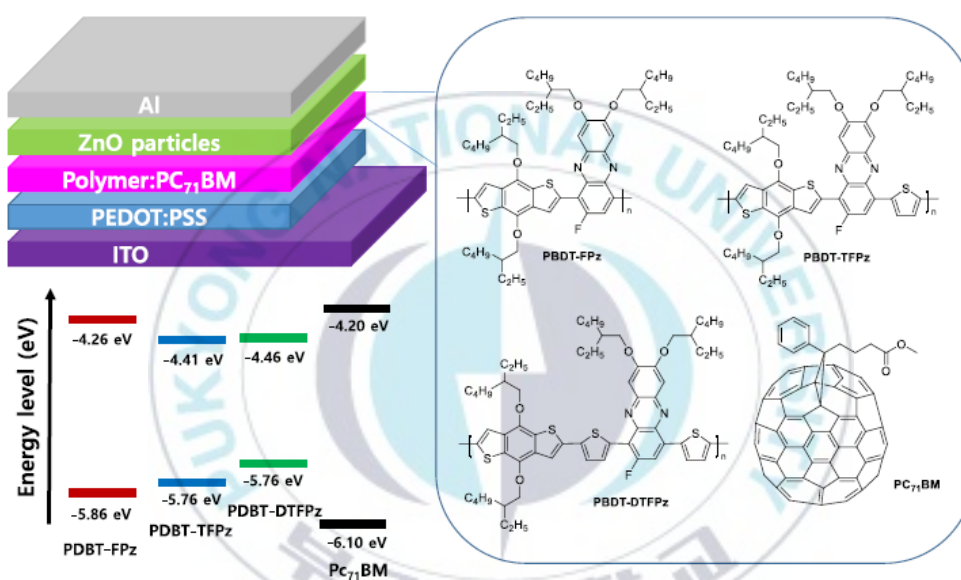


Figure 41. Molecular structures and energy levels of electron donor and PC₇₁BM and schematic diagram of the PSC device architecture.

<Optical properties of the synthesized organic material>

The absorption spectra of thin film are shown in **Figure 42 (a)**. The solutions for analysis were prepared using DCB as the solvent, while the thin films were obtained by pin-coating on a quartz plate from the DCB solution at room temperature. In the solution form, PDBT-FPz, PDBT-TFPz, and PDBT-DTFPz, exhibited similar absorption spectra, with absorption maxima at 580, 578 and 591 nm, respectively, while in the thin films, the maximum the number of thiophene in repeating unit increases, the

configuration length increases. PBDT-TFPz, with only one thiophene introduced, was blue-shifted with an increase in asymmetry. The absorption edges of the PBDT-FPz, PBDT-TFPz, and PBDT-DTFPz films were detected at 738, 747, and 756 nm, corresponding to optical bandgaps of 1.68, 1.66 and 1.64 eV, respectively. These results indicated a red shift in the absorption maxima in the thin film form. In addition, the broader peaks observed in the spectra of the thin film samples indicate the presence of stronger aggregation or more ordered π - π stacking in the solid form.

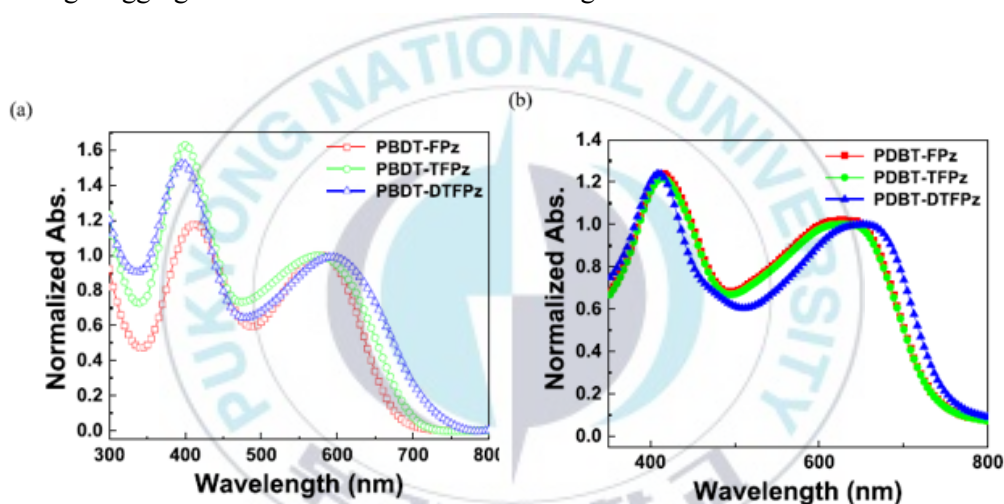


Figure 42. UV-visible absorption spectra of polymers in dichlorobenzene solution (a) and the solid state (b).

<Electrochemical and theoretical calculations>

The electrochemical properties of the polymers were determined from the band gap, which in turn was estimated from the absorption onset wavelength and the HOMO energy level obtained by cyclic voltammetry (CV) measurements in an acetonitrile solution of tetrabutylammonium tetrafluoroborate (Bu_4NBF_4 , 0.10 M) at a scan rate of 100 mV/s and at room temperature under argon. A platinum electrode ($\sim 0.05 \text{ cm}^2$) coated with a thin polymer film was used as the working electrode, and a Pt wire and a

Ag/AgNO₃ electrode were used as the counter and reference electrodes, respectively. The energy level of the Ag/AgNO₃ reference electrode (calibrated by the Fc/Fc⁺ redox system) was 4.8 eV below the vacuum level. **Figure 43** shows the CV spectra of the polymers, and the optoelectrical properties are summarized in **Table 3**. The HOMO and lowest unoccupied molecular orbital (LUMO) levels were calculated according to the empirical formulas ($E_{\text{HOMO}} = -([E_{\text{onset}}]^{\text{ox}} + 4.8) \text{ eV}$) and ($E_{\text{LUMO}} = -([E_{\text{onset}}]^{\text{red}} + 4.8) \text{ eV}$), respectively. The oxidation potential onsets of PBDT-FPz, PBDT-TFPz, and PBDT-DTFPz were determined to be 0.80, 0.96 and 1.06 V, respectively, which correspond to HOMO energy levels of - 5.86, - 5.76 and - 5.60 eV, respectively. The PBDT-FPz, PBDT-TFPz, and PBDT-DTFPz have lower HOMO energy levels due to mono-fluoro atom in phenazine moiety.

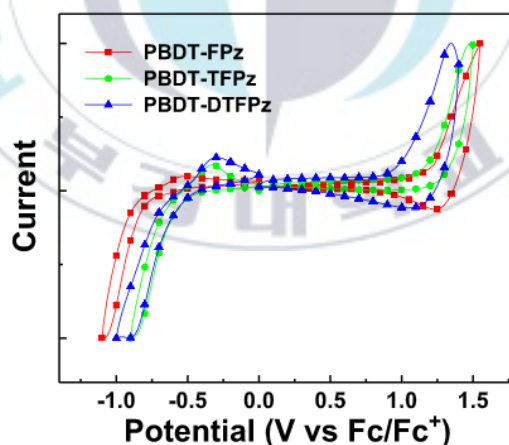


Figure 43. Electrochemical properties of polymers

Table 3. Optoelectrical properties of Polymers

polymers	optical band gap ^a (eV)	HOMO ^b (eV)	LUMO ^c (eV)	E_{ox}^{d} (V)	$E_{\text{red}}^{\text{d}}$ (V)	electrochemical band gap ^e (eV)
PBDT-FPz	1.68	-5.86	-4.26	1.06	-0.54	1.60
PBDT-TFPz	1.66	-5.76	-4.41	0.96	-0.39	1.35
PBDT-DTFPz	1.64	-5.60	-4.46	0.80	-0.34	1.14

^a Optical energy band gap was estimated from the onset wavelength of the optical absorption.

^b Calculated from the oxidation potentials.

^c Calculated from the reduction potentials.

^d Onset oxidation and reduction potential measured by cyclic voltammetry.

^e Calculated from the E_{ox} and E_{red} .

These results therefore indicate that upon increasing the number of thiophene units, the HOMO energy level increases. In addition, the LUMO energy levels of PBDT-FPz, PBDT-TFPz, and PBDT-DTFPz were determined to be - 4.46, - 4.41, and - 4.26 eV, respectively, and so the electrochemical band gap, calculated from the CV data, were 1.60, 1.35, and 1.14 eV, respectively. It was therefore apparent that the polymers based on phenazine units as the acceptor unit exhibited a low band gap. Moreover, in the case of the polymers containing greater numbers of thiophene units, the HOMO energy levels were elevated and the LUMO energy levels were lowered, thereby reducing the electrochemical bandgaps.

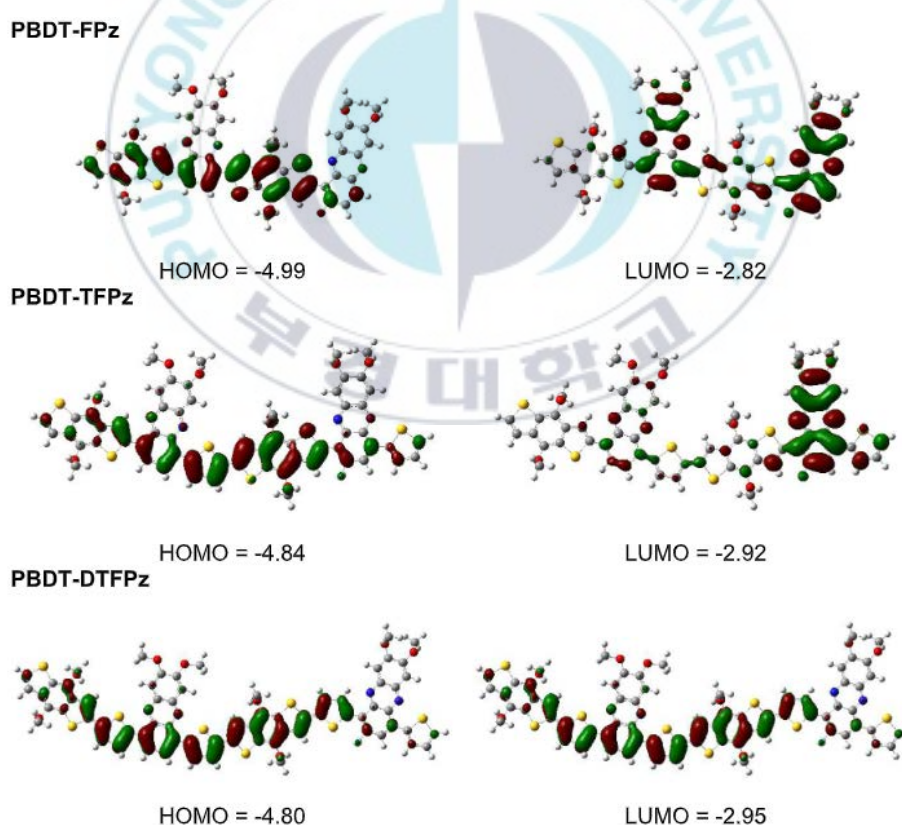


Figure 44. Theoretical calculation of the monomers by density functional theory (DFT) at the B3LYP/6-31 G level.

The optimized geometry for each polymer was then calculated using the B3LYP/6-31 G level of theory in the Gaussian 03 package to gain insight regarding their electronic structures. The HOMO and LUMO surfaces were plotted using GaussView version 4.1. To simplify the computations, the alkyl chains were replaced with methyl groups, and only two repeating units were used for the polymer backbone. We studied the tunability of the HOMO and LUMO energy levels of synthesized compounds using a computational methods. The optimized structures of PBDT-FPz, PBDT-TFPz, and PBDT-DTFPz are shown in **Figure 44**, and the HOMO/LUMO levels were determined computationally to be - 4.99/- 2.82, - 4.84/- 2.92 and - 4.80/- 2.95 eV for PBDT-FPz, PBDT-TFPz, and PBDT-DTFPz, respectively. These results therefore confirm that the HOMO energy levels increased upon the incorporation of greater numbers of thiophene units.

<Photovoltaic properties>

The hole and electron mobilities of the polymer:PC71BM blend films were measured using the space charge limited current (SCLC) method with the device structure ITO/PEDOT:PSS /polymer: PC71BM/Au for holes and ITO/ZnO/ polymer:PC71BM/ ZnO nanoparticules/ Al for electrons. The thin films were fabricated under the same condition as OPV devices. *J-V* characteristics showed a quadratic dependence on voltage over a range of several volts, which was consistent with the Mott–Gurney equation as below.

$$J_{SCL} = 9\varepsilon_0\varepsilon_r\mu V^2/8L^3 \text{-----Equation 8.}$$

Where ϵ_0 is the free-space permittivity, ϵ_r is the dielectric constant of the polymer:PC71BM blend films, μ is the mobility, V is the applied voltage and L is the thickness of the photoactive films. The hole mobilities of the PBDT-FPz, PBDT-TFPz, and PBDT-DTFPz devices were $3.30 \times 10^{-5} \text{ cm}^2/\text{Vs}$, $2.61 \times 10^{-4} \text{ cm}^2/\text{Vs}$ and $4.85 \times 10^{-4} \text{ cm}^2/\text{Vs}$, respectively. The electron mobilities were calculated to be $1.1 \times 10^{-6} \text{ cm}^2/\text{Vs}$ for PBDTFPz, $4.8 \times 10^{-3} \text{ cm}^2/\text{Vs}$ for PBDT-TFPz and $3.34 \times 10^{-3} \text{ cm}^2/\text{Vs}$ for PBDT-DTFPz. The hole mobility of PBDT-DTFPz shows an increase, which could lead to a relatively higher FF value in PSCs resulted from the more planar polymer backbone and increased intermolecular interactions. To demonstrate the potential application of the synthesized polymers in PSCs, we employed our polymers as the electron donor and PC71BM as the electron acceptor to fabricate BHJ PSCs with a configuration of ITO/ PEDOT:PSS/polymer:PC71BM/Al under AM 1.5 G irradiation ($100 \text{ mW}/\text{cm}^2$). **Figure 45** shows the current density-voltage plots of the prepared OSCs, while **Table 4** lists the open circuit voltages (V_{oc}), short circuit current densities (J_{sc}), fill factors (FF), and PCEs of the devices. The active layers were prepared by spin-coating the blend solutions of PBDTFPz,

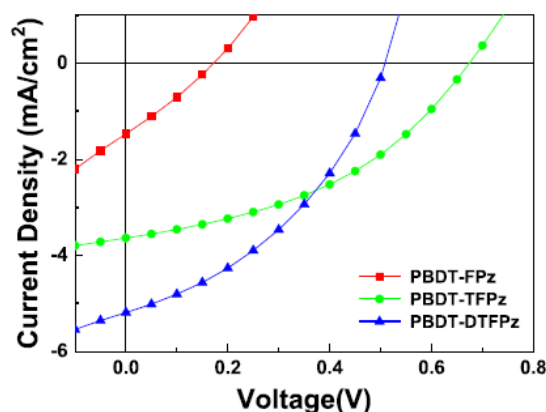


Figure 45. Current density-voltage characteristics of the polymer solar cells under the illumination of AM 1.5, $100 \text{ mW}/\text{cm}^2$.

Table 4. Photovoltaic Properties of the Polymer solar cell

	J_{sc} (mA/cm ²)	V_{oc} (V)	FF	PCE (%)
PBDT-FPz	1.47	0.17	0.28	0.07
PBDT-TFPz	3.64	0.67	0.41	1.00
PBDT-DTFPz	5.12	0.59	0.55	1.66

PBDT-TFPz, and PBDT-DTFPz as electron donor materials and PC71BM as the electron acceptor materials in DCB. The devices based on PBDT-TFPz:PC71BM and PBDT-DTFPz:PC71BM showed V_{oc} values of 0.67 and 0.59 V, J_{sc} values of 3.64 and 5.12 mA/cm², and FF values of 0.41 and 0.55, and PCEs of 1.00% and 1.66%, respectively. These results suggest that the high molecular weight of PBDT-DTFPz improves the device efficiency due to its superior morphology. The incident-photon-to-current efficiency (IPCE) spectra of the photovoltaic devices constructed using the polymer:PCBM blends are presented in **Figure 46**. The spectra have maxima of 21.9% at 410 nm, 27.1% at 450 nm and 35.3% at 450 nm, for PBDT-FPz, PBDT-TFPz, and PBDT-DTFPz, respectively.

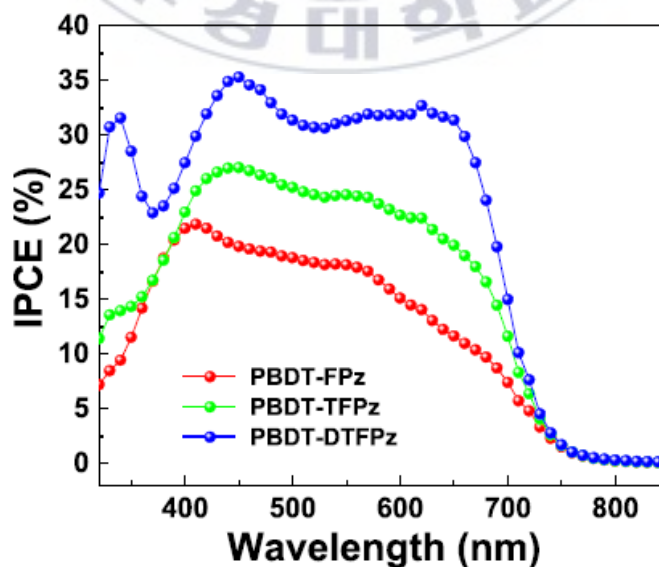
**Figure 46. IPCE curves of the corresponding polymer solar cells**

Figure 47 shows atomic force microscopy (AFM) images depicting the surface morphologies (surface area of $5 \times 5 \mu\text{m}^2$) of the polymer blend thin films with DIO. The blended films of PBDTTFPz: PC71BM has increased roughness due to increased asymmetry from introduction of one thiophene in repeating units.

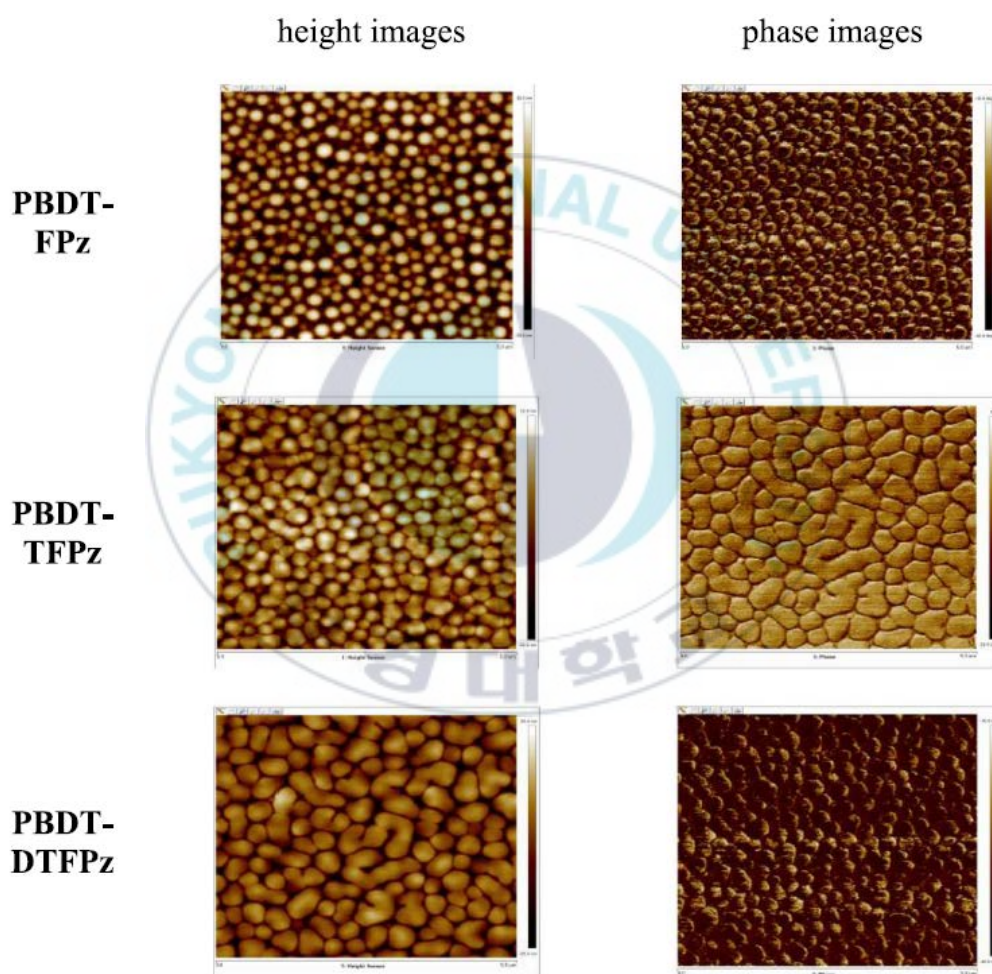


Figure 48. AFM images of films spin coated from PBDT-FPz:PC70BM, PBDT-TFPz:PC70BM and PBDT-DTFPz:PC70BM with DIO.

5.3 Conclusion

Using the MF value, we investigated the correlation between the V_{oc} loss of OPVs and the energy-state matching at the BHJ interface. In binary systems, OPVs with smaller MFs have higher V_{oc} values, and this tendency was confirmed for a ternary OPV device with three active materials. Based on the results, we conclude that energy-state matching between the donor and acceptor is one of the critical factors for suppressing energy loss and maximizing V_{oc} . Finally, we achieved a high-efficiency ternary OPV device with a PCE of 16.15% by controlling the MF value. We believe that the MF developed in this study enables estimations of the V_{oc} loss in OPVs and the design of optimized mixtures of donors and acceptors for high-performance OPV devices with the maximum V_{oc} .

Moreover, the HOMO energy levels difference of PBDT-FPz, PBDTTFPz and PBDT-DTFPz which were determined to be - 5.86, - 5.76, and - 5.60 eV, respectively, was determined for enhancement of V_{oc} . Thereby indicating that increased numbers of thiophene units in the backbone resulted in high HOMO energy levels. In addition, the electrochemical band gaps for PBDT-FPz, PBDT-TFPz, and PBDT-DTFPz were determined to be 1.60, 1.35 and 1.14 eV, respectively, indicating that these polymers based on phenazine as the acceptor unit exhibited low band gaps. Finally, the potential applicability of these polymers in perovskite solar cells was examined, and the device based on PBDT-DTFPz:PC71BM with DIO (3 vol%) exhibited the best photovoltaic performance, showing a V_{oc} of 0.59 V, a JSC of 5.12 mA/cm², a FF of 55%, and a PCE of 1.69%.

CHAPTER 6 CONCLUSION

We developed an effective method to quantify the degree of hot-state matching between the donor and acceptor in the blend system. By calculating the MF of BHJ thin film from the MODO between the donor and acceptor, we quantify the degree of energy-state mismatching between the electron donor and acceptor at their interface. A smaller MF value indicates a higher degree of energy-level matching, whereas a larger MF value indicates a lower degree of state overlapping at the BHJ interface. In order to demonstrate the effect of hot-state matching via calculation of MF, we measured TAS for targeting electrons which excited on corresponded hot-state energy levels. From the TAS result, we can observe the relation between MF and the generation rate of CT states in the blend system. The energy level with low MF which is well-matched energy level has the relatively low generation rate of CT states, while the energy level with the higher MF has huge CT states. The result means that the hot-state matching between donor and acceptor is strongly related with the PICT in the organic blend system.

Using the MF value, we investigated the correlation between the V_{oc} loss of OPVs and the energy-state matching at the BHJ interface. In binary systems, OPVs with smaller MFs have higher V_{oc} values, and this tendency was confirmed for a ternary OPV device with three active materials. Based on the results, we conclude that energy-state matching between the donor and acceptor is one of the critical factors for suppressing energy loss and maximizing V_{oc} . Finally, we achieved a high-efficiency ternary OPV device with a PCE of 16.15% by controlling the MF value. We believe

that the MF developed in this study enables estimations of the V_{oc} loss in OPVs and the design of optimized mixtures of donors and acceptors for high-performance OPV devices with the maximum V_{oc} .

Moreover, the HOMO energy levels difference of PBDT-FPz, PBDTTFPz and PBDT-DTFPz which were determined to be - 5.86, - 5.76, and - 5.60 eV, respectively, was determined for enhancement of V_{oc} . Thereby indicating that increased numbers of thiophene units in the backbone resulted in high HOMO energy levels. In addition, the electrochemical band gaps for PBDT-FPz, PBDT-TFPz, and PBDT-DTFPz were determined to be 1.60, 1.35 and 1.14 eV, respectively, indicating that these polymers based on phenazine as the acceptor unit exhibited low band gaps. Finally, the potential applicability of these polymers in perovskite solar cells was examined, and the device based on PBDT-DTFPz:PC71BM with DIO (3 vol%) exhibited the best photovoltaic performance, showing a V_{oc} of 0.59 V, a JSC of 5.12 mA/cm², a FF of 55%, and a PCE of 1.69%.

REFERENCES

- 1 J. Hou, O. Inganäs, R. H. Friend and F. Gao, *Nat. Mater.*, 2018, **17**, 119–128.
- 2 G. Dennler, M. C. Scharber and C. J. Brabec, *Adv. Mater.*, 2009, **21**, 1323–1338.
- 3 A. J. Heeger, *Adv. Mater.*, 2014, **26**, 10–28.
- 4 A. J. Heeger, *Semiconducting and metallic polymers*, 2001, **36**, 1–45.
- 5 A. J. Heeger, *Semiconducting and metallic polymers*, 2001, **36**, 1–42.
- 6 A. J. Heeger, *Semiconducting and metallic polymers*, 2001, **36**, 1–5.
- 7 A. J. Heeger, *Semiconducting and metallic polymers*, 2001, **36**, 1–19.
- 8 A. J. Heeger, *Curr. Appl. Phys.*, 2001, **1**, 247–267.
- 9 T. Kumari, S. M. Lee, S. H. Kang, S. Chen and C. Yang, *Energy Environ. Sci.*, 2017, **10**, 258–265.
- 10 H. Y. Chung, J. H. Park, J. Cui, S. Y. Kim, J. Oh, D. Kim and S. Y. Park, *J. Phys. Chem. C*, 2021, **125**, 18352–18361.
- 11 L. Zhang, Z. Zhang, D. Deng, H. Zhou, J. Zhang and Z. Wei, *Adv. Sci.*, 2022, **2202513**, 2202513.
- 12 M. K. Cyrański, *Chem. Rev.*, 2005, **105**, 3773–3811.
- 13 Y. Bai, M. Hao, S. Ding, P. Chen and L. Wang, *Adv. Mater.*, 2022, **34**, 1–35.
- 14 A. J. Gillett, A. Privitera, R. Dilmurat, A. Karki, D. Qian, A. Pershin, G. Londi, W. K. Myers, J. Lee, J. Yuan, S. J. Ko, M. K. Riede, F. Gao, G. C. Bazan, A. Rao, T. Q. Nguyen, D. Beljonne and R. H. Friend, *Nature*, 2021, **597**, 666–671.
- 15 J. P. Correa-Baena, A. Abate, M. Saliba, W. Tress, T. Jesper Jacobsson, M. Grätzel and A. Hagfeldt, *Energy Environ. Sci.*, 2017, **10**, 710–727.
- 16 B. S. Braun, W. R. Salaneck and M. Fahlman, 2009, 1450–1472.
- 17 H. Tamura and I. Burghardt, , DOI:10.1021/ja4093874.
- 18 Z. S. Wang, W. E. I. Sha and W. C. H. Choy, *J. Appl. Phys.*, , DOI:10.1063/1.4970958.
- 19 Z. Zheng, N. R. Tummala, Y. T. Fu, V. Coropceanu and J. L. Brédas, *ACS Appl. Mater. Interfaces*, 2017, **9**, 18095–18102.
- 20 H. Tamura and I. Burghardt, *J. Am. Chem. Soc.*, 2013, **135**, 16364–16367.
- 21 X. Y. Zhu, Q. Yang and M. Muntwiler, *Acc. Chem. Res.*, 2009, **42**, 1779–1787.

- 22 C. Phys. , DOI:10.1063/5.0099986.
- 23 Y. Hassan, J. H. Park, M. L. Crawford, A. Sadhanala, J. Lee, J. C. Sadighian, E. Mosconi, R. Shivanna, E. Radicchi, M. Jeong, C. Yang, H. Choi, S. H. Park, M. H. Song, F. De Angelis, C. Y. Wong, R. H. Friend, B. R. Lee and H. J. Snaith, *Nature*, 2021, **591**, 72–77.
- 24 A. C. Jakowetz, M. L. Böhm, J. Zhang, A. Sadhanala, S. Huettner, A. A. Bakulin, A. Rao and R. H. Friend, *J. Am. Chem. Soc.*, 2016, **138**, 11672–11679.
- 25 N. S. SARICIFTCI and A. J. HEBGER, *Int. J. Mod. Phys. B*, 1994, **08**, 237–274.
- 26 N. S. Sariciftci, L. Smilowitz, A. J. Heeger and F. Wudi, 1992, **258**, 27–30.
- 27 N. S. Sariciftci, L. Smilowitz, A. J. Heeger and F. Wudl, *Science (80-.)*, 1992, **258**, 1474–1476.
- 28 L. G. Kaake, J. J. Jasieniak, R. C. Bakus, G. C. Welch, D. Moses, G. C. Bazan and A. J. Heeger, , DOI:10.1021/ja308949m.
- 29 I. W. Hwang, D. Moses and A. J. Heeger, *J. Phys. Chem. C*, 2008, **112**, 4350–4354.
- 30 N. S. Sariciftci, L. Smilowitz, A. J. Heeger and F. Wudl, *Science (80-.)*, 1992, **258**, 1474–1476.
- 31 C. M. Oh, J. Lee, S. H. Park and I. W. Hwang, *J. Phys. Chem. Lett.*, 2021, **12**, 6418–6424.
- 32 D. Veldman, S. C. J. Meskers and R. A. J. Janssen, *Adv. Funct. Mater.*, 2009, **19**, 1939–1948.
- 33 M. Koppe, H. J. Egelhaaf, G. Dennler, M. C. Scharber, C. J. Brabec, P. Schilinsky and C. N. Hoth, *Adv. Funct. Mater.*, 2010, **20**, 338–346.
- 34 C. W. Schlenker, C. Li, H. Yip, A. K. Jen, A. Rao, P. C. Y. Chow, S. Ge, D. S. Ginger and R. H. Friend, 6–11.
- 35 S. Liu, J. Yuan, W. Deng, M. Luo, Y. Xie, Q. Liang, Y. Zou, Z. He, H. Wu and Y. Cao, *Nat. Photonics*, 2020, **14**, 300–305.
- 36 D. Baran, N. Gasparini, A. Wadsworth, C. H. Tan, N. Wehbe, X. Song, Z. Hamid, W. Zhang, M. Neophytou, T. Kirchartz, C. J. Brabec, J. R. Durrant and I. McCulloch, *Nat. Commun.*, 2018, **9**, 1–9.
- 37 C. Zhong, H. Choi, J. Y. Kim, H. Y. Woo, T. L. Nguyen, F. Huang, Y. Cao and A. J. Heeger, *Adv. Mater.*, 2015, **27**, 2036–2041.
- 38 I. W. Hwang, C. Soci, D. Moses, Z. Zhu, D. Waller, R. Gaudiana, C. J. Brabec and A. J. Heeger, *Adv. Mater.*, 2007, **19**, 2307–2312.
- 39 J. A. Phys, I. Hwang, S. Cho, J. Y. Kim, K. Lee, N. E. Coates, D. Moses and A. J. Heeger, , DOI:10.1063/1.2951957.

- 40 G. Chai, Y. Chang, J. Zhang, X. Xu, L. Yu, X. Zou, X. Li, Y. Chen, S. Luo, B. Liu, F. Bai, Z. Luo, H. Yu, J. Liang, T. Liu, K. S. Wong, H. Zhou, Q. Peng and H. Yan, *Energy Environ. Sci.*, 2021, **14**, 3469–3479.
- 41 K. Miyata, *Nat. Mater.*, 2018, **17**, 377.
- 42 M. Maimaris, A. J. Pettipher, M. Azzouzi, D. J. Walke, X. Zheng, A. Gorodetsky, Y. Dong, P. S. Tuladhar, H. Crespo, J. Nelson, J. W. G. Tisch and A. A. Bakulin, *Nat. Commun.*, 2022, **13**, 4949.
- 43 L. Lu, M. A. Kelly, W. You and L. Yu, *Nat. Photonics*, 2015, **9**, 491–500.
- 44 B. Guzelturk, T. Winkler, T. W. J. Van de Goor, M. D. Smith, S. A. Bourelle, S. Feldmann, M. Trigo, S. W. Teitelbaum, H. G. Steinrück, G. A. de la Pena, R. Alonso-Mori, D. Zhu, T. Sato, H. I. Karunadasa, M. F. Toney, F. Deschler and A. M. Lindenberg, *Nat. Mater.*, , DOI:10.1038/s41563-020-00865-5.
- 45 A. A. Raheem, S. Kamaraj, V. Sannasi and C. Praveen, *Org. Chem. Front.*, 2018, **5**, 777–787.
- 46 R. S. Gurney, D. G. Lidzey and T. Wang, *Reports Prog. Phys.*, , DOI:10.1088/1361-6633/ab0530.
- 47 V. Tamilavan, J. Lee, R. Agneeswari, D. Y. Lee, Y. K. Jung, S. Cho, J. H. Jeong, Y. Jin, M. H. Hyun and S. H. Park, *Polymer (Guildf.)*, 2017, **125**, 182–189.
- 48 A. Gadisa, M. Svensson, M. R. Andersson and O. Inganas, *Appl. Phys. Lett.*, 2004, **84**, 1609–1611.
- 49 C. P. Chen, S. H. Chan, T. C. Chao, C. Ting and B. T. Ko, *J. Am. Chem. Soc.*, 2008, **130**, 12828–12833.
- 50 B. Qi and J. Wang, *J. Mater. Chem.*, 2012, **22**, 24315–24325.
- 51 N. Schopp, V. V. Brus, J. Lee, G. C. Bazan and T. Q. Nguyen, *Adv. Energy Mater.*, 2021, **11**, 1–10.
- 52 K. Vandewal, S. Albrecht, E. T. Hoke, K. R. Graham, J. Widmer, J. D. Douglas, M. Schubert, W. R. Mateker, J. T. Bloking, G. F. Burkhard, A. Sellinger, J. M. J. Fréchet, A. Amassian, M. K. Riede, M. D. McGehee, D. Neher and A. Salleo, *Nat. Mater.*, 2014, **13**, 63–68.
- 53 J. Chen, D. Jia, E. M. J. Johansson, A. Hagfeldt and X. Zhang, *Energy Environ. Sci.*, 2021, **14**, 224–261.
- 54 Y. Li, *Acc. Chem. Res.*, 2012, **45**, 723–733.
- 55 S. M. Menke, N. A. Ran, G. C. Bazan and R. H. Friend, *Joule*, 2018, **2**, 25–35.
- 56 J. Yao, T. Kirchartz, M. S. Vezie, M. A. Faist, W. Gong, Z. He, H. Wu, J. Troughton, T. Watson, D. Bryant and J. Nelson, 2015, **014020**, 1–10.

- 57 S. M. Ryno, Y. T. Fu, C. Risko and J. L. Brédas, *ACS Appl. Mater. Interfaces*, 2016, **8**, 15524–15534.
- 58 S. M. Falke, C. A. Rozzi, D. Brida, M. Maiuri, M. Amato, E. Sommer, A. De Sio, A. Rubio, G. Cerullo, E. Molinari and C. Lienau, *Science (80-.)*, 2014, **344**, 1001–1005.
- 59 M. Zhang, L. Zhu, G. Zhou, T. Hao, C. Qiu, Z. Zhao, Q. Hu, B. W. Larson, H. Zhu, Z. Ma, Z. Tang, W. Feng, Y. Zhang, T. P. Russell and F. Liu, *Nat. Commun.*, 2021, **12**, 1–10.
- 60 Q. An, F. Zhang, J. Zhang, W. Tang, Z. Deng and B. Hu, *Energy Environ. Sci.*, 2016, **9**, 281–322.
- 61 S. Karuthedath, J. Gorenflot, Y. Firdaus, N. Chaturvedi, C. S. P. De Castro, G. T. Harrison, J. I. Khan, A. Markina, A. H. Balawi, T. A. Dela Peña, W. Liu, R. Z. Liang, A. Sharma, S. H. K. Paleti, W. Zhang, Y. Lin, E. Alarousu, D. H. Anjum, P. M. Beaujuge, S. De Wolf, I. McCulloch, T. D. Anthopoulos, D. Baran, D. Andrienko and F. Laquai, *Nat. Mater.*, 2021, **20**, 378–384.
- 62 W. Xu, 2018, 206–221.
- 63 K. Vandewal, A. Gadisa, W. D. Oosterbaan, S. Bertho, F. Banishoeib, I. Van Severen, L. Lutsen, T. J. Cleij, D. Vanderzande and J. V. Manca, *Adv. Funct. Mater.*, 2008, **18**, 2064–2070.
- 64 M. A. Pan, T. K. Lau, Y. Tang, Y. C. Wu, T. Liu, K. Li, M. C. Chen, X. Lu, W. Ma and C. Zhan, *J. Mater. Chem. A*, 2019, **7**, 20713–20722.
- 65 T. Wang, T. R. Kafle, B. Kattel and W. L. Chan, *J. Am. Chem. Soc.*, 2017, **139**, 4098–4106.
- 66 W. Köntges, P. Perkhun, J. Kammerer, R. Alkarsifi, U. Würfel, O. Margeat, C. Vidolot-Ackermann, J.-J. Simon, R. R. Schröder, J. Ackermann and M. Pfannmöller, *Energy Environ. Sci.*, , DOI:10.1039/c9ee03535d.
- 67 Y. Liang, Z. Xu, J. Xia, S. T. Tsai, Y. Wu, G. Li, C. Ray and L. Yu, *Adv. Mater.*, 2010, **22**, 135–138.
- 68 X. Ma, J. Wang, J. Gao, Z. Hu, C. Xu, X. Zhang and F. Zhang, *Adv. Energy Mater.*, 2020, **10**, 1–9.
- 69 H. Min, D. Y. Lee, J. Kim, G. Kim, K. S. Lee, J. Kim, M. J. Paik, Y. K. Kim, K. S. Kim, M. G. Kim, T. J. Shin and S. Il Seok, *Nature*, 2021, **598**, 444–450.
- 70 J. C. Blakesley and D. Neher, *Phys. Rev. B - Condens. Matter Mater. Phys.*, , DOI:10.1103/PhysRevB.84.075210.
- 71 1–41.
- 72 A. A. Raheem, 2018, 777–787.
- 73 J. Vicente, J. S. Goulart, M. C. A. Premazzi, A. G. P. Sobrinho, A. A. Silva, M. C. S. Azeredo, J. B. Domingos and F. S. Miranda, *J. Mol. Struct.*, 2014, **1063**, 320–327.

- 74 Y. Yang, E. R. Davidson and W. Yang, *Proc. Natl. Acad. Sci. U. S. A.*, 2016, **113**, E5098–E5107.
- 75 A. Mahapatra, D. Prochowicz, M. M. Tavakoli, S. Trivedi, P. Kumar and P. Yadav, *J. Mater. Chem. A*, 2020, **8**, 27–54.
- 76 J. Bertrandie, J. Han, C. S. P. De Castro, E. Yengel, J. Gorenflot, T. Anthopoulos, F. Laquai, A. Sharma and D. Baran, *Adv. Mater.*, , DOI:10.1002/adma.202202575.
- 77 C. Bay, A. C. Vissing, D. Thaysen-Petersen, C. M. Lerche, K. Togsverd-Bo, J. Heydenreich and M. Haedersdal, *Lasers Surg. Med.*, 2017, **49**, 810–818.
- 78 J. Bhat, J. Birch, C. Whitehurst and S. W. Lanigan, *Lasers Med. Sci.*, 2005, **20**, 6–10.
- 79 C. H. Tan, A. Wadsworth, N. Gasparini, S. Wheeler, S. Holliday, R. S. Ashraf, S. D. Dimitrov, D. Baran, I. McCulloch and J. R. Durrant, *J. Phys. Chem. C*, 2019, **123**, 5826–5832.
- 80 K. Vandewal, S. Albrecht, E. T. Hoke, K. R. Graham, J. Widmer, J. D. Douglas, M. Schubert, W. R. Mateker, J. T. Bloking, G. F. Burkhard, A. Sellinger, J. M. J. Fréchet, A. Amassian, M. K. Riede, M. D. McGehee, D. Neher and A. Salleo, *Nat. Mater.*, 2014, **13**, 63–68.
- 81 A. You, M. A. Y. Be and I. In, , DOI:10.1063/1.4913519.
- 82 A. E. Jailaubekov, A. P. Willard, J. R. Tritsch, W. L. Chan, N. Sai, R. Gearba, L. G. Kaake, K. J. Williams, K. Leung, P. J. Rossky and X. Y. Zhu, *Nat. Mater.*, 2013, **12**, 66–73.
- 83 Y. Hassan, O. J. Ashton, J. H. Park, G. Li, N. Sakai, B. Wenger, A. A. Haghghirad, N. K. Noel, M. H. Song, B. R. Lee, R. H. Friend and H. J. Snaith, *J. Am. Chem. Soc.*, 2019, **141**, 1269–1279.
- 84 J. Yuan, Y. Zhang, J. Yuan, Y. Zhang, L. Zhou, G. Zhang, H. Yip, T. Lau and X. Lu, *Joule*, 1–12.
- 85 Y. Jeon, H. R. Choi, M. Lim, S. Choi, H. Kim, J. H. Kwon, K. C. Park and K. C. Choi, *Adv. Mater. Technol.*, 2018, **3**, 1–10.
- 86 C. W. Tang, *Appl. Phys. Lett.*, 1986, **48**, 183–185.
- 87 P. Schilinsky, C. Waldauf, J. Hauch and C. J. Brabec, *J. Appl. Phys.*, 2004, **95**, 2816–2819.
- 88 C. J. Brabec, A. Cravino, D. Meissner, N. S. Sariciftci, M. T. Rispens, L. Sanchez, J. C. Hummelen and T. Fromherz, *Thin Solid Films*, 2002, **403–404**, 368–372.
- 89 B. A. Gregg and M. C. Hanna, *J. Appl. Phys.*, 2003, **93**, 3605–3614.
- 90 C. Urich, D. Wynands, S. Olthof, M. K. Riede, K. Leo, S. Sonntag, B. Maennig and M. Pfeiffer, 2008, 1–6.

- 91 Y. Zhang, Y. Ma, I. Shin, Y. K. Jung, B. R. Lee, S. Wu, J. H. Jeong, B. H. Lee, J. H. Kim, K. H. Kim and S. H. Park, *ACS Appl. Mater. Interfaces*, 2020, **12**, 7186–7197.
- 92 R. Jasiūnas, H. Zhang, A. Devižis, M. Franckevičius, F. Gao and V. Gulbinas, *Sol. RRL*, 2022, **6**, 1–8.
- 93 H. Yang, D. Kim, B. R. Lee, J. Y. Kim and W. Bright, .
- 94 N. A. Ran, S. Roland, J. A. Love, V. Savikhin, C. J. Takacs, Y. T. Fu, H. Li, V. Coropceanu, X. Liu, J. L. Brédas, G. C. Bazan, M. F. Toney, Di. Neher and T. Q. Nguyen, *Nat. Commun.*, 2017, **8**, 1–9.
- 95 B. Xiao, A. Tang, J. Zhang, A. Mahmood, Z. Wei and E. Zhou, *Adv. Energy Mater.*, 2017, **7**, 1–7.
- 96 Y. Zhang, Y. Ma, I. Shin, Y. K. Jung, B. R. Lee, S. Wu, J. H. Jeong, B. H. Lee, J. H. Kim, K. H. Kim and S. H. Park, *ACS Appl. Mater. Interfaces*, 2020, **12**, 7186–7197.
- 97 F. Liu, L. Zhou, W. Liu, Z. Zhou, Q. Yue, W. Zheng, R. Sun, W. Liu, S. Xu, H. Fan, L. Feng, Y. Yi, W. Zhang and X. Zhu, *Adv. Mater.*, 2021, **2100830**, 1–8.
- 98 M. Wei, Z. Wang, Z. Wen, X. Hao and W. Qin, *Appl. Phys. Lett.*, 2018, **113**, 1–5.
- 99 K. Vandewal, K. Tvingstedt, A. Gadisa, O. Inganäs and J. V. Manca, *Phys. Rev. B - Condens. Matter Mater. Phys.*, 2010, **81**, 1–8.
- 100 D. Kim, I. Shin, H. S. Yang, P. M. Hangoma, J. S. Bae, B. R. Lee, J. H. Kim, D. K. Moon and S. H. Park, *J. Power Sources*, , DOI:10.1016/j.jpowsour.2021.230212.
- 101 L. Zhan, S. Li, T. K. Lau, Y. Cui, X. Lu, M. Shi, C. Z. Li, H. Li, J. Hou and H. Chen, *Energy Environ. Sci.*, 2020, **13**, 635–645.
- 102 T. M. Burke, S. Sweetnam, K. Vandewal and M. D. McGehee, *Adv. Energy Mater.*, 2015, **5**, 1–12.
- 103 L. Zhan, S. Li, T. K. Lau, Y. Cui, X. Lu, M. Shi, C. Z. Li, H. Li, J. Hou and H. Chen, *Energy Environ. Sci.*, 2020, **13**, 635–645.
- 104 S. Izawa, N. Shintaku, M. Kikuchi and M. Hiramoto, *Appl. Phys. Lett.*, , DOI:10.1063/1.5114670.
- 105 Y. Yan, Y. Zhang, Y. Liu, Y. Shi, D. Qiu, D. Deng, J. Zhang, B. Wang, M. A. Adil, K. Amin, W. A. Memon, M. Wang, H. Zhou, X. Zhang and Z. Wei, *Adv. Energy Mater.*, 2022, **12**, 1–9.
- 106 S. Chen, S. W. Tsang, T. H. Lai, J. R. Reynolds and F. So, *Adv. Mater.*, 2014, **26**, 6125–6131.
- 107 S. Mahesh, J. M. Ball, R. D. J. Oliver, D. P. McMeekin, P. K. Nayak, M. B. Johnston and H. J. Snaith, *Energy Environ. Sci.*, 2020, **13**, 258–267.
- 108 J. Lee, V. Tamilavan, K. H. Rho, S. Keum, K. H. Park, D. Han, Y. K. Jung, C. Yang, Y. Jin, J. W. Jang, J. H. Jeong and S. H. Park, *Adv. Energy Mater.*, 2018, **8**, 1–9.

- 109 Z. Ni, H. Jiao, C. Fei, H. Gu, S. Xu, Z. Yu, G. Yang, Y. Deng, Q. Jiang, Y. Liu, Y. Yan and J. Huang, *Nat. Energy*, , DOI:10.1038/s41560-021-00949-9.
- 110 J. J. Yoo, G. Seo, M. R. Chua, T. G. Park, Y. Lu, F. Rotermund, Y. Kim, C. S. Moon, N. J. Jeon, V. Bulović, S. S. Shin and M. G. Bawendi, *Nature*, , DOI:10.1038/s41586-021-03285-w.
- 111 P. M. Hangoma, Y. Ma, I. Shin, Y. Liu, W. I. Park, Y. K. Jung, B. R. Lee, J. H. Jeong, S. H. Park and K. H. Kim, *Sol. RRL*, 2019, **3**, 1–10.
- 112 V. V. Brus, N. Schopp, S. J. Ko, J. Vollbrecht, J. Lee, A. Karki, G. C. Bazan and T. Q. Nguyen, *Adv. Energy Mater.*, 2021, **11**, 1–10.
- 113 S. Yamamoto, A. Orimo, H. Ohkita, H. Benten and S. Ito, *Adv. Energy Mater.*, 2012, **2**, 229–237.
- 114 S. R. Cowan, A. Roy and A. J. Heeger, *Phys. Rev. B - Condens. Matter Mater. Phys.*, 2010, **82**, 1–10.
- 115 S. Figure, , DOI:10.1038/nature12339.
- 116 S. Minimized, N. Energy, O. Morphology and P. S. Cells, .
- 117 Z. Li, X. Xu, W. Zhang, X. Meng, Z. Genene, W. Ma, W. Mammo, A. Yartsev, M. R. Andersson, R. A. J. Janssen and E. Wang, *Energy Environ. Sci.*, 2017, **10**, 2212–2221.
- 118 H. Shi, R. Xia, G. Zhang, H. L. Yip and Y. Cao, *Adv. Energy Mater.*, 2019, **9**, 1–8.
- 119 Y. Zhang, Q. Chen, H. S. Yang, D. Kim, I. Shin, B. R. Lee, J. H. Kim, D. K. Moon, K. H. Kim and S. H. Park, *ACS Appl. Mater. Interfaces*, 2021, **13**, 33172–33181.
- 120 J. Lv, H. Tang, J. Huang, C. Yan, K. Liu, Q. Yang, D. Hu, R. Singh, J. Lee, S. Lu, G. Li and Z. Kan, *Energy Environ. Sci.*, 2021, **14**, 3044–3052.
- 121 X. K. Chen, V. Coropceanu and J. L. Brédas, *Nat. Commun.*, , DOI:10.1038/s41467-018-07707-8.
- 122 Y. H. L. Lin, M. A. Fusella and B. P. Rand, *Adv. Energy Mater.*, 2018, **8**, 1–16.
- 123 F. MacHui, S. Rathgeber, N. Li, T. Ameri and C. J. Brabec, *J. Mater. Chem.*, 2012, **22**, 15570–15577.
- 124 E. Yoon, K. Y. Jang, J. Park and T. W. Lee, *Adv. Mater. Interfaces*, 2021, **8**, 1–21.
- 125 H. J. Snaith, L. Schmidt-Mende, M. Grätzel and M. Chiesa, *Phys. Rev. B - Condens. Matter Mater. Phys.*, 2006, **74**, 1–6.
- 126 N. Gasparini, X. Jiao, T. Heumueller, D. Baran, G. J. Matt, S. Fladischer, E. Spiecker, H. Ade, C. J. Brabec and T. Ameri, *Nat. Energy*, 2016, **1**, 1–9.
- 127 L. Lu, T. Xu, W. Chen, E. S. Landry and L. Yu, *Nat. Photonics*, 2014, **8**, 716–722.
- 128 A. Nikolis, S. Bernstein, B. Kinney, V. Park and P. Surgery, 2016, 115–125.

- 129 Z. Guo, Y. Wan, M. Yang, J. Snaider, K. Zhu and L. Huang, *Science* (80-.), 2017, **356**, 59–62.
- 130 M. A. Becker, R. Vaxenburg, G. Nedelcu, P. C. Sercel, A. Shabaev, M. J. Mehl, J. G. Michopoulos, S. G. Lambrakos, N. Bernstein, J. L. Lyons, T. Stöferle, R. F. Mahrt, M. V. Kovalenko, D. J. Norris, G. Rainò and A. L. Efros, *Nature*, 2018, **553**, 189–193.
- 131 J. A. Phys., , DOI:10.1063/1.3086447.
- 132 Z. Cao, F. Hu, C. Zhang, S. Zhu, M. Xiao and X. Wang, *Adv. Photonics*, 2020, **2**, 8–10.
- 133 E. P. Koumoulos, S. A. M. Tofail, C. Silien, D. De Felicis, R. Moscatelli, D. A. Dragatogiannis, E. Bemporad, M. Sebastiani and C. A. Charitidis, *Mater. Des.*, 2018, **137**, 446–462.
- 134 G. Grancini, M. Maiuri, D. Fazzi, A. Petrozza, D. Brida, G. Cerullo, G. Lanzani and K. T. Gmbh, , DOI:10.1038/NMAT3502.
- 135 S. Shoaee, M. Stolterfoht and D. Neher, *Adv. Energy Mater.*, 2018, **8**, 1–20.
- 136 M. Saliba, J. P. Correa-Baena, M. Grätzel, A. Hagfeldt and A. Abate, *Angew. Chemie - Int. Ed.*, 2018, **57**, 2554–2569.
- 137 M. Ghasemi, N. Balar, Z. Peng, H. Hu, Y. Qin, T. Kim, J. J. Rech, M. Bidwell, W. Mask, I. McCulloch, W. You, A. Amassian, C. Risko, B. T. O. Connor and H. Ade, , DOI:10.1038/s41563-020-00872-6.
- 138 C. Zhang, S. Liang, W. Liu, F. T. Eickemeyer, X. Cai, K. Zhou, J. Bian, H. Zhu, C. Zhu, N. Wang, Z. Wang, J. Zhang, Y. Wang, J. Hu, H. Ma, C. Xin, S. M. Zakeeruddin, M. Grätzel and Y. Shi, *Nat. Energy*, 2021, **6**, 1154–1163.
- 139 Z. He, C. Zhong, X. Huang, W. Y. Wong, H. Wu, L. Chen, S. Su and Y. Cao, *Adv. Mater.*, 2011, **23**, 4636–4643.
- 140 M. Segal, A. Baldo, J. Holmes, R. Forrest and G. Soos, *Phys. Rev. B - Condens. Matter Mater. Phys.*, 2003, **68**, 1–14.
- 141 L. Lu, T. Xu, W. Chen, E. S. Landry and L. Yu, *Nat. Photonics*, 2014, **8**, 716–722.
- 142 Y. He, H. Y. Chen, J. Hou and Y. Li, *J. Am. Chem. Soc.*, 2010, **132**, 1377–1382.
- 143 Q. Wan, X. Guo, Z. Wang, W. Li, B. Guo, W. Ma, M. Zhang and Y. Li, *Adv. Funct. Mater.*, 2016, **26**, 6635–6640.
- 144 S. Zhang, Y. Qin, J. Zhu and J. Hou, *Adv. Mater.*, 2018, **30**, 1–7.
- 145 V. Tamilavan, S. Kim, J. Y. Sung, D. Y. Lee, S. Cho, Y. Jin, J. Jeong, S. H. Park and M. H. Hyun, *New J. Chem.*, 2016, **40**, 10153–10160.

ACKNOWLEDGEMENT

이렇게 감사의 글을 쓰려니 2017 년 가을부터 시작된 박사과정 동안 겪어 왔던 많은 일들이 주마등처럼 스쳐 지나갑니다. 비록 새로운 시작에 대한 설렘보다는 박사과정 동안의 아쉬움이, 박사로서의 자부심보다는 자질에 대한 부족함이 많이 느껴지지만, 그럼에도 불구하고 이 논문을 쓸 수 있었던 이유는 셀 수 없이 많은 분들의 도움이 있었기 때문에 가능했으며, 이렇게 감사의 말씀을 드리고자 합니다.

무엇보다도 제 박사과정기간 동안 아낌없는 지도와 지원을 주신 지도교수 박성흠 교수님께 깊은 감사를 드리고 싶습니다. 연구는 물론이고 하나의 인격체로서 성장을 할 수 있게끔 도와주신 박성흠 교수님을 만난 것은 저에게 있어 아주 큰 행운이고 축복이라고 생각합니다. 앞으로도 박사로서 교수님의 가르침을 바탕으로 참된 연구자가 되도록 더욱 노력하겠습니다.

그리고 항상 저에게 연구자로서의 방향성과 박사과정기간 동안 큰 에너지를 주신 인제대학교 정윤경 교수님께 깊은 감사를 드리고 싶습니다. 박사과정 동안 마주친 많은 어려움 속에서 정윤경 교수님의 지지와 가르침은 저에게 큰 동기부여가 되었습니다.

저와 함께 긴 시간을 같이 보낸 ODPL 멤버들에게도 감사를 드리고 싶습니다. 특히 연구기간 동안 항상 붙어 다니며 많이 싸우고 많이 웃기도 했던 단비, 옆에서 우직하게 저를 피곤해하는 인수햄에게 감사 드립니다. 그리고 항상 덤병대는 저를 챙겨준 근녕이, 온갖 굵은일 힘든 내색 없이 척척 해내는 은혜, 하나뿐인 부사수 호준이, my real friend Pesi and Yuan, ODPL 실험실내에서 저에게 많은 도움을 준 Dr.Tamil, 성범이, 유미, Fuqiang, Anqi, Wu, Lying, Du 에게도 많이 고맙다고 전하고 싶습니다.

마지막으로 항상 저를 아끼고 사랑해주는 가족들께 감사 드립니다. 이와 같은 많은 분들의 도움속에서 올바르게 훌륭한 연구자가 되도록 스스로 채찍질하며 노력하겠습니다.